Imperial College London

Department of Earth Science and Engineering

Thermal history of recrystallized carbonate rocks using clumped isotopes

Qi Adlan

Submitted in part fulfilment of the requirements for the degree of

Doctor of Philosophy

July 2022

I'm a drop in the ocean and I am the ocean in a drop

my greatest burden is unfulfilled potential

Abstract

Developed in the last two decades, carbonate clumped isotope approach (Δ_{47}) is suitable for temperature reconstruction of the (re)crystallization (TΔ_{47}) of all carbonate phases (Ghosh et al., 2006; Eiler, 2007). Unlike traditional oxygen isotope ($\delta^{18}O$) thermometers, clumped isotopes do not depend on the $\delta^{18}O$ of the fluid from which the carbonate minerals developed (Eiler, 2007). This has significant implications for diagenesis and thermal history reconstruction of carbonate rocks in sedimentary basins.

In this study, geological samples were used as a natural laboratory which provides a testing ground to understand the behaviour of clumped isotope-exchange reactions through burial–exhumation complexity. The objectives are to investigate the robustness of clumped isotope thermometers to archive thermal history in recrystallized carbonates and to add more constraints on processes associated with the thermal history of a formation using several carbonate species (calcite and dolomite). First, a new approach was developed to safely cleans samples contaminated by organic matter and hydrocarbons. Using subsurface carbonate samples, the recrystallization and clumped isotope-thermal resetting of different limestone components work were then assessed. Finally, investigation of the kinetic differences between minerals in recrystallized limestone and dolostone at various stages of the burial process were conducted across a regional orogeny in Oman.

The results of this thesis indicate that different carbonate fabrics recrystallize at different water/rock ratios and with different susceptibility to thermal resetting with respect to clumped isotopes. Fine-grained matrix continues to recrystallize even at a low water/rock ratio during the deep stage of burial and records a wide range of temperatures, suggesting continuous and probably partial recrystallization. Here the evidence of cessation of dissolution and re-precipitation reactions during burial are stopped by oil emplacement was found, extending the application of clumped isotope analyses to petroleum migration studies. This thesis also confirms for the first time in a natural environment that calcite and early dolomite record a different clumped isotope history when subjected to the same thermal history. Finally, this thesis demonstrates that more geological phenomena can be discovered using calcite and early dolomite at the same sampling point, which offers additional constraints on the burial model.

Declarations of originality and copyright

I hereby confirm that the work in this thesis is my own and I give appropriate references and citations whenever I refer to, describe or quote from the work of others.

Qi Adlan

Acknowledgements

Contents

List of Tables

List of Figures

Chapter 5

CHAPTER 1
INTRODUCTION

1.1 General Introduction

Temperature is one of the most important controls of many geological processes, and it has been studied as the thermochronology branch of knowledge in geology. The researcher uses the most fundamental empirical, descriptive, and deductive approaches to obtain temperature history information using materials from outcrops, core samples and seepage (McCulloh and Naeser, 1989).Thermal history information of rocks can only be obtained using paleo-thermometric techniques that depend on the presence of organic material or specific minerals. The existing techniques, such as vitrinite reflectance (Waples, 1982; Barker, 1983; Burnham and Sweeney, 1989; Sweeney and Burnham, 1990), Tmax in rock-eval pyrolysis (Burnham et al., 1987; Tissot et al., 1987; Peters et al., 1994), thermal alteration index or spore coloration index (Staplin, 1969; Lerche and McKenna, 1991), conodont colour index (Epstein et al., 1977), transmittance color index (Robison et al., 2000), Acritarch fluorescence (Obermajer et al., 1997) and ultraviolet excitation (Thompson-Rizer et al., 1988) are dependent on the existence of organic substances, and are generally used to obtain paleo-temperature information on shale and coal materials. On the other hand, techniques using smectite-illite mineral transformation (Burst, 1969; Pytte and Reynolds, 1989), fission-track annealing in apatite and zircon (Gleadow et al., 1986; Tagami et al., 1998), belemnite (carbonate) oxygen isotope composition (Stevens and Clayton, 1971; Rosales et al., 2004), fluid inclusions (Roedder and Bodnar, 1980; McLimans, 1987) and carbonate clumped isotopes (Eiler and Schauble, 2004; Ghosh et al., 2006; Eiler, 2007; Ghosh et al., 2007; Eiler, 2011) were developed based on the characteristics of specific minerals and are generally used to obtain paleo-temperature information on sandstones, siltstones, mudstones and carbonate rocks.

The carbonate clumped isotope method is the most effective proxy for temperature reconstruction in carbonate formations today, and has been widely used to reconstruct burial history of sedimentary basins (Dennis and Schrag, 2010; Passey and Henkes, 2012; Lechler et al., 2013; Snell et al., 2013; Garzione et al., 2014; Fan et al., 2014; Stolper and Eiler, 2015; Winkelstern and Lohmann, 2016; Gallagher et al., 2017; Lloyd et al., 2017; John, 2018; Lawson et al., 2018; Mangenot et al., 2018; Lacroix and Niemi, 2019; Naylor et al., 2020; Ryb et al., 2021; Hemingway and Henkes, 2021). Using this technique, it is essential first to understand the evolution of the Δ_{47} signature and the traditional isotope ($\delta^{13}C$ and $\delta^{18}O$) in carbonate formations through burial and exhumation processes. The clumped isotope (Δ_{47}) and the standard isotope content ($\delta^{13}C$ and $\delta^{18}O$) of carbonates may change via recrystallization in a water-buffered system or a rock-buffered system (equivalent to open or closed

1

systems in other studies). Water-buffered systems are developed when the carbonate mineral receives a high influx of fluid. The clumped isotope compositions (Δ_{47}) of carbonate minerals in this type of system are reset to values reflecting the ambient temperature of the fluid during recrystallization (Bergmann et al., 2018b; Ryb and Eiler, 2018; Stolper et al., 2018; Lawson et al., 2018; Ingalls, 2019; Ryb et al., 2021). In comparison, the rock-buffered system occurs under low water-rock ratio conditions. The clumped isotope compositions (Δ_{47}) under such conditions can also be altered through direct dissolution-precipitation processes, but are likely to retain their initial bulk isotope compositions. Interestingly, clumped isotope (Δ_{47}) alteration can also occur via isotopic reordering with no precipitation-(re)crystallization process involved. This process is known as 'solid-state reordering', which refers to the diffusive migration of C or O within the solid mineral (Dennis and Schrag, 2010; Passey and Henkes, 2012; Stolper and Eiler, 2015; Brenner et al., 2018; Lloyd et al., 2018; Ryb et al., 2021), with more details given in Chapter 2 and Chapter 5 of this thesis.

The examples cited highlight the complexity of Δ_{47} data of ancient carbonate formations, and also that this complexity is difficult to replicate in laboratory experiments. Understanding all the processes listed above and their effects on the clumped isotope composition is desirable, though, as it would allow us to reconstruct, with less uncertainty, the details of the thermal and diagenetic histories of recrystallized carbonate formations through the burial and exhumation processes. In this thesis, geological samples are used as a natural laboratory to understand the behaviour of clumped isotope-exchange reactions through burial–exhumation complexity. This thesis tested the capacity of carbonate clumped isotope paleo-thermometry to archive thermal evolution and the recrystallization process in carbonate rocks through various stages of the burial process across a regional orogeny. At the same time, the differences in the kinetics of carbonate mineral isotope re-equilibration and the response of different limestone fabrics to thermal resetting with respect to clumped isotopes are also investigated. The overall work reported in this PhD thesis offers additional constraints on the burial history model and will bring the community closer to unravelling the complexity of isotopic alteration of carbonate formations through natural processes such as burial and exhumation.

1.2   Aims

The main aims of this thesis were to: (1) develop a laboratory protocol to successfully measure clumped isotopes in samples contaminated with hydrocarbons, as would be the case in subsurface petroleum reservoirs where the industrial application of thermal history reconstructions might be needed; (2) to test how effective the clumped isotope thermometer in reconstructing the thermal history of recrystallized carbonate formations in hydrocarbon reservoirs with a relatively simple burial history;

and (3) to add more constraints on the thermal history reconstruction of complex tectonic areas by combining information from coeval calcite and dolomite in the same location.

1.3   Detailed objectives and approach

The first objective in general was to safely remove hydrocarbons from contaminated samples. This was achieved by testing the impact of Oxygen Plasma Ashing (OPA) on the relative abundance of mass 47 isotopologues. This objective includes the following details:

- To systematically investigate potential fractionation effects on the initial Δ_{47} values of carbonates, including the $\delta^{18}O$ values, $\delta^{13}C$ values, $\Delta 48$ offsets and 49 parameters after low-temperature oxygen plasma ashing treatment.
- Undertake an experiment using three natural samples with a large range of initial Δ_{47} value and exposure to different plasma exposure times: 10, 20, and 30 minutes.
- To provide recommendations for effective oxygen plasma ashing treatment, especially the best treatment duration for challenging samples such as oil-stained carbonates, bituminous shales, or host rocks with very high organic carbon content.

The second objective was to investigate the clumped isotope records of recrystallized carbonate rocks derived from shallow burial settings. This includes the following details :

- Determine whether different limestone components (larger skeletal grains and enclosing matrix) have different susceptibility to thermal resetting with respect to clumped isotopes.
- Investigate whether the Δ_{47} temperature recorded in this recrystallized carbonate rock is at equilibrium with the formation temperature.
- Test the hypothesis that water displacement inhibits or stops diagenesis by comparing the Δ_{47} temperature of recrystallized limestone, the established burial history, and the timing of petroleum accumulation.

Finally, the last objective was to investigate the clumped isotope records of recrystallized limestone and dolostone across the Oman Mountain orogenic belt. The samples were selected from various stratigraphic intervals and in areas with different degrees of burial and exhumation. This last objective includes the following details:

- Investigate the environment of recrystallization and associated processes at different stages of burial, and their impact on the recorded isotopic composition (Δ_{47}, $\delta^{18}O$ and $\delta^{13}C$).

- Examine whether natural calcite and early dolomite record a different clumped isotope signal when subjected to the same thermal history, thus testing laboratory experiments suggesting a difference in kinetics for these two minerals.

- Examine whether dolomite is more resistant to Δ_{47} alteration during burial and exhumation, and at the same time, identify the difference in cooling temperature between minerals.

- Perform XRD analysis on the eogenetic dolomite to confirm a relationship between cation ordering and clumped isotope temperatures.

- Investigate the clumped isotope records and cation ordering in hydrothermal dolomite and its difference to early dolomite.

1.4   Thesis outline and publications

This thesis consists of 6 chapters, and is organised as follows:

Chapter 1: "Introduction". This chapter provides general introduction, research background, aims and objectives of thesis.

Chapter 2: "Theoretical background and methodology". This chapter presents a literature review on thermal history reconstruction of rocks, background to the clumped isotope measurement technique and carbonate recrystallization processes. The methodology in this chapter includes the carbon dioxide extraction, purification and data processing used in the Qatar Stable Isotope Laboratory at Imperial College London.

Chapter 3: "Petroleum contaminant in carbonate samples and how to safely clean it". Organic contaminant (i.e. hydrocarbon) is one of the main issue in clumped isotope measurement. This chapter provides an analytical approach to address the petroleum contaminant issue. Using the Oxygen Plasma Ashing technique, a protocol is developed to prepare and safely clean contaminated-subsurface samples for clumped isotope measurement.

This chapter was published in 2020 in Rapid Communications in Mass Spectrometry:

Adlan, Q., Davies, A. J., & John, C. M. (2020). *Effects of oxygen plasma ashing treatment on carbonate clumped isotopes. Rapid Communications in Mass Spectrometry, 34(14), e8802. https://doi.org/10.1002/rcm.8802*

Chapter 4: "Recrystallization temperature of shallowly buried carbonates and potential clumped isotope application for petroleum migration study". This chapter focuses on clumped isotope records of recrystallized calcite in shallow burial setting and the evidence that different carbonate fabrics

recrystallize and reset at different water/rock ratios through time. This includes the first report of the application of clumped isotope analyses application for petroleum migration studies.

This chapter was published in 2023 in Chemical Geology:

Adlan, Q. and John, C.M. (2023). *Clumped isotope record of individual limestone fabrics: A potential method to constrain the timing of oil migration. Chem Geol 616, 121245. https://doi.org/10.1016/j.chemgeo.2022.121245*

Chapter 5: "Constraining the kinetic parameters of calcite vs dolomite recrystallization in natural systems". This chapter focuses on the difference in clumped isotope records between calcite and dolomite and additional constraints can be placed on burial models. This includes the first report of correlation between dolomite cation ordering and the clumped isotope blocking temperature in natural samples.

This chapter has been reviewed in Geochimica et Cosmochimica Acta. It will be moved and submitted to Earth and Planetary Science Letters as per the recommendation of the editor:

Adlan, Q., Kaczmarek, S.E., John, C.M. *Constraining the kinetic parameters of calcite vs dolomite clumped isotope reordering during burial diagenesis.*

Chapter 6: "Conclusions, wider implications and future research directions". This chapter ties studies in chapters 3, 4 and 5 together to discuss how effective the clumped isotope thermometer can be in the modelling of thermal histories in recrystallized carbonate formations and suggestions for future research.

CHAPTER 2

THEORETICAL BACKGROUND AND METHODOLOGY

2.1   Theoretical background

2.1.1   Carbonate clumped isotope thermometry

The principle of clumped isotopes is that the two heavy isotopes of oxygen and carbon will preferentially bond ("clump") together in carbonate ions within a mineral lattice, and the abundance of this clumping is temperature-dependent (Eiler and Schauble, 2004; Ghosh et al., 2006; Eiler, 2007; Ghosh et al., 2007; Eiler, 2011). The rare ^{13}C and ^{18}O in the CO_2 molecules (i.e. $^{13}C^{18}O^{16}O$) used in this thermometry differ from the common isotopes (^{12}C and ^{16}O) because of the presence of one and two additional neutrons in their nucleus, respectively, which increases the mass. In the CO_2 molecules, the bonds containing both ^{13}C and ^{18}O are more stable thermodynamically than the common isotopes (Ghosh et al., 2006; Eiler, 2007). Due to changes in enthalpy (decreases with increasing temperature), the $^{13}C^{18}O^{16}O$ isotopologues become rarer for carbonates formed at high temperatures relative to the number predicted by probability (Ghosh et al., 2006; Eiler, 2007). Thus, the excess of $^{13}C^{18}O^{16}O$ isotopologues (mass 47) in carbonate minerals provides a direct estimate of the temperature of mineral crystallization (or re-crystallization). The difference between clumped isotope thermometry and traditional ($\delta^{18}O$) oxygen isotope thermometry is that clumped isotopes can be used to directly determine the carbonate mineral precipitation temperature without relying on the oxygen fluid composition ($\delta^{18}O_{fluid}$) from which the carbonate minerals developed (Eiler, 2007). For the stochastic abundance of CO_2 isotopologues in the atmosphere at 25°C, see Eiler (2007).

Measuring clumped isotopes in carbonates is not performed on the minerals, but on the CO_2 produced by the reaction of the mineral with H_3PO_4 acid. The ratios of CO^{2+} ions of different masses are determined for this CO_2 using a modified mass spectrometer that can measure mass-47 CO_2 (mostly $^{13}C^{18}O^{16}O$). During the measurement process, the mass 48 and sometimes mass 49 of CO_2 are also used as a screen for contaminants (Huntington et al., 2009; John and Bowen, 2016). The Δ_{47} notation (in per mil ‰) is used to represent the relative difference between the mass 47 abundance in CO_2 from acid digestion versus mass 47 abundance expected from stochastic distribution (Eiler, 2007; Ryb et al., 2017). Only then can a calculation of temperature ($T(\Delta_{47})$) be performed (Anderson et al., 2021b) using the Δ_{47} value of CO_2 released from phosphoric acid digestion of carbonate using an empirical calibration of the carbonate reference frame (i.e. CDES by Dennis et al. 2011). Recently, a new calibration was derived using carbonate anchor values from the InterCarb experiment (I-CDES, (Bernasconi et al., 2021), to overcome differences in data correction and variability in acid fractionation factors between laboratories (Anderson et al., 2021b).

6

2.1.2 Clumped isotopes (Δ_{47}) to constrain thermal histories of sedimentary basins

The application of carbonate clumped isotope paleo-thermometry has increased in recent years, especially in burial history reconstruction of carbonate formation in sedimentary basins (Dennis and Schrag, 2010; Huntington et al., 2010; Passey and Henkes, 2012; Lechler et al., 2013; Snell et al., 2013; Garzione et al., 2014; Fan et al., 2014; Stolper and Eiler, 2015; Winkelstern and Lohmann, 2016; Gallagher et al., 2017; Lloyd et al., 2017; John, 2018; Lawson et al., 2018; Mangenot et al., 2018; Lacroix and Niemi, 2019; Ingalls, 2019; Veillard et al., 2019; Naylor et al., 2020; Quade et al., 2020; Xiong et al., 2020; Ryb et al., 2021; Hemingway and Henkes, 2021). There are two mechanisms for the carbonate clumped isotope compositions (Δ_{47} values) of carbonate rocks to be altered during the burial–exhumation process: recrystallization via dissolution/re-precipitation and solid-state reordering of C-O bonds (Henkes et al., 2014; Stolper et al., 2018).
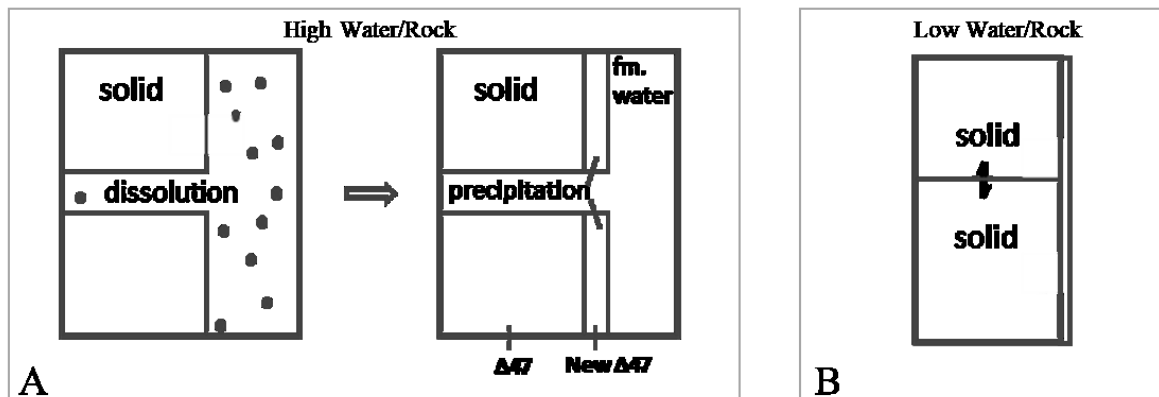
Figure 2.1 Simplified illustration of partial recrystallization via dissolution and precipitation and its newly formed Δ_{47} values (A); and isotopic exchange via solid-state reordering of C-O bonds (B).

During burial, elevated formation temperatures increase the rates of chemical reactions and ionic diffusion within carbonate minerals (Moore, 2001). This event changes the thermodynamic stability of the carbonate minerals being dissolved or precipitated (Flügel, 2010). All reactions during burial diagenesis are essentially aqueous dissolution-(re)precipitation reactions. The outside environment and the carbonate lattice undergo mass transfer reactions during this recrystallization process (Stolper and Eiler, 2015). Recrystallization via dissolution/re-precipitation in aqueous conditions can be shown as the following simple reactions:

Calcite $\qquad\qquad\qquad\qquad CaCO_3 \ (s) \rightleftharpoons Ca^{2+} + CO_3^{2-}$ $\qquad\qquad\qquad\qquad$ (2.1)

Dolomite $\qquad\qquad\qquad\qquad MgCa(CO_3)^2 \ (s) \rightleftharpoons Mg^{2+} + Ca^{2+} + 2CO_3^{2-}$ $\qquad\qquad$ (2.2)
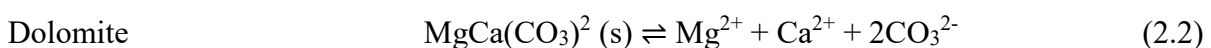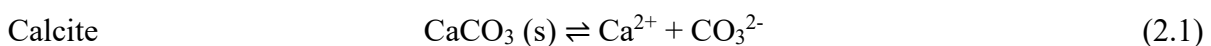
The isotopic exchange reactions can be initiated by the introduction of a sufficient (or high) influx of fluid into the carbonate formations to create a water-buffered system (or open system in another study). Complete recrystallization in a water-buffered system will lead to a resetting of the clumped isotope compositions (Δ_{47}) of the rocks reflecting the ambient burial temperature and, depending on the water to rock ratio, $\delta^{13}C$ and $\delta^{18}O$ values may also be altered (Dale et al., 2014; Beckert et al., 2016; Lawson et al., 2018; Bergmann et al., 2018b; Ryb and Eiler, 2018; Stolper et al., 2018; John, 2018; Ingalls, 2019; Veillard et al., 2019; Lukoczki et al., 2020; Ryb et al., 2021).

In cases where there is no fluid influx into the carbonate formations and or when the mass of fluid phase in contact with rock is limited due to a low porosity and permeability environments, the isotope-exchange reactions in this low water-rock conditions happen in a rock-buffered system. In this system, the $\delta^{13}C$ and $\delta^{18}O$ compositions of the recrystallized rocks may not change, but the clumped isotope compositions (Δ_{47}) will be altered via isotopic reordering, either through direct dissolution-precipitation processes, or through a process known as 'solid-state reordering'. The process of solid-state reordering is initiated internally by the diffusive migration of C or O to new lattice coordinates within the solid mineral driven by temperature elevation (Dennis and Schrag, 2010; Passey and Henkes, 2012; Stolper and Eiler, 2015; Brenner et al., 2018; Lloyd et al., 2018; Ryb et al., 2021). The empirical evidence of this bond reordering derives from the fact that non-first-order kinetics were found in: 1) brachiopods (Henkes et al., 2014; Shenton et al., 2015), 2) carbonatites (Dennis and Schrag, 2010; Stolper and Eiler, 2015), and 3) marbles and sedimentary rock alteration along dikes (Finnegan et al., 2011; Lloyd et al., 2017; Ryb et al., 2017). The solid-state bond reordering can be shown as the following simple reactions (Passey and Henkes, 2012; Henkes et al., 2014):

$$Ca^{13}C^{16}O_3 + Ca^{12}C^{18}O^{16}O_2 \leftrightarrow Ca^{13}C^{18}O^{16}O_2 + Ca^{12}C^{16}O_3 \qquad (2.3)$$
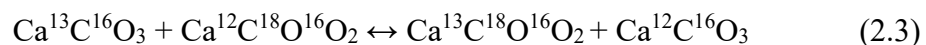
In simple terms, this temperature-dependent reaction can be defined as a disorder-order homogeneous equilibrium (Henkes et al., 2014). This study demonstrates that the first period of clumped isotope reordering is 'inactive', coinciding with early burial (shallow depth), and it maintains the initial $T\Delta_{47}$ value (Henkes et al., 2014). This first phase is followed by activation of reordering above 120˚C for several million years (figure 2.2). It has been observed that the $T\Delta_{47}$ increases slowly before eventually approaching equilibrium with the burial environment (Henkes et al., 2014). The following is a simplified illustration of the Δ_{47} mechanism in relation to the reordering process and burial process:
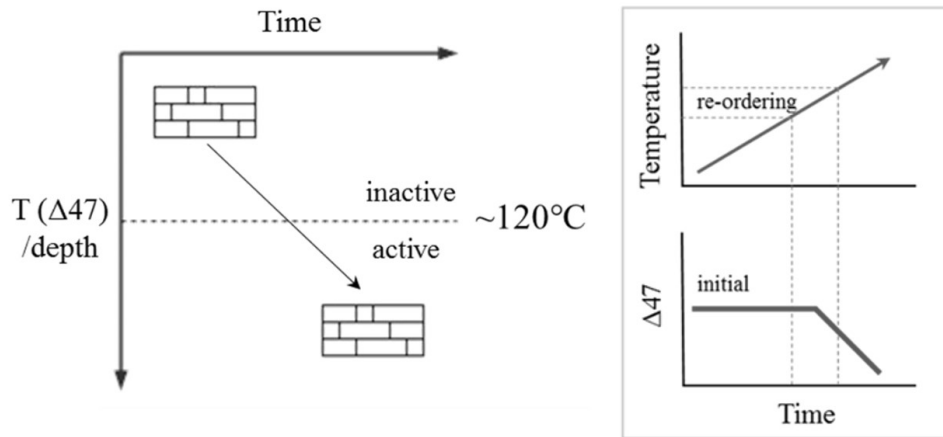
Figure 2.2. Simplified illustration of solid state ordering during burial (Henkes et al., 2014)

During the cooling process, the carbonate mineral may pass through the closure temperature of ~120°C and enter a point where the reordering process is inactive (Henkes et al., 2014), the reordering process is stopped, and the mineral 'locks in' an apparent $T\Delta_{47}$ value (Figure 2.3).
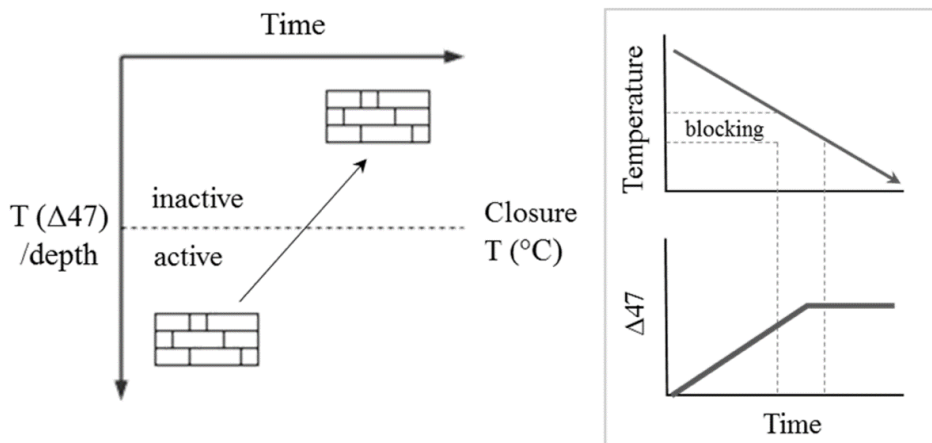
Figure 2.3. Simplified illustration of solid state ordering during exhumation (Henkes et al., 2014)

The isotope-exchange reactions via dissolution-precipitation processes (water-buffered and rock-buffered systems) and via solid-state reordering can impact any carbonates that experience burial diagenesis including any rocks that contain carbonate cements or veins. In the case of exhumed carbonate formations, where solid-state reordering dominates, the temperature measured through the clumped isotope thermometer may record 'apparent/blocking temperatures' (Passey and Henkes, 2012; Stolper and Eiler, 2015; Ryb et al., 2017) that are neither related to the original formation temperature nor the recrystallization (or maximum burial) temperature (Stolper and Eiler, 2015; Ryb et al., 2017). One previous study suggested that diagenetic alteration (i.e., recrystallization) at peak burial and during exhumation had no impact on the final blocking temperature recorded in the

carbonate minerals as the final blocking temperature mainly depends on the cooling rate (Stolper and Eiler, 2015).

Several laboratory heating experiments have been conducted to try to understand the solid-state reordering of carbonate minerals. So far, kinetics studies, through controlled heating experiments, have been conducted on calcite (Passey and Henkes, 2012; Henkes et al., 2014; Stolper and Eiler, 2015; Brenner et al., 2018), dolomite (Lloyd et al., 2018), and aragonite (Chen et al., 2019). The kinetic parameters from these heating experiments were used by geoscientists to model and predict the change in Δ_{47} from an initial value in response to an imposed thermal history. This in turn constrains the burial–exhumation process of carbonate formations.

2.1.3   Fluid–rock interaction

Fluid–rock interaction refers to the isotopes and /or elements exchanges that occur at increasing temperatures between fluids and minerals (Hurai et al., 2015; Simon et al., 2017). This interaction involves combinations of dissolution–precipitation, chemical exchange reactions and diffusion controlled mainly by the water: rock ratios (Hoefs, 2015; Hurai et al., 2015). In detail:

- In the dissolution-precipitation process, smaller grains dissolve and recrystallize on the surface of larger grains, decreasing the overall surface area and lowering the system's total free energy (Hoefs, 2015). The isotopic exchange between mineral and fluid occurs while the material is in solution.
- A chemical reaction between fluid and rock occurs as the chemical activity of one component between fluid and solid is contrastingly different from each other (Hoefs, 2015). The breakdown of a finite portion of the original crystal and the formation of new crystals is implied, which would form at or near isotopic equilibrium with the fluid (Hoefs, 2015).
- Diffusion process isotopic exchange occurs at the interface between the crystal and the fluid with little or no change in the morphology of the reactant grains or minerals (Hoefs, 2015).

The nature of interactive processes between fluid and rock in porous media can be quantitatively predicted using diagenetic models that utilize the principle of the stable isotope exchange of $^{18}O/^{16}O$ (Taylor Jr, 1977; Gregory and Taylor Jr, 1981), D/H (Taylor, 1978; Sakai et al., 1990) and $^{87}Sr/^{86}Sr$ ratios at equilibrium (Simon et al., 2017). This diagenetic modelling has become a common practice that aims at predicting the relevant diagenetic processes in carbonate formations (Banner and Hanson, 1990; Nader et al., 2015).

The first attempts to quantify isotope exchange processes in fluid-rock interaction were performed by Sheppard et al. (1971) and Taylor (1974) using a simple closed-system material balance equation to calculate cumulative fluid/rock ratios.

$$W/R = \frac{\delta_{rock_f} - \delta_{rock_i}}{\delta_{H_2O_i} - (\delta_{rock_f} - \Delta)} \quad ,\text{where } \Delta = \delta_{rock_f} \delta_{H_2O_f} \text{ (Hoefs, 2015)} \qquad (2.4)$$

The system's initial (i) and final (f) isotopic states are required for the equation above, assuming the interaction of rock with fluid as one finite volume. Mass balance equations are generally used for a diagenetic modelling to calculate the simultaneous changes in stable isotope values and elemental abundances that occur during fluid-rock interaction (Nader et al., 2015; Simon et al., 2017). The results then allow the direct comparison of a variety of geochemical data regarding testing models for diagenesis (Banner and Hanson, 1990). One key feature of this approach is that the relative values of water: rock ratios of the diagenetic system can be predicted (Banner and Hanson, 1990). However, the absolute values for fluid: rock ratios determined by mass balance methods may not be directly applicable to the parameters of natural diagenetic systems (Banner and Hanson, 1990).

In the absence of elemental abundance data, the nature of fluid-rock interaction recorded in carbonate rocks can also be understood by modelling the isotopic exchange trajectories in the minerals regarding the systems (Gregory et al., 1989) (Figure 2.4).
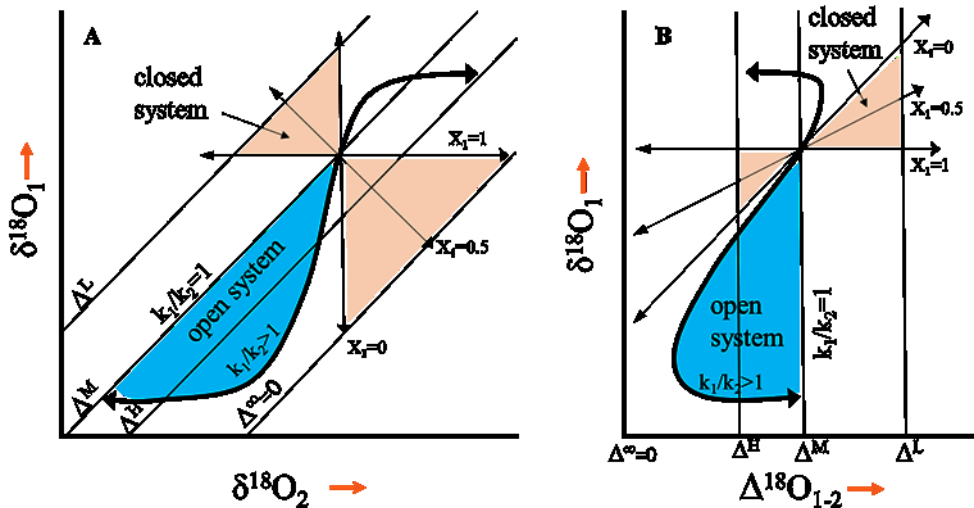
Figure 2.4. The systematics of stable-isotope exchange trajectories between minerals and fluids in the context of mass balance considerations are shown in δ-δ and δ-Δ spaces, both in closed and in open systems (Gregory et al., 1989). The figure on the right (b) is an exact transformation of the figure on the left (a), where mineral-1 is assumed to be the one that concentrates the heavy isotope at equilibrium (Δ), x_1 is the two-phase closed-system exchange trajectories, and k_1/k_2 is the relative exchange rate (see Gregory et al., 1989).

Fluid-rock interactions can take place in four different types of systems following Criss et al. (1987): (1) True, fluid-absent closed systems, in which isotopic exchange effects are constrained to occur only among coexisting mineral phases; (2) Closed systems as a limited type of open system, where interactions may occur between mineral phases and a coexisting fluid; (3) Open systems, where complex isotopic interactions occur between a mineral and a progressively infiltrating, externally-derived fluid, such that the fluid/rock ratio increases with time, and (4) "Buffered" open systems, or reservoir-controlled systems, which comprise a particular case where the fluid flux is large compared to the mineral-fluid exchange rates (Criss et al., 1987). This thesis will refer to open systems types 3 and/ or 4 as water-buffered systems; refer to type 2 closed systems as rock-buffered systems, and refer to the fluid-absent closed-system type 1 as a solid-state reordering system (see previous sub-Chapter 2.1.2).

In subsurface conditions, the $\delta^{18}O$ values of the formation waters are controlled mainly by the exchangeable mineral-oxygen reservoir and the temperature (Sheppard, 1984; 1986). Thus, the application of $\delta^{18}O$ versus a temperature plot for the formation waters has been used to understand this fluid-rock interaction (Sheppard, 1986). At a low water: rock ratio, oxygen in the surrounding rock dominates over the oxygen in the fluid, thus resulting in a change in the fluid isotope ratio (Hurai et al., 2015). The trajectory of oxygen change in the fluid (i.e. $\delta^{18}O$ fluid enrichment) in this rock-buffered system can be recognized in the $\delta^{18}O$ vs temperature plot: for example, the $\delta^{18}O$ fluid enrichment of calcites in Palmarito, the Bird Spring Formation, Venezuela (Shenton et al., 2015) and the Marion Plateau dolomites (Veillard et al., 2019). In the opposite case of a high water: rock ratio, the rock isotope ratio ($\delta^{18}O$ mineral) becomes modified (Sheppard, 1986; Hurai et al., 2015). The trajectory of oxygen change in minerals in this water-buffered system has also been recognized in the $\delta^{18}O$ vs temperature in the diagenetic studies of Arabian Gulf Coast carbonates (Sheppard, 1986) and the Palmarito Formation, Venezuela (Shenton et al., 2015).

2.1.4 Inhibition of diagenetic processes in carbonate formation by petroleum

Subsurface fluids play a critical role during the diagenesis of carbonate reservoirs as they can dissolve and re-precipitate cement, and act as transporting mediums during this process. Consequently, the presence of hydrocarbons, which are also a fluid, can significantly affect diagenesis. The inhibition by petroleum of the diagenetic process in a subsurface rock formation was initially suggested after porosity preservation was recognized in a sandstone reservoir (Johnson, 1920). In carbonate formations, it was found that the porosity and permeability showed systematic declines from crest to flank and occasionally abrupt changes at the petroleum water contact level, also suggesting a

diagenetic inhibition by petroleum (e.g., Feazel and Schatzinger, 1985; Gluyas et al., 1993; Neilson et al., 1998). The topic of the inhibition effect of oil emplacement on carbonate reservoirs has remained a subject of interest with numerous reviews and investigations arising in various case studies (Friedman and Sanders, 1978; Epstein and Friedman, 1983; Feazel and Schatzinger, 1985; Mitterer and Cunningham, 1985; Oswald et al., 1995; Nielson et al., 1998; Worden et al., 1999; Heasley et al., 2000; Bloch et al., 2002; Ehrenberg and Nadeau, 2005; Cox et al., 2010; Kolchugin et al., 2016).

The pores in carbonate petroleum reservoirs are first filled with formation water before petroleum enters and displaces it. During and after the petroleum charge, some water content in this reservoir, known as irreducible water saturation (S_{wi}), persisted even when the whole reservoir structure was filled with petroleum. This water saturation might contribute to the diagenetic process and is known to be controlled by the wettability of the petroleum-water-rock system (Worden, 1999).

The word wettability is described as the preference of a rock to be in contact with one type of fluid rather than another (e.g., water-wet reservoir or oil-wet reservoir) that controlled by a surface energy thermodynamic (Figure 2.5). This wettability is contingent upon the hydrocarbon composition, the water salinity and chemistry of rock formation, the asphaltene content, the reservoir fabric, the abundance of iron-bearing minerals, and the petroleum column height in the reservoir (Worden, 1999).
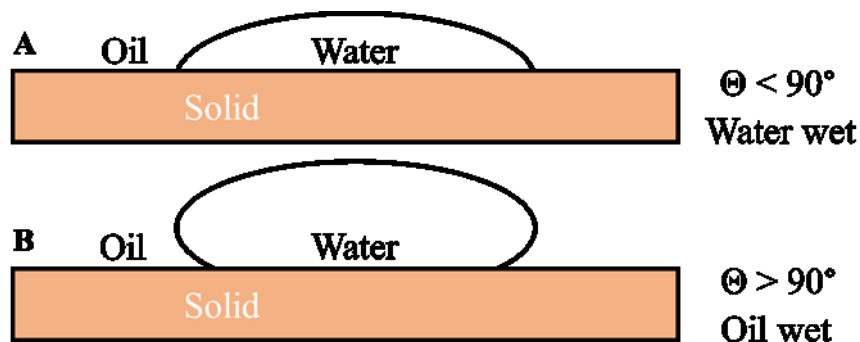
Figure 2.5. Wettability of a rock surface (Schön, 2015). A) Water-wet conditions, the mineral surface is coated with water, while oil and gas occupy the central position of the largest pores. B) Oil-wet conditions, the mineral surface is coated with oil, and the water is in the centre of the largest pores. The contact angle Θ is related to interfacial tension (Schön, 2015).

Wettability in carbonate reservoirs predicted to be generally oil-wet (Barclay and Worden, 2000; Cox et al., 2010). It is suggested that a thin film of oil formed around pore interiors of carbonate reservoirs as a result of the contact between positively charged calcite surfaces with the negative dipoles in oil (Cox et al., 2010; Worden, 1999). In this Oil-wet conditions, the mineral surface is coated with oil and the water is in the centre of the largest pores, the relative positions of oil and water are reversed with respect to the water-wet state (Schön, 2015).

From the physicochemical processes perspective, the effect of petroleum emplacement depends on the availability of surface area of minerals available for dissolution or precipitation (Worden, 1999), the saturation exponent (Murphy et al., 1989) and the flow rates of water (Worden, 1999). For example, the dissolution or precipitation process will be unaffected in fully water-wet systems where all the mineral surfaces are coated with water, even at high petroleum saturation (Worden, 1999). All in all, the effectiveness of the diagenetic process in carbonate formation in regard to its petroleum contents mainly depends on a wide variety of factors, such as the timing and level of hydrocarbon saturation and the wettability of the reservoirs (Worden et al., 1998; Kolchugin et al., 2016). This diagenetic inhibition can transpire once the physical or chemical coverage of mineral surfaces by petroleum or related organic compounds shield parts of the surfaces from access by diagenetic fluids. In addition, petroleum can also limit the aqueous phase flow and mass transfer processes which can reduce the effectiveness of the cementation process (Worden et al., 1998).

2.2   Methodology

There are three necessary stages to extract clumped isotope values from carbonate rocks, sequentially: gas extraction, purification and mass-spectrometer measurement (Huntington et al., 2009; Dale et al., 2014). The data results from these measurements are then processed and corrected before interpretation.

2.2.1 CO_2 extraction and purification

The Δ_{47}, $\delta^{18}O$ and $\delta^{13}C$ can only be measured from CO_2 produced by acid-digestion of rocks. Using powdered samples, the extraction of CO_2 was performed using 105% anhydrous orthophosphoric acid bath at 90°C under vacuum condition following McCrea (1950) and Swart et al. (1991). Depending on the carbonate mineral content, a total of 4-4.5mg of carbonate powder was required for the effective acid-digestion process. The reaction occurs as follows:

$$H_3PO_4 + XCO_3 \rightarrow CO_2 + H_2O + X^{2+} + + HPO_4^{2-} \qquad (2.5)$$
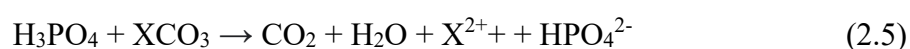
Where X is a metal cation (e.g. Ca^{2+}). This reaction was done for 10 minutes for calcite samples and longer for dolomite samples (i.e. 20 minutes). Throughout this period, extracted gases, including the product CO_2, were cryogenically trapped in a glass spiral trap, immersed in liquid nitrogen (LN_2) at -195.79 °C. The CO_2 was then purified to remove contaminant gases including water vapor.

With manual CO_2 purification in the stable isotope laboratory, the CO_2 gas from the acid-digestion stage was passed through several traps, sequentially: spiral cryogenic trap (multiple), silver trap and a static Porapak-Q (PPQ) glass U-trap before being transferred to the mass-spectrometer inlet valve. The

Porapak-Q trap used here was originally designed for use in gas chromatography columns separating polar gas from non-polar CO_2 (divinyl benzene polymer). The CO_2 was moved through the different traps using a pressure differential mechanism as a result of temperature differentiation (-195.79 °C, LN_2). Following acid-digestion, Trap-1 was used as cryogenic trap to remove condensable gas. The CO_2 was then released by heating the trap to -90°C and the gas was then passed through a ¼ inch diameter glass tube containing silver wool to remove sulphur molecule (Guo and Eiler, 2007; Eagle et al., 2010) and through the PPQ trap maintained at -35˚C. Transfer time across the PPQ trap was 60 minutes. The CO_2 was cryogenically trapped in Trap-3 before again being released by application of ethanol slush at 90˚C and frozen into a cold finger (Trap-4) for transfer to the mass spectrometer. The traps and metal tube lines were heated at 150°C under vacuum with a hot air gun to clean them before the next run was initiated. The manual purification method is only used in Chapter 3 to increase throughput.

For the automated CO_2 purification (IBEX), helium gas was used as a carrier using a trap configuration similar to the manual line. Samples were delivered to the acid reaction vessel by a rotating auto sampler while the extracted CO_2 was frozen down continuously. The CO_2 gas was released by heating the first trap to -80°C and then moving it across a 2.5 mm gas chromatography (GC) column held at -35°C, using helium as carrier gas. The CO_2 was then frozen in the second trap at -195.79 °C before being moved to a micro-volume container and finally transferred to the mass-spectrometer.

2.2.2   Mass Spectrometry

All measurements were performed in the stable isotope laboratory at Imperial College London using two Thermo Finnigan MAT-253 gas source IRMS systems, denoted 'Pinta' and 'Santa Maria' (Thermo Instruments Bremen, Germany). These mass spectrometers are equipped with dual inlet systems that allows determination of isotope ratios by introducing sample gas and reference gas of known isotopic composition into the mass spectrometer, alternately, under nearly identical pressure conditions (Huntington et al., 2009). High purity (HP) carbon dioxide was used as the reference gas with $\delta^{18}O$ and $\delta^{13}C$ values given in Chapters 3-5 in this study. For clumped isotopes measurement, additional cups for 44-49 m/z ions were registered in both mass-spectrometer (Eiler and Schauble, 2004). The majority of measurements used in this study were made on Pinta, unless stated elsewhere. Before each acquisition, peak centering and pressure adjustments were automatically carried out. Measurements consisted of eight acquisitions each with seven cycles with 26 s integration time. The bellow pressure was adjusted to approximately 45 mbar to generate a m/z 44 ion beam signal of roughly 15000 mV after the introduction of the sample to the mass spectrometer. The pressure was automatically adjusted

and maintained throughout the analysis to achieve the beam signal target. A typical acquisition time was around 2 hours.

2.2.3 Data processing

All calculations were made using the accessible and free software Easotope (John and Bowen, 2016). The process is initiated by calculation of the relative abundance ratios R_{13}, R_{17} and R_{18} using a known value of $\delta^{18}O$ and $\delta^{13}C$ of the working or reference gas (WG). The relative abundance of $^{13}C/^{12}C$, $^{17}O/^{16}O$, and $^{18}O/^{16}O$ of the reference gas are defined as:

$$R^{13}_{REF} = \left(1 + \left(\frac{\delta_{13C\ REF}}{1000}\right)\right) \times R^{13}_{VPDB} \tag{2.6}$$

$$R^{18}_{REF} = \left(1 + \left(\frac{\delta_{18O\ REF}}{1000}\right)\right) \times R^{18}_{VSMOW} \tag{2.7}$$

$$R^{17}_{REF} = \left(1 + \frac{R^{18}_{REF}}{R^{18}_{VSMOW}}\right)^{\lambda} \times R^{17}_{VSMOW} \tag{2.8}$$

Where R^{13}_{VPDB} is 0.01118, R^{18}_{VSMOW} is 0.0020052, R^{17}_{VSMOW} is 0.00038475 following Brand et al. (2010), and $\lambda = 0.528$ (Daëron et al., 2016). Abundances of ^{12}C, ^{13}C, ^{16}O, ^{17}O and ^{18}O were computed for the reference gas prior to calculating the isotopologue composition of the reference gas, mass 44-49 (R_{44}-R_{49} REF), assuming a stochastic distribution. For further details of these calculations see John and Bowen (2016).

After the isotopologue composition of the reference gas was determined, the isotopic composition of the sample gas ($\delta^{18}O$ SAMPLE and $\delta^{13}C$ SAMPLE) was then defined relative to the reference gas:
Where i = [44, 45, 46, 47, 48, 49]
The first step was to compute the abundance ratio (R_i SAMPLE) of m/z = i relative to m/z = 44 using voltage (V_i) value of m/z = i.

$$R^{17}_{REF} = \frac{(V_i/V_{44})\ SAMPLE}{V_i/V_{44})\ REF} \tag{2.9}$$

The second calculation step was to compute the abundance ratio of the different masses (δ_i):

$$\delta_{i\ SAMPLE} = \left(\frac{R\ i\ SAMPLE}{R\ i\ REF} - 1\right) \times 1000 \tag{2.10}$$

16

The third calculation step was to compute the abundance ratio of R_{18} SAMPLE (Assonov and Brenninkmeijer, 2003):

$$-3\,K^2(R_{18\,SAMPLE})^{2\lambda} + 2\,K(R_{45\,SAMPLE})\,(R_{18\,SAMPLE})^{\lambda} + 2(R_{18\,SAMPLE}) - R_{46\,SAMPLE} = 0 \qquad (2.11)$$

where,

$$k = (R\,^{17}REF)/(R\,^{18}REF)^{\lambda} \qquad (2.12)$$

The fourth calculation step was to compute the $\delta^{18}O$ SAMPLE:

$$\delta^{18}O_{\ SAMPLE} = \left(\frac{R^{18}\ SAMPLE}{R^{18}\ VSMOW} - 1\right) \times 1000 \qquad (2.13)$$

The fifth calculation step was to compute the $\delta^{13}C$ SAMPLE:

$$\delta^{13}C_{\ SAMPLE} = \left(\frac{R^{13}\ SAMPLE}{R^{18}\ VSMOW} - 1\right) \times 1000 \qquad (2.14)$$

where,

$$R^{13}_{\ SAMPLE} = R^{45}_{\ SAMPLE} - 2(R^{17}_{\ SAMPLE}) \qquad (2.15)$$

$$R^{17}_{\ SAMPLE} = k\,(R^{18}_{\ SAMPLE})^{\lambda} \qquad (2.16)$$

Then the final step was to compute the ratio of isotopologues in CO_2 SAMPLE as a stochastic distribution, before calculating the abundance ratio for CO_2 SAMPLE as the stochastic distribution of m/z=45,46,47 ($R_{m/z*}$SAMPLE):

$$R_{45}{}^*{}_{SAMPLE} = {}^{45}CO_2{\ SAMPLE} / {}^{44}CO_2{\ SAMPLE} \qquad (2.17)$$

$$R_{46}{}^*{}_{SAMPLE} = {}^{46}CO_2{\ SAMPLE} / {}^{44}CO_2{\ SAMPLE} \qquad (2.18)$$

$$R_{47}{}^*{}_{SAMPLE} = {}^{47}CO_2{\ SAMPLE} / {}^{44}CO_2{\ SAMPLE} \qquad (2.19)$$

The values of Δ_{47} of CO_2 can be calculated as (Eiler, 2007):

$$\Delta_{47}\,RAW = \left(\left(\frac{R47\ SAMPLE}{R47*\ SAMPLE} - 1\right) - \left(\frac{R46\ SAMPLE}{R46*\ SAMPLE} - 1\right) - \left(\frac{R45\ SAMPLE}{R45*\ SAMPLE} - 1\right)\right) \times 10^3 \qquad (2.20)$$

where $R_i = m_i / m_{44}$ or R_{47}, R_{48}, R_{49} are abundance ratios relative to mass 44. In summary, the main outputs of this data processing are $\delta^{18}O$, $\delta^{13}C$, and Δ_{47} RAW values. However, these values cannot be interpreted immediately and must be corrected for experimental effects.

2.2.4   Data corrections

There are three corrections to be applied to the raw data from previous calculations: drift correction, non-linearity correction and reference frame projection. The first correction was performed as the presence of contaminants in the isotope-ratio mass spectrometer can result in signal instability related to the ion source performance, known as a drift (D'Autry et al., 2010).

The drift was corrected by plotting the $\delta^{18}O$ and $\delta^{13}C$ raw data against the inter-laboratory published carbonate standards (ETH 1 to ETH 4) and internal standard (ICM) with their accepted isotopic values. For further details of the isotopic composition of these standards see Table 2.1.
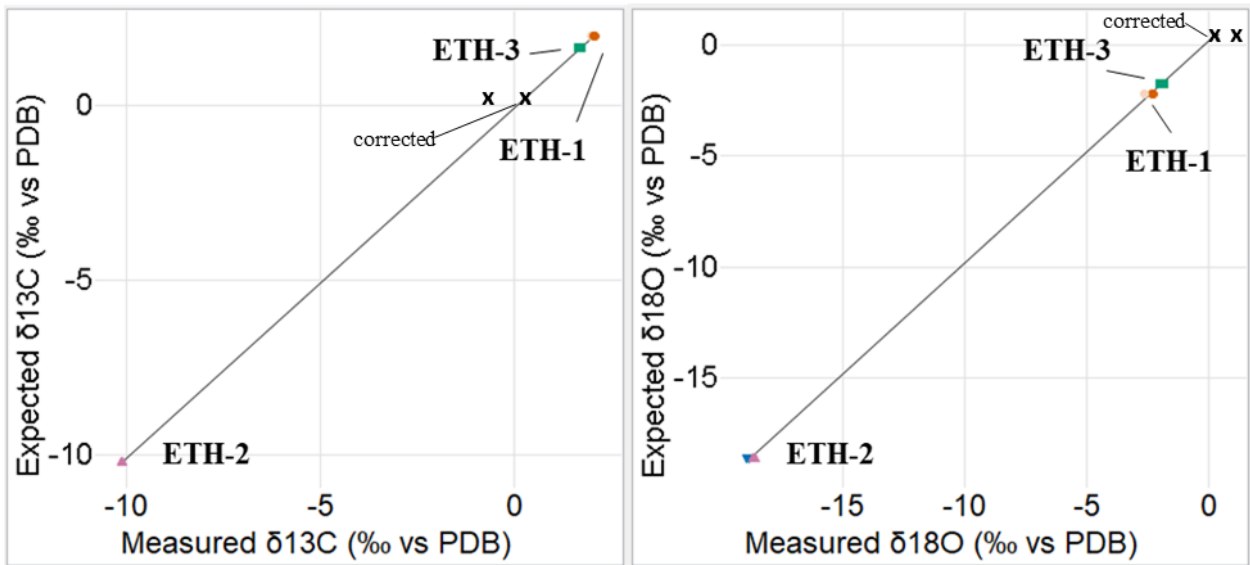
Figure 2.6 Example of linear regression for drift correction.

The carbonate standards data can then be linearly regressed (Figure 2.6). The corrected values of $\delta^{18}O$ and $\delta^{13}C$ ($\delta^{18}O$ CORRECTED and $\delta^{13}C$ CORRECTED) were obtained by applying the linear equation:

$$\delta^{18}O \text{ CORRECTED} = \text{slope} (\delta^{18}O \text{ MEASURED}) + \text{intercept} \tag{2.21}$$

$$\delta^{13}C \text{ CORRECTED} = \text{slope} (\delta^{13}C \text{ MEASURED}) + \text{intercept} \tag{2.22}$$

The next correction was for the non-linearity that exists for all mass-spectrometers that depends on the machine and changes over time as a function of cleanliness, filament, and tuning (Bernasconi et al., 2013). There are two methods generally applied to correct for this effect: the "heated gas correction"

(Huntington et al., 2009) and the "pressure base line correction (PBL)" (He et al., 2012; Bernasconi et al., 2013). In this study, the "heated gas correction" was used for the samples purified on the manual line and the "pressure base line correction (PBL)" for samples run on the auto-purification IBEX.

The heated gas correction (only used in Chapter 3) was achieved by measuring heated gases with a constant Δ_{47} value and a range of bulk isotopic composition ($\delta47$) prepared at the temperature of 1000°C following Huntington et al. (2009). In practice, gases are heated in a quartz glass tube for 2 hours at 1000°C before rapidly quenched at room temperature. The heated gas has a calculated Δ_{47} value of 0.027‰ (Wang et al., 2004). The positive linear correlation formed due to this linearity effect is defined as:

$$\Delta_{47} \, HG = slope \, (\delta_{47}) + intercept \qquad (2.23)$$

The pressure base line (PBL) was used for the sample purified with the automated IBEX line to optimize the non-linearity correction (He et al., 2012; Bernasconi et al., 2013). The PBL correction removes the effect of secondary electrons on the Faraday cup collectors. These secondary electrons create a negative baseline signal with an amplitude inversely proportional to the beam intensity. Following the approach of Bernasconi et al. (2013), daily scans were acquired using the reference gas, at different intensities, 12 kV to 17 kV in 1 kV steps on the *m/z* 44 beam. The negative intensity of the background was then plotted against the beam intensity. The regression then can be used to correct the sample intensity (Figure 2.7).
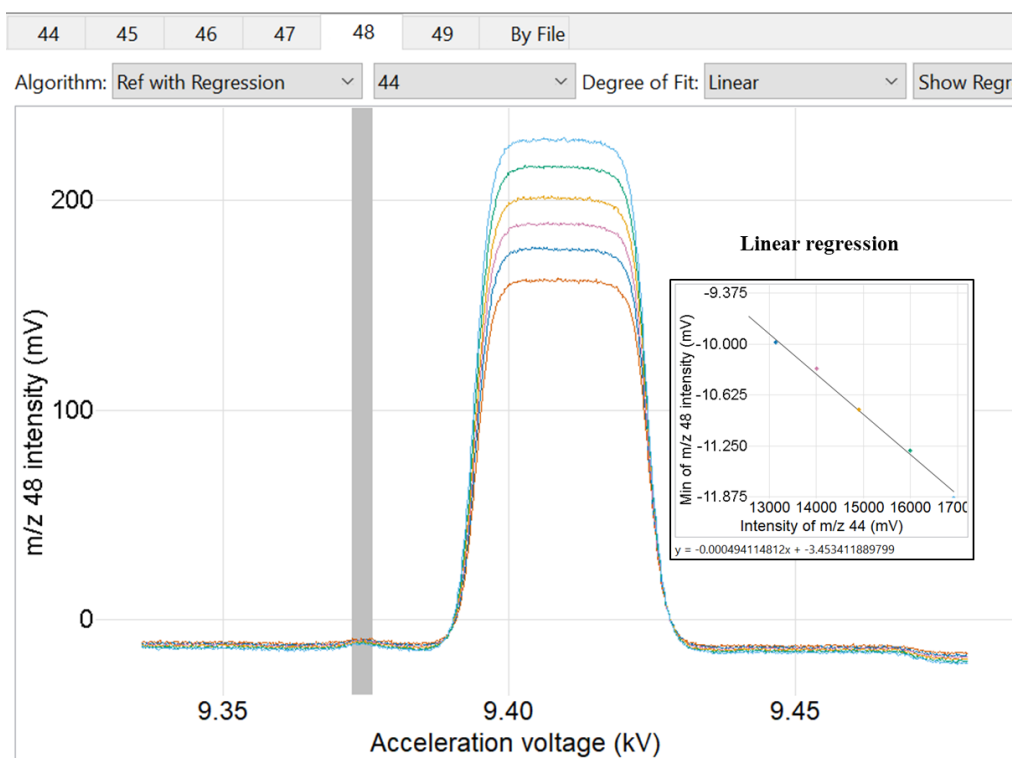
Figure 2.7 Scans run showing mass 47 intensities across acceleration voltages 9.36-9.39 kV (top) and linear regression between the background and the beam intensity.

For the last correction, the raw data were then projected into the inter-laboratory absolute reference frame or Intercarb Carbon Dioxide Equilibrated Scale (I-CDES) (Bernasconi et al., 2021) based on routinely measured ETH1, ETH2, ETH3, ETH4 and internal Carrara Marble (ICM) carbonate standards (Muller et al., 2017; Davies and John, 2019; Bernasconi et al., 2021). This correction, previously known as 'carbon dioxide equilibrated scale (CDES)', has been used to correct a scale compression by projecting the measurement results on carbonate standards to the known reported value scale (Dennis et al., 2011; Bernasconi et al., 2021). The carbonate clumped isotope values of the standards are reported relative to a carbonate reference frame uniquely defined by the absolute Δ_{47} values reported in Table 2.1 for ETH-1, ETH-2, and ETH-3 following Bernasconi et al. (2021).

Table 2.1 List of standards with its isotopic compositions following (Bernasconi et al., 2021).

Carbonate Standards	Δ_{47} (‰, I-CDES)	$\delta^{13}C$ (‰,VPDB)	$\delta^{18}O$ (‰,VPDB)
ETH-1	0.2052	2	-2.19
ETH-2	0.2085	-10.2	-18.58
ETH-3	0.6132	1.67	-1.75
ETH-4	0.4505	-10.22	-18.67
ICM (internal)	0.291	2.02	-1.82
IOL (internal)	0.636	0.3	0.38

2.2.5 Metrics of contaminations

Radicals and ions in the 44-46 mass range (e.g. NO2) can produce isobaric effects on $\delta^{13}C$ and $\delta^{18}O$ measurements in a mass spectrometry (Adlan et al., 2020). Molecular species such as $^{32}S^{16}O^-$, $^{15}N^{16}O2$, $^{15}N^{14}N^{18}O$, $^{14}N^{15}N^{18}O$, CH_2Cl_2, C_5H_{12}, CCl^+ (e.g. produced from CH_3Cl or CH_2Cl_2) have similar molecular weight to masses 48 and 49 of CO_2 (Huntington et al., 2009;Eiler and Schauble, 2004), and lead to isobaric interferences with the mass 47 of CO_2 (Adlan et al., 2020). This isobaric effect can significantly impact clumped isotope measurements (Davies and John, 2017).

The offset in the Δ_{48} value of a sample from δ_{48} vs. Δ_{48} heated gas regression lines was used to detect the presence of contaminants that may fall within the range of the mass 47 isotopologue. The Δ_{48} may be calculated in an analogous fashion to Δ_{47}. The standard procedure in the Stable Isotope Laboratory at Imperial College London was to apply a cut off value of $\Delta 48$ offset > 1.5 and 49 parameter > 0.2 (John and Bowen, 2016), above which samples are considered as contaminated.

2.3   Summary

The carbonate clumped isotope thermometry is one of the best techniques to assess carbonate rocks' thermal history and diagenesis. The value of clumped isotope compositions in the carbonate rocks varies depending on recrystallization and solid-state reordering processes in relation to its thermodynamic system. The processes of extracting the clumped isotope value involve the CO_2 extraction from carbonate samples, purification process and measurement in a mass spectrometer before the data can be processed in Easotope software.

One advantage of this technique is that it can directly determine the mineral precipitation temperature without relying on the oxygen fluid composition. Therefore, the diagenetic process, including its fluid–rock interaction, can be examined. In the subsurface condition, the effectiveness of this diagenetic process may be interrupted or stopped by petroleum. It depends on a wide variety of factors, such as the timing and level of hydrocarbon saturation as well as the wettability of the reservoirs. The subject of carbonate diagenesis and its fluid-rock interaction with clumped isotopes will be discussed in Chapters 4 and 5, while the diagenetic interruption by petroleum will be discussed in Chapter 4 of this thesis.

CHAPTER 3

PETROLEUM CONTAMINANT IN CARBONATE ROCKS AND HOW TO SAFELY CLEAN IT

3.1 Introduction

Since the introduction of carbonate clumped isotope thermometry more than a decade ago, the number of laboratories, as well as the number of geoscience applications using this technique, has grown rapidly. The naturally-occurring, multiply-substituted isotopologues ('clumped isotopes') of ^{13}C and ^{18}O are ideal for paleotemperature reconstruction since no information on the oxygen isotope composition of the water is required (Ghosh et al., 2007). Carbonate clumped isotopes have been used in numerous applications such as burial history reconstruction (Dennis and Schrag, 2010; Passey and Henkes, 2012; Henkes et al., 2014; Huntington and Lechler, 2015; Shenton et al., 2015; Gallagher et al., 2017; Ryb et al., 2017; John, 2018; Mangenot et al., 2018), carbonate diagenesis (Huntington et al., 2011; Loyd et al., 2012; Dale et al., 2014; Millan et al., 2016), constraining the conditions for dolomitization (Ferry et al., 2011; Beckert et al., 2016; Veillard et al., 2019; Lukoczki et al., 2019), reconstructing subsurface fluid flow (Budd et al., 2013; Lu et al., 2017; Lu et al., 2018), estimating the burial pressure regime of carbonates (Honlet et al., 2018), reconstructing past glacial/interglacial temperature variations (Affek et al., 2008; Meckler et al., 2015), constraining uplift rates on continents (Huntington et al., 2010) and estimating fault-related temperature and fluid composition (Swanson et al., 2012).

As carbonates are widespread minerals that can easily be found in sedimentary basins and crystalline rock complexes, further applications of this technique can provide important information on conditions for economic mineral deposits (del Real et al., 2016; Mering et al., 2018) and characterization of hydrocarbon reservoirs (Vandeginste et al., 2014; MacDonald et al., 2015). A wide range of applications implies a wide range of sample types used for clumped isotopes and therefore it has become increasingly more important to evaluate possible sources of uncertainties related to sample contamination. The most common problem in the stable isotopic measurements, beside the presence of water, is the presence of hydrocarbon (e.g., bitumen) and adhering organic material, which can affect both the measurement of carbonate clumped isotopes (MacDonald et al., 2015; Davies and John, 2017) as well as conventional bulk isotope measurements (Wierzbowski, 2007; Fallet et al., 2009; Roberts et al., 2018). This organic component can react with phosphoric acid (H_3PO_4) during acid digestion and generate molecular gaseous species which have similar molecular weights to the carbon dioxide molecules. These radicals and ions in the 44-46 mass range (e.g. NO_2) produce isobaric effects that interfere with the mass spectrometric determination of $\delta^{13}C$ and $\delta^{18}O$. Molecular species such as

$^{32}S^{16}O^-$, that have similar molecular weight to mass 48 and 49 of CO_2 (Huntington et al., 2009) (and $^{15}N^{16}O_2$, $^{15}N^{14}N^{18}O$, $^{14}N^{15}N^{18}O$, CH_2Cl_2, C_5H_{12}, CCl^+ produced from CH_3Cl or CH_2Cl_2 (Eiler and Schauble, 2004)) lead to isobaric interferences with the mass 47 of CO_2. For masses in the *m/z* range of 47-49, these effects are several orders of magnitude more important due to the low abundance of the corresponding naturally-occurring isotopologues, and this significantly impacts clumped isotope measurements (Davies and John, 2017).

In the field of conventional bulk isotope analysis, it has become a common practice to perform a treatment to remove organic matter (Epstein et al., 1951; Epstein et al., 1953; Durazzi, 1977; Goreau and Yonge, 1977; Lister, 1988; Boomer, 1993; Curtis et al., 1993; Wierzbowski, 2007; Lebeau et al., 2014). Low-temperature oxygen plasma ashing (OPA) is a well known method used for removing organic matter from samples using ionized oxygen (Bird et al., 2010; Lebeau et al., 2014) with a working temperature range of 60-70 °C (Pike et al., 1989). The effect of low-temperature OPA treatment on the initial bulk isotopic composition has been demonstrated as being negligible or within the bounds of analytical error (Goreau and Yonge, 1977). For example, a recent study indicated that low-temperature OPA treatment produced a maximum change of the initial bulk isotopic value of +0.30‰ for $\delta^{13}C$ and -0.12‰ for $\delta^{18}O$ value for a 2-6 hours 125°C treatment (Roberts et al., 2018).

For carbonate clumped isotope measurements, cleaning of CO_2 from volatile organic contaminants generated by acid digestion is typically achieved through a static Porapak-Q trap held under vacuum at temperatures below 0˚C (Huntington et al., 2009; Davies and John, 2017). However, there are some indications that the Porapak-Q trap is not sufficient to clean samples with abundant organic radicals during the purification process. Although it was not discussed in detail in previous publications, raw data from a previous clumped isotope study (MacDonald et al., 2015) performed in Imperial College lab showed that contamination issues could radically be reduced by using OPA treatment on organic-rich samples, as indicated by lower Δ_{48} offset and 49 parameter after OPA treatment. However, no study to date has systematically investigated potential fractionation effects that low-temperature OPA could cause on the initial Δ_{47} values of carbonates. For instance, in the previously cited study (MacDonald et al., 2015), a Δ_{47} lowering of 0.011-0.040‰ was observed and attributed to the OPA-treated samples being free of contaminants (contamination results in positive isobaric effects on mass 47), but it is also possible that the change was due to a secondary alteration of the initial Δ_{47} value.

Here, results are presented of a study specifically designed to test whether OPA treatment has an impact on clumped isotope values. This is critical because clumped isotopes rely on high-resolution measurement and even small offsets could significantly bias the temperatures derived from this technique.

3.2   Materials and methods

3.2.1   Materials

In order to test the effects of OPA treatment, three natural samples were selected with a large range of initial Δ_{47} values: an internal "Oamaru limestone" standard (IOL), a sample of vein calcite from Jabal Madar, Oman (JMF-6A), and the internal Carrara marble standard (ICM). The IOL samples were previously documented as 'least cemented homogeneous Oligocene Limestones' and characterized by a $\delta^{18}O$ value between 0‰ and 1‰ PDB and $\delta^{13}C$ value between 0‰ and 1.5‰ PDB (Nelson and Smith, 1996). The JMF-6A samples were previously documented as 'macro-columnar calcite' with a $\delta^{18}O$ value between -16‰ and -12‰ VPDB and a $\delta^{13}C$ value between -8‰ and -2‰ VPDB (Vandeginste et al., 2017).

Both IOL and ICM have been routinely measured as calcite standards on the instruments at Imperial College London. The JMF-6A calcite sample was never used as reference materials or carbonate standards. This JMF-6A sample was selected based on its isotopic homogeneity, and the Δ_{47} value being intermediate between IOL and ICM. The samples were crushed with an agate mortar and pestle, then sieved through a 125 µm sieve. Fourier Transform Infrared Spectroscopy (FT-IR-Spectrometer Nicolet 5700) was used to ensure the samples were homogeneous and to qualitatively estimate the mineralogy of JMF-6A and IOL. The Δ_{48} offset value of IOL and JMF-6A is respectively 0.044‰ and 0.038‰ on average, while the 49 parameter is respectively 0.177 and 0.131 on average. The choice of a wider range of Δ_{47} values was driven by the need to test whether the oxygen reagent-isotopic exchange impacted the carbonates, and whether this impact was proportional to the clumped isotope composition of the sample. The Δ_{47} CDES value of IOL is 0.732 ± 0.005 ‰ (n=11), of JMF-6A is 0.629 ± 0.008 ‰ (n=10), and of ICM is 0.411 ± 0.003 ‰(n=21).

3.2.2   Testing treatment times of 10, 20, 30 and 60-minutes with OPA

All powdered samples were weighed to 20 mg before being sprinkled evenly on a petri dish 60 mm in diameter with a side (wall height) of 15 mm to ensure a maximum surface area of mineral exposed to the plasma treatment. The petri dish was placed into the 100 mm diameter x 280 mm length chamber of a Henniker Plasma HPT-100 (Henniker Scientific) and treated with low-temperature plasma ashing under oxygen at a flow rate of 46 mL/min and a power of 100 W, with a vacuum condition of 0.2 mbar before gas flow, and increasing to 2 ± 0.05 mbar during the treatment with gas in the chamber. The HPT-100 used in this study was the same instrument used to effectively remove organic contaminants in previous studies within 5 minutes (MacDonald et al., 2015) and 40 minutes (2 x 15-20 minutes, with

shaking and 5 minutes resting time between OPA treatments) (Davies and John, 2019). As a consequence, OPA treatment times of 10, 20 and 30 minutes were tested in this study to see if OPA impacted the Δ_{47}, and potentially the $\delta^{18}O$, $\delta^{13}C$, Δ_{48} offset and 49 parameter of the samples.

The instrument specification comparison shows that the power source used in the HPT-100 in this study was 50W lower than the POLARON PT7160 used for the previous organic matter removal experiment (Lebeau et al., 2014). The lower power of the Henniker Plasma HPT-100 generates lower radio frequency (RF), which yields a lower oxidation potential (Bird et al., 2010) of O_2^+, O, O_2, O^- (Dai, 1996) and electrons to reacts with the sample surface. Based on three temperature measurements, the working temperature inside the plasma chamber of the Henniker Plasma HPT-100 ranged between 65-70 ºC after 30 minutes, 57-60 ºC after 20 minutes and 37-43 ºC after 10 minutes. The temperature was measured on the petri dish surface using a wire probe-digital thermometer, 3-5 seconds after the plasma treatment finished, thus the actual temperatures probably were slightly higher (~5 ºC). The chamber temperature is lower than the 125 ºC reported for the plasma chamber in a similar bulk stable isotope cleaning experiment (Roberts et al., 2018). The lower chamber temperature is favourable as clumped isotopes are susceptible to reordering at elevated temperatures (Dennis and Schrag, 2010; Henkes et al., 2014). The actual plasma chamber temperature of the POLARON PT7160 used by Lebeau et al. (2014) is unknown, however the technical information from the product manual book suggests 10-35 ºC in 95% maximum humidity. This previous cleaning study (Lebeau et al., 2014) used a treatment duration of 300 to 1860 minutes prior to stable isotope measurement. In this study, the main part of plasma experiment focused on the detection of alteration using 3 different samples, whilst the secondary part focuses on the best way to prevent alteration using only the ICM sample. The OPA experiment design in this study is shown in Figure 3.1.
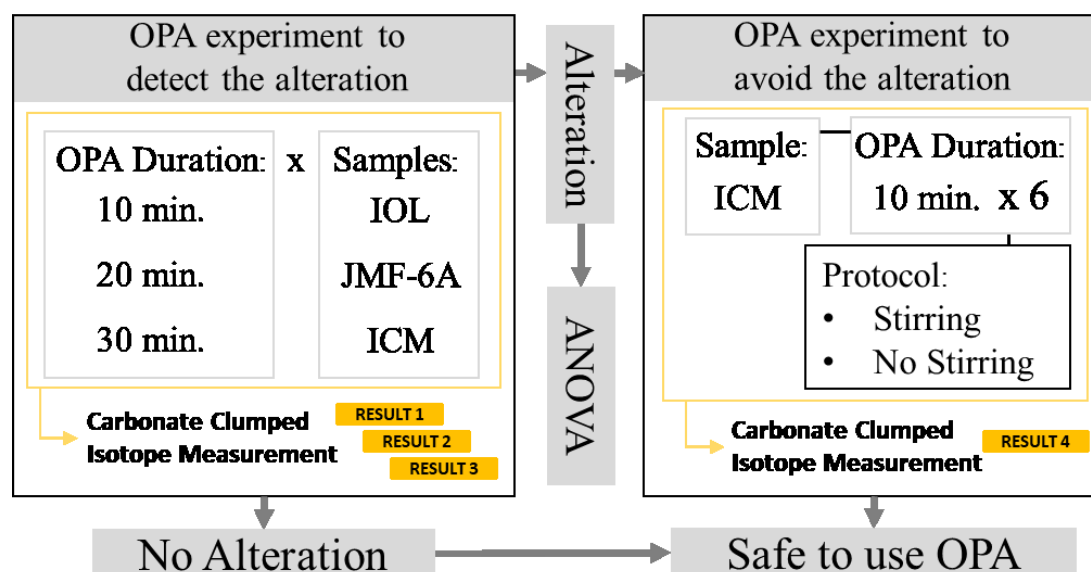
Figure 3.1. Research Design. There are three treatment duration to be applied to three types of samples with an additional experiment related to the stirring effect. The label "results 1,2 and 3" refer to clumped isotope measurements of the untreated, 10-minute, 20-minute and 30-minute OPA treatments respectively, for the three samples. Result 4 refers to the appended experiment where the petri dish was taken out of the plasma chamber to stir the powders with less than 3 minutes breaks between 10 minute plasma exposures.

3.2.3 Measurement and data analysis

Clumped isotopes, $\delta^{18}O$ and $\delta^{13}C$ measurements were carried out in the Qatar Stable Isotope Laboratory at Imperial College London. Each replicate measurement comprises eight acquisitions with seven cycles each of 26s integration time (John and Bowen, 2016). The measurement is repeated seven times per replicate in two different mass spectrometers (both MAT 253's) with a total analysis time of 2h per replicate on each mass spectrometer, "Pinta" equipped with an automatic prototype IBEX line, and "Santa Maria" used with a manual line to prepare samples. In this research, a minimum of nine replicates per sample were measured for both IOL and the JMF-6A sample, and six replicates per sample for ICM, which yields 127 measurements totalling 254 hours of analysis time. In order to increase throughput, 10% of measurements were made by manual purification of CO_2 following published procedures (Dale et al., 2014) and analysed on another Thermo MAT 253 mass spectrometer. The manual line is similar in design to the IBEX but has no carrier gas, relying instead on cryogenic vacuum transfer. The analytical method (calculations of raw Δ_{47}, $\delta^{18}O$ and $\delta^{13}C$) of both systems (manual and IBEX) was similar (see Chapter 2).

Calculations and corrections of raw Δ_{47}, $\delta^{18}O$ and $\delta^{13}C$ were performed using the free software Easotope (John and Bowen, 2016). For the 10% of samples prepared in the manual line, the first correction was to perform non-linearity correction on raw Δ_{47} using a series of heated gas with different bulk isotopic compositions and addition to the carbonate standards (Huntington et al., 2009). For samples run on the IBEX, all the standards were carbonates and a pressure baseline correction was used following the methods developed at the ETH Zurich (Bernasconi et al., 2013). Next, the Δ_{47} results were projected in the absolute reference frame or Carbon Dioxide Equilibrated Scale (CDES) (Dennis et al., 2011) based on routinely measured ETH1, ETH2, ETH3, ETH4 and Carrara Marble (ICM) carbonate standards (Muller et al., 2017; Davies and John, 2019). The standards to samples ratio used in this study was one standard per three samples. The last correction to the raw Δ_{47} was to add an acid correction factor of 0.088‰ to obtain a final $\Delta_{47(CDES)}$ value (Petersen et al., 2019). The bulk isotopic value of $\delta^{18}O$ was corrected for acid digestion at 90°C by multiplying the value by 1.0081

using the published fractionation factor (Kim et al., 2007). Mass 48 and mass 49 signal spikes were used as an indicators of the presence of hydrocarbons, chlorocarbons (Eiler and Schauble, 2004; Huntington et al., 2009) and sulphur bearing contaminants (Guo and Eiler, 2007; Huntington et al., 2009). Contamination was monitored by observing the values on mass 48 and 49 from each measurement, using a Δ_{48} offset value < 1.5‰ and/or a 49 parameter values < 0.3 as a threshold to exclude individual replicates from the analysis (Davies and John, 2017). To ensure that no bias in Δ_{47} offset was caused by using different purification lines and mass spectrometers, the results are compared both with and without the 10% data acquired with the manual purification line.

3.2.4 Statistical methods

The clumped isotope Δ_{47}, $\delta^{18}O$ and $\delta^{13}C$ values of all samples (Carrara marble, IOL and JMF-6A) are normally distributed (Davies and John, 2019), allowing for the application of parametric statistical tests on the sample data. Statistical analysis of One-way ANOVA (Analysis of Variance) was carried out using the SPSS 25 software (IBM). This statistical method was only performed on the IOL and JMF-6A samples. The null hypothesis was defined as plasma-treated samples representing the same population as the initial untreated sample. The alternative was that the mean results from the 10, 20- and 30-minutes OPA treatment are distinguishable as a unique population.

The Power analysis (Cohen, 1977) was implemented following the ANOVA test to quantify the likelihood that the null hypothesis could be rejected. For this analysis, the alpha level used was 0.05, while the effect size (partial eta-squared) was obtained from ANOVA results (Cohen, 1977).

If ANOVA indicated no statistically significant difference amongst the population but that the mean value of results indicated a systematic offset for a given population, then the LSD (Least Significant Difference) T-test (Fisher, 1936) was applied to focus on relative differences between the four populations (initial, 10, 20 and 30 minutes OPA). These multiple comparison tests (LSD) provide useful information even if the overall ANOVA results are not statistically significant. Although multiple comparison tests are commonly only applied after the null hypothesis of homogeneity is rejected, this practice is regarded as 'unfortunate common practice' by some statisticians (Hsu, 1996).

3.3 Results

The isotopic composition (Δ_{47}, $\delta^{18}O$ and $\delta^{13}C$) of all three samples treated with 10, 20, 30 and 60 minutes of oxygen plasma ashing are shown in Table 3.1. Previous work (Petersen et al., 2016; Davies and John, 2017) has shown that, due to the presence of the Porapak-Q trap used in the purification line,

the standard deviation of $\delta^{18}O$ of ICM was high (0.6‰ (Petersen et al., 2016) and 0.2‰ (Davies and John, 2017)) at a trap temperature of -35°C. Given previous work on this topic, impacts on the bulk isotopic trends are not the focus of this study due to the high standard deviation. Instead, this study focused on the Δ_{47} result.

3.3.1 Δ_{47} alteration

The results are presented as a boxplot with 95% confidence level with the mean value shown by a red line (Figure 3.2) and one standard error (SE) representing uncertainty. In this section, the term 'value' is understood to mean the 'mean value' of the total number of replicates measurements for each standards or samples. The Δ_{47} value of IOL deviates by -0.003 ‰ from the control population after a 10-minutes plasma treatment and -0.002 ‰ after a 20-minute plasma treatment. For sample JMF-6A, the Δ_{47} deviated by +0.004‰ after a 10-minutes and -0.005‰ after a 20-minute plasma treatment. All of these results are within the analytical error (± 1 SE) of 0.005‰ of the initial IOL value and 0.008‰ of the initial JMF-6A value.

Table 3.1. Carbonate clumped isotope parameter (Δ_{47}) and bulk isotope composition ($\delta^{18}O$ and $\delta^{13}C$ values) of IOL, JMF-6A and ICM before (initial values) and after OPA pre-treatment

Sample ID	OPA treatment duration (min)	n	$\delta^{13}C$ (‰, VPDB)	$\delta^{13}C$ SE (‰)	$\delta^{18}O$ (‰, VPDB)	$\delta^{18}O$ SE (‰)	Δ_{47} (‰, CDES)	Δ_{47} SE (‰)	Δ_{47} offset[a] (‰)
Oamaru limestone, New Zealand									
Initial value	0	11	0.289	0.011	0.355	0.023	0.732	0.005	0
IOL10	10	10	0.281	0.020	0.386	0.024	0.729	0.007	−0.003
IOL20	20	10	0.303	0.010	0.348	0.018	0.729	0.006	−0.002
IOL30	30	10	0.327	0.012	0.410	0.037	0.746	0.007	0.014
Jabal Madar calcite vein, Oman									
Initial value	0	10	−7.895	0.024	−14.732	0.028	0.629	0.008	0
JMF10	10	9	−7.827	0.047	−14.733	0.096	0.633	0.006	0.004
JMF20	20	9	−7.910	0.022	−14.763	0.028	0.624	0.009	−0.005
JMF30	30	9	−7.812	0.041	−14.664	0.049	0.653	0.008	0.024
Carrara marble standard									
Initial value	0	21	2.060	0.006	−1.894	0.009	0.411	0.003	0
ICM10X3	10x3[b]	8	2.070	0.007	−1.898	0.021	0.401	0.005	−0.010
ICM30	30	7	2.059	0.015	−1.906	0.045	0.422	0.006	0.011
ICM10X6NS	10x6[c]	7	2.056	0.004	−1.879	0.044	0.413	0.003	0.002
ICM10X6S	10x6[d]	6	2.035	0.019	−1.947	0.047	0.407	0.004	−0.004

No systematic change in the Δ_{48} offset and 49 parameters was found.
CDES, carbon dioxide equilibrated scale; ICM, internal Carrara marble; IOL, internal Oamaru limestone; JMF-6A, Jabal Madar; OPA, oxygen plasma ashing.
[a] The mean value of the plasma-treated sample minus the untreated mean value.
[b] The total duration of OPA pre-treatment was 30 min; the treatment was ceased every 10 min to stir the sample powder.
[c] The total duration was 60 min; the treatment was ceased every 10 min with no stirring procedure introduced.
[d] The total duration was 60 min; the treatment was ceased and stirred every 10 min.

The 30 minute OPA treatment of IOL resulted in a +0.014 ‰ deviation in the Δ_{47} value. This positive deviation of Δ_{47} occurred in eight out of ten measurements and 50% of the measurements yielded a positive alteration within ~ ± 3 SE of the initial IOL value. The same plasma duration for JMF-6A samples resulted in a +0.024‰ offset compared to the initial value. This positive offset occurred in eight out of nine measurements and 55% of the total measurements show a positive alteration within ± 3 SE of the initial JMF-6A value. For the ICM samples, the 30 minute plasma treatment resulted in +0.011 ‰ deviation in the Δ_{47} value, within ± 3 SE of initial values. The results were compared to including and excluding the 10% of manual line data, and there was no significant difference in this comparison (less than 1 SE change in average value). The systematic offset in experiments using 30 minutes of plasma treatment persisted.

One-way ANOVA tests showed that the plasma treatments on IOL and JMF-6A had no significant impact (α=0.05) on the Δ_{47} parameter with an $F(3,37) = 1.708$, p=0.182 for IOL and $F(3,33) = 2.639$, p=0.066 for JMF-6A (Table 3.2). Using the calculated effect size of 0.125 and 0.181, the power analysis of Cohen (1977) on IOL and JMF-6A yielded values of 0.0853 and 0.119 based on a 0.05 α value. These results are considered as low values (<0.2;Cohen, 1977) implying that it is difficult to prove the statistical difference between the groups, even if a difference might exist. The size of the dataset (n) plays an important role in this power analysis, as the power value has a positive correlation with to the dataset size (Mahapoonyanont et al., 2010). The ability to reject the null hypothesis would be improved for larger datasets (n).
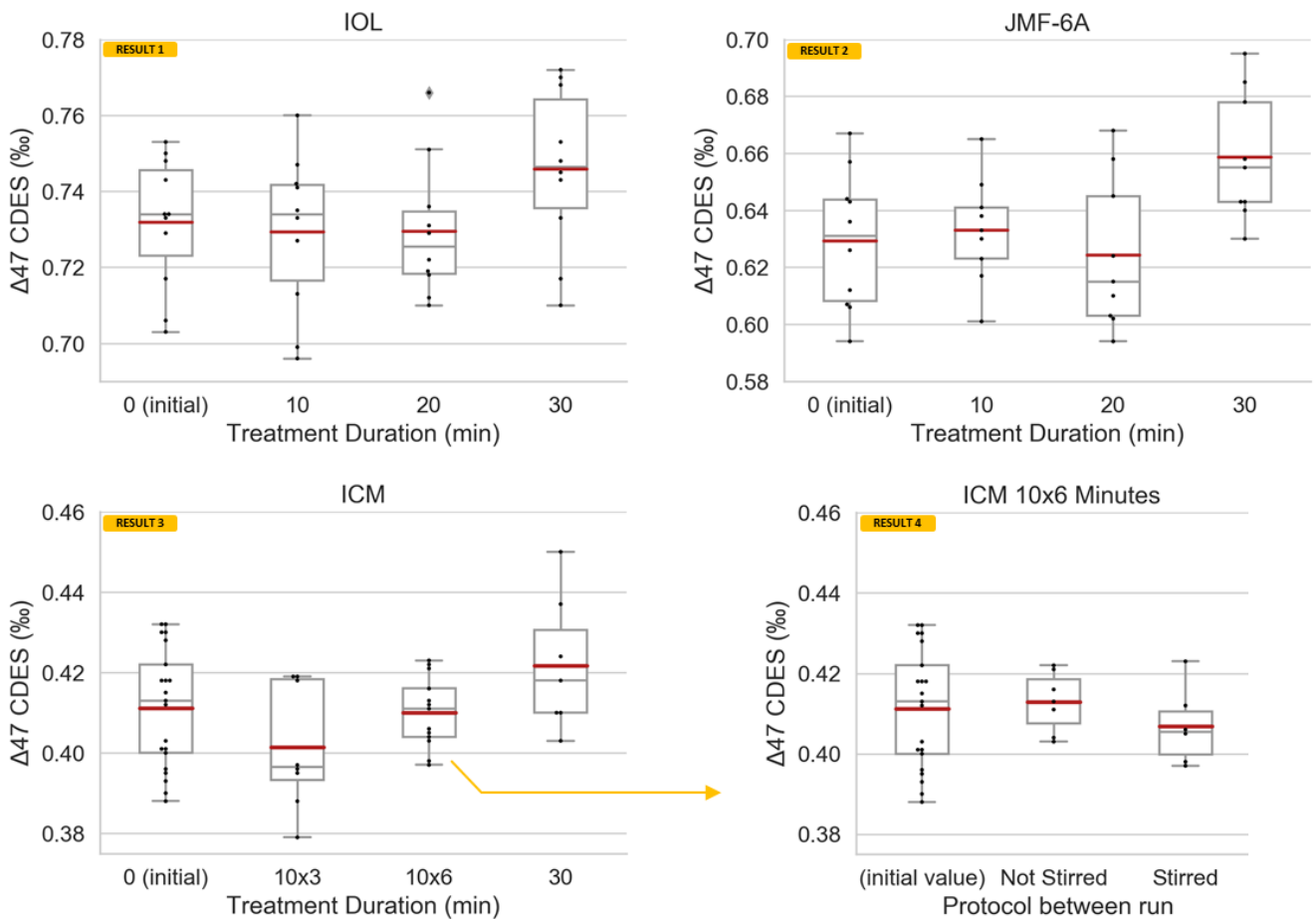
Figure 3.2. Box plot result of oxygen plasma ashing treatment on internal Oamaru limestone (IOL), Jabal Madar (JMF-6A), internal Carrara marble (ICM) and ICM 60 min (Results 1, 2, 3 and 4). Mean values shown by red lines.

Multiple comparison LSD tests on IOL and JMF-6A (Table 3.2) provides a numerical analysis that quantifies what has been observe in the boxplot, even if the overall ANOVA results are not statistically significant. The individual p-value of the comparison of initial vs 30 min OPA for IOL was closer to 0.05 value compared to others (e.g., initial vs 10 min and initial vs 20 min). For the JMF-6A, the p-value of the initial vs 30 min OPA was below 0.05 value compared to others (e.g., initial vs 10 min and initial vs 20 min). The LSD results suggest that the populations of initial vs 30 min OPA are likely to be different from the others. Note that p-value less or equal to 0.05 value are considered to be a significant difference.

Table 3.2. ANOVA and post hoc LSD analysis of IOL and JMF-6A samples.

ANOVA	Sum of squares	DF	F	P-value	Post hoc LSD		Mean difference	P-value	95% confidence level Lower bound	95% confidence level Upper bound
IOL/Oamaru limestone										
Between group	0.002	3	1.708	0.182	Initial vs.	10 min	0.003	0.766	−0.015	0.020
Within group	0.014	37				20 min	0.002	0.775	−0.015	0.019
Total	0.016	40				30 min	−0.014	0.103	−0.031	0.003
JMF-6A/Jabal Madar calcite										
Between group	0.004	3	2.639	0.066	Initial vs.	10 min	−0.004	0.725	−0.026	0.018
Within group	0.018	33				20 min	0.005	0.653	−0.017	0.027
Total	0.022	36				30 min	−0.024	0.033	−0.046	−0.002

The null hypothesis was not rejected for all groups of treatment, but there is a noticeable difference between the mean value of the 30 min treatment and the initial value. The LSD post hoc reveals a distinguishable difference in the *P*-value on the 30 min plasma treatment.
ANOVA, analysis of variance; DF, degrees of freedom; IOL, internal Oamaru limestone; JMF-6A, Jabal Madar; LSD, least significant difference.

3.3.2 Testing variations of the OPA protocol on ICM

A variation of the OPA protocol (Table 1) was performed on ICM to observe the effect of the total exposure area to the plasma on the Δ_{47} value (Figure 3.2, Result 4). Three treatments of 10-minutes of OPA were performed sequentially on a sample, stirring the powder with a glass rod between the runs. This experiment resulted in a Δ_{47} offset of -0.010‰, i.e. within ± 3 SE of the untreated ICM sample. Furthermore, an experiment of 6 OPA treatments of 10 minutes each with no stirring yielded a Δ_{47} value within the analytical error (± 1 SE) of the untreated ICM sample, while the stirred samples yielded a Δ_{47} offset of -0.004‰, 1 ppm below the ± 1 SE of the untreated ICM sample.

3.4 Discussion

3.4.1 Contamination and effectiveness of the OPA

The principle of the OPA method is that excited oxygen (O_2^+, O, O_2, O^-) and electrons are created by exposing oxygen reagent at a low temperature to radiofrequencies in a vacuum chamber (Dai, 1996). When these particles enter into contact with the sample surface, they oxidize organic particles into CO_2 and water vapour (Belkind and Gershman, 2008).

Traditionally, two contamination indicators are used to screen data for clumped isotopes, the Δ48 offset and 49 parameters (John and Bowen, 2016). Replicate samples with values exceeding an acceptable threshold of 1.5‰ for the Δ_{48} offset and 0.2 for the 49 parameters (Davies and John, 2019) are rejected. A previous study of the Pinda reservoir dolomites in Angola (MacDonald et al., 2015), performed in Imperial College London, demonstrated that dolomite samples stained with hydrocarbon could still yield high-levels of contamination when cleaned through a Porapak trap. The unpublished raw data from this Pinda reservoir study (MacDonald et al., 2015) showed that low-temperature OPA treatment

solved the contamination issue (Δ_{48} offset: 6.8-20 ‰, 49 parameters: 0.389-0.525, data presented here in Table 3.3). Even in the 5 minute OPA treatment, both of these contamination indicators were reduced significantly to within acceptable values (Δ_{48} offset: 0.270-0.407‰, 49 parameters: 0.087-0.174, Table 3.3). Thanks to the low-temperature OPA treatment, the proportion of acquisitions showing an acceptable low level of contamination increased to 77.8% (MacDonald et al., 2015) (Figure 3.3).

Table 3.3. A result of carbonate clumped isotope parameter (Δ_{47} value) after OPA pre-treatment and the reduction of the contaminant level of the Δ_{48} offset and the 49 parameters in hydrocarbon-saturated carbonate samples from Angola

Sample ID	n	Δ_{47} (CDES) (‰)	Δ_{47} SE (‰)	Δ_{48} offset (‰) Mean	Max. value	49 parameter Mean	Max. value
Untreated sample							
Buff1	7	0.582	0.010	18.5	68.8	0.389	0.712
Caco1	7	0.566	0.026	6.8	29.6	0.525	1.996
Caco2 3637	4	0.592	0.028	20.0	62.2	0.468	0.847
Caco2 3705	3	0.543	0.016	11.7	28.2	0.465	0.855
Palang	10	0.564	0.011	19.4	162.7	0.422	0.766
5 min of OPA							
Buff1	4	0.552	0.022	0.407	0.781	0.127	0.388
Caco1	4	0.526	0.019	0.319	0.424	0.087	0.108
Caco2 3637	4	0.581	0.016	0.227	0.510	0.174	0.289
Caco2 3705	4	0.553	0.021	0.107	0.270	0.086	0.122
Palang	3	0.535	0.008	0.393	0.480	0.151	0.188

The data set is obtained from the unpublished data measured by MacDonald et al.(2015)
CDES, carbon dioxide equilibrated scale; OPA, oxygen plasma ashing.
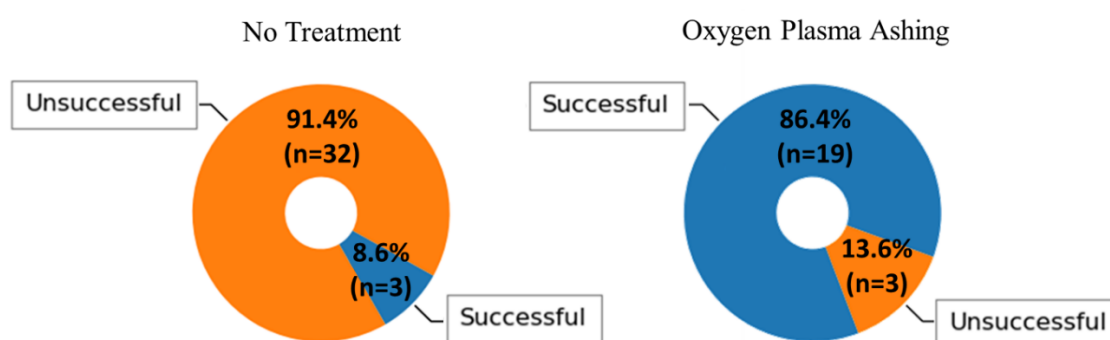
Figure 3.3. Oxygen plasma ashing pre-treatment rate of success on carbonate reservoir samples contaminated by hydrocarbon (bitumen) based on 57 carbonate clumped isotope measurement of MacDonald et al, 2015. The clumped isotope measurement rate of success based on acceptance of Δ_{48} offset and 49 parameter contaminant level.

3.4.2 Effect of the OPA treatment on Δ_{47}

This study results reveal that, for the radio frequency of this specific instruments, a 30 minute OPA treatment has the potential to cause an observable systematic positive offset in clumped isotopes (Δ_{47}). However, if the total duration of 30 minutes of OPA treatment is applied in discrete 10 minute treatment intervals followed by stirring, no significant increase in Δ_{47} value is observed. This suggests that, for an offset to exist, the same mineral surface needs to be exposed to the plasma for 30 minutes, as stirring between runs effectively exposes new crystal surfaces between each run.

Although not statistically significant in the ANOVA tests (Δ_{47} offset of 0.014 ‰ for IOL; 0.024‰ for JMF-6A and 0.011‰ for ICM), all of the 30 minute non-stop OPA treatments consistently yield a different population of results with a positive offset from the control population, numerically proven by the multiple comparison test LSD. It is interesting to note that the same treatment for ICM yields the smallest Δ_{47} alteration. Two possible hypotheses are suggested to explain this: either (hypothesis 1) the increase in Δ_{47} is proportional to the initial Δ_{47} value of the material as ICM has the lowest initial Δ_{47} value of the three samples, or (hypothesis 2) the effect of OPA treatment is proportional to differences in mineral reactivity given that only Carrara Marble (ICM) was impacted by metamorphic processes.

The easiest explanation for a change in Δ_{47} proportional to the initial value of the sample (hypothesis 1) is admixing of a newly formed calcite mineral during OPA treatment. One of the by-products of OPA treatment is water vapour inside the plasma chamber, which has the potential to lead to isotopic exchange between the calcite and water molecules via dissolution-precipitation processes. If this was the case, then the isotopic exchange most likely have occurred at the outer surface of the calcite and yielded a new composition for the neoformed calcite with Δ_{47} value in equilibrium with the plasma chamber temperature of 65-70 °C, i.e., 0.577 to 0.588‰ (Davies and John, 2019). This newly precipitated calcite phase would mix with the existing samples, and we might thus expect to see an increase in the final Δ_{47} value of ICM since the initial Δ_{47} value for this sample is lower than the chamber temperature, and a lowering of the Δ_{47} value for both IOL and JMF-6A which have initial Δ_{47} values higher than the chamber temperature. This predicted trend is incompatible with the results for IOL and JMF-6A and thus hypothesis 1 is rejected.

A difference of mineral reactivity (hypothesis 2) could, for instance, impact the parameters of solid-state reordering (Passey and Henkes, 2012). However, the low temperature recorded in the plasma chamber (<100°C) effectively precludes this process from happening. Other potential mineral reactivity mechanisms to explain how OPA treatment impacts clumped isotopes include, for instance, thermal dilatation or thermal-induced expansion of minerals. It is known that thermal expansion of calcite minerals may occur in the powdered samples during the plasma treatment: a heating/cooling

cycle of +20°C, -60°C, -20°C on Italian Marble resulted in thermal expansion leading to a reduction of the cohesion strength of the grains (Koch and Siegesmund, 2004). The volumetric thermal expansion of limestones is also 14.5% larger (Robertson, 1988) than for marbles for the temperature range of 20°C -100°C due to grain density and crystal orientation differences; as a consequence, the thermal expansion of IOL and JMF-6A would yield a larger mineral surface area to the plasma bombardment than the ICM sample. Previous experiments (Roberts et al., 2018) suggested that a larger surface area of calcite exposed to the plasma tends to increases the potential for atmospheric CO_2 isotopic exchange reactions due to disruption on the calcite lattice. Therefore, the smaller Δ_{47} offset between ICM and the two other samples for the 30 minute OPA treatment could be due to the different volumetric thermal expansion properties (Robertson, 1988), with marbles (ICM) being less susceptible to thermal expansion possibly due to a better crystal orientation after metamorphism. This smaller offset could also be related to population size, as the standard error of 30-minute OPA on ICM is greater than for the other samples. However, if the thermal expansion hypothesis can explain the difference in magnitude of impact of the OPA treatment in the three samples, it cannot explain why the Δ_{47} increases in the 30 minute treatment in the first place.

Careful observations of the petri dish following the 30 minutes of plasma treatment revealed the occurrence of highly adhesive white particles (potentially CaO, though this could not be tested due to its small quantity) on the side of the petri dish, suggesting that high energy reactive species in the plasma treatment were able to sputter a small amount of carbonate material over the entire petri dish surface. Such a high-energy bombardment may not only project particles out of the petri dish, but also break organic and inorganic carbon bonds at the surface of calcite. Since the Δ_{47} measurement depends on the relative abundance of the ^{13}C-^{18}O bond, and that the bond containing the heavy isotope is slightly stronger (Eiler, 2007), the increasing value of Δ_{47} after the 30 minute plasma experiment in this experiment is most likely due to the preferential breaking of the bonds between the lighter isotopes caused by the high energy reactive species in the plasma. This process would lead to a progressive increase in the proportion of ^{13}C-^{18}O bonds at the surface of the calcite grains, and thus an increase in Δ_{47} (Figure 3.4).
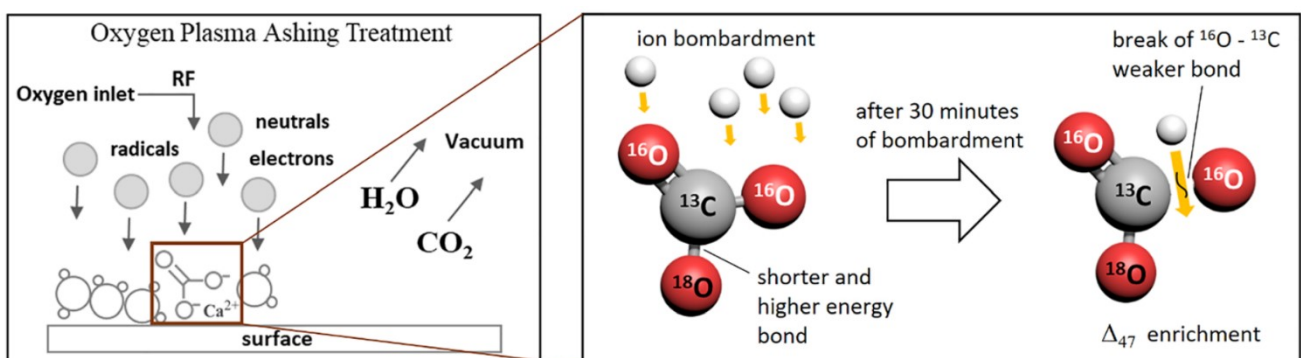
Figure 3.4. Hypothetical model for Δ_{47} enrichment by preferential breaking of the weaker bonds (e.g. ^{13}C-^{16}O) after 30 minutes of oxygen plasma ashing treatment.

Table 3.4. Temperature difference comparison of untreated samples and the 30 minutes treatment

Sample ID	Δ_{47} (‰, CDES)		Temperature, $T_{\Delta 47}$ (°C)		Temperature difference (°C)
	Untreated	After 30 min OPA	Untreated	After 30 min OPA	
IOL/Oamaru limestone, New Zealand	0.732	0.746	12.7	8.8	3.9
JMF-6A/Jabal Madar calcite vein, Oman	0.629	0.653	47.2	38.1	9.1
ICM/Carrara marble standard	0.411	0.422	199.9	186.7	13.3

CDES, carbon dioxide equilibrated scale; ICM, internal Carrara marble; IOL, internal Oamaru limestone; JMF-6A, Jabal Madar.

3.4.3   Implications for paleotemperature reconstructions

Since Δ_{47} has a quantitative relationship with temperature, the implications of the observed offset caused by OPA treatment can be quantified using the following temperature calibration (Davies and John, 2019):

$$\Delta_{47} = 0.03998 \text{ x } \frac{10^6}{T^2} + 0.2423$$

The difference between the initial temperature of the sample and the temperature after 30-minutes of continuous oxygen plasma treatment induces a bias towards lower temperatures of 3.9 °C for IOL, 9.1 °C for JMF-6A and 13.3 °C for ICM (Table 3.4). Whether or not this bias is significant will depend on the particular application. In paleoclimate studies, the order of magnitude of change in Δ_{47} that reported here for 30 minutes corresponds to a large enough temperature difference to potentially mask any paleoclimatic signal being investigated. However, this study emphasizes that the shorter OPA treatments of 10 minutes do not significantly alter the Δ_{47} and can thus be considered safe for clumped isotope applications.

3.5   Conclusions

An effective treatment to remove organic material prior to carbonate clumped isotope analysis must maintain the original isotopic composition of the mineral while removing contaminants. Based on this experiment, 30 minutes or more of oxygen plasma ashing on calcite powders has the potential to alter the initial isotopic composition beyond analytical error, thus biasing paleotemperature studies. The small data populations used for the test cannot prove the statistical significance (α of 0.05) of the OPA alteration.

This study suggests that the positive offset occurs because the bonds between the lighter isotopes are preferentially broken by OPA treatment, leading to an increase in the 'clumping' of the sample. Because the magnitude of the observed mean value can range from 4°C to 13 °C in the 30-minute treatment, this study recommends that any laboratory performing OPA should shorten the runs to 10 to 20 minutes, as plasma treatment of this duration on instrument used in this study shows no alteration of the initial value of Δ_{47}. In addition, it is possible to safely remove additional organic matter by doing successive runs of 10 minutes, followed by a break and stirring of the sample, as this procedure, with a total OPA time of 30 minutes (and 60 minutes on Carrara Marble) shows no offset in Δ_{47}. This results thus validate the use of OPA for clumped isotope applications and will allow future research using clumped isotopes in challenging samples, such as oil-stained carbonates, bituminous shales, or very high organic carbon content host rocks. Future research should consider the potential OPA effects on different mineral (i.e. aragonite) which may respond differently under plasma bombardment.

CHAPTER 4

RECRYSTALLIZATION TEMPERATURE OF SHALLOWLY BURIED CARBONATES AND POTENTIAL CLUMPED ISOTOPE APPLICATION FOR PETROLEUM MIGRATION STUDY

4.1 Introduction

Carbonate rocks provide a large proportion of the world reservoirs for hydrocarbons and water, and are thus important for energy resources and access to clean water. But to contain fluids, rocks need porosity, and carbonate porosity evolution is complex because of the high chemical reactivity of the carbonate minerals (Choquette and Pray, 1970; Moore, 1989a). All of the reactions during burial diagenesis are aqueous dissolution-(re)precipitation reactions, and it has long been suggested that displacement of water by petroleum could inhibit or stop these reactions (Feazel and Schatzinger, 1985; Worden et al., 1999; Worden and Heasley, 2000). This has been conclusively demonstrated to occur only in microporous limestone reservoirs, based on trends of increasing porosity toward the crests of domal structures within strata having little lateral variation in depositional texture (D'Heur, 1984; Oswald et al., 1995; Neilson et al., 1996; Brasher and Vagle, 1996; Melville et al., 2004; Ehrenberg et al., 2016; Van Simaeys et al., 2017; Ehrenberg et al., 2020). Reports of inferred porosity preservation by petroleum in other types of carbonate hosts are unconvincing, however, because variations in depositional texture were not considered and interpretations of paleo-oil/water contact positions are open to doubt. Sandstone reservoirs also show no evidence of any petroleum inhibition effect (i.e. quartz cement retardation) (Giles et al., 1992; Bjorkum and Nadeau, 1998; Molenaar et al., 2008), despite clear evidence that porosity in the oil zone of certain Upper Jurassic sandstones has been preserved by grain-coating microquartz (Aase et al., 1996). Some studies have concluded that sandstone diagenesis can be slowed down by petroleum emplacement (Worden et al., 1998; Marchand et al., 2001; Worden et al., 2018). However, there has, to date, been little examination of the detailed timing and geochemistry of process by which petroleum inhibits diagenesis in the microporous limestone reservoirs, and this is a main focus of the present study.

Carbonate burial diagenesis is controlled by the mineral-surface area available for reaction, the saturation state of diagenetic fluids, the thermodynamic stability of the carbonate minerals being dissolved or precipitated and the rates of dissolution and precipitation (Flügel, 2010). The fluids are commonly chemically complex brines resulting from long-term water-rock interaction under elevated temperatures and pressures (Stoessell and Moore, 1983; Moore, 1989b, 2001). At the same time, elevated burial temperatures increase the rates of chemical reactions and ionic diffusion (Moore, 2001). Comparison between the temperatures recorded in recrystallized carbonates and established burial

histories and timing of petroleum accumulation provides a way of testing the hypothesis that water displacement inhibits or stops diagenesis.

An issue is that established proxies to estimate recrystallization temperatures (notably fluid inclusions) are difficult or impossible to apply in carbonates with very small crystal sizes (i.e. micrite) (Mathieu et al., 2013; Mraz et al., 2019). This study used carbonate clumped isotope paleo-thermometry to circumvent this problem. Previous studies (Shenton et al., 2015; John, 2018; Veillard et al., 2019) have shown that the clumped isotope technique is sensitive to complete and partial recrystallization and thus yields information on diagenetic processes. The previous body of work also reported that each carbonate fabric has a different susceptibility to dissolution-reprecipitation (Shenton et al., 2015).

Here, the clumped isotope technique is performed on the fine-grained matrix, skeletal grains and cements of subsurface carbonates from an oil-bearing reservoir in the Arabian Plate. This is an ideal study location because of previous work on the diagenetic and thermal history using fluid inclusions and petrography (Burruss et al., 1985; Alsharhan, 1989; Oswald et al., 1995). The same studies also suggested that this interval experienced multiple recrystallization processes, implying the possibility of overprinted fluid inclusions in the carbonate cements. The study objectives of this chapter are **[a]** to further understand the response of different limestone fabrics to thermal resetting with respect to clumped isotopes, and **[b]** to investigate whether or not carbonate diagenesis (cementation and recrystallization) continued after hydrocarbon emplacement, as has been debated (Neilson et al., 1996; Neilson et al., 1998; Barclay et al., 1999; Cox et al., 2010; Kolchugin et al., 2016).

Figure 4.1. Carbonate formations used for this study with stratigraphic units modified from Van Buchem et al. (2010). Samples were obtained from carbonate reservoir rock of the Lower Cretaceous

Upper Thamama Group, Aptian-Barremian (Barremian II sequence) from two giant oilfields on the Arabian Plate, located onshore and offshore.

4.2 Geological setting of the carbonate interval

The sedimentary system in the study area, UAE (see Ehrenberg et al., 2020), was initially filled by the prograding Lekhwair- Habshan-Salil (LHS) system during the Barremian (Landmesser and Saydam, 1996; van Buchem et al., 2002b), and was followed by aggradation of the Kharaib, Shu'aiba, Nahr Umr and Natih Formations (van Buchem et al., 2002b). The Barremian-Aptian interval comprises the Shuaiba, Kharaib, and Lekhwair Formations, which developed on a broad carbonate ramp (van Buchem et al., 2002b; van Buchem et al., 2010; Vahrenkamp et al., 2014). The sample used for this study is collected from sequence II of the Barremian strata (Figure 4.1), which consists of three early facies associations: 1) Orbitolonid/miliolid wackestone to packstone; 2) mixed-fauna mudstone with wackestone; and 3) Rudist/miliolid wackestone, packstone, grainstone and framestone (van Buchem et al., 2002b).

4.3 Material and methods

4.3.1 Samples

Samples for this study come from cores collected in seven wells from an onshore giant oilfield and one well from an offshore giant oilfield, both located in the UAE (see Ehrenberg et al., 2020). Note that the publication of the name of wells and fields in the study area is very restrictive, including the prohibition of giving full details about samples. The collaborator of this research only allows the release of essential information. Here, the name Rainy (offshore giant oilfield) and Ibrahim (onshore giant oilfield) are used to disguise the original well names.

Small amounts of different textural components, including skeletal grains, matrix, and cements, were extracted from cut surfaces using a dental drill at the lowest possible speed (1000-2000 rpm). To obtain homogeneous powder size, the samples were subsequently gently crushed with an agate mortar and pestle and then sieved through a 125 µm sieve. Because of the presence of oil residue, the offshore field core samples were treated with low-temperature plasma ashing (Henniker Plasma HPT-100) for 2x10 minutes duration (Adlan et al., 2020) under oxygen at a flow rate of 46 mL/min and a power of 100 W, with vacuum condition of 0.2 mbar. This plasma treatment does not affect the original isotopic composition of sample (Adlan et al., 2020).

4.3.2   Petrography and mineralogy

Petrographic observations were made using a transmitted light Zeiss Axioskop 40, followed by cathodoluminescence (CL) microscopy on a Nikon Eclipse 50i microscope equipped with a CITL cathodoluminescence MK5-2 stage. The operating conditions for the CL stage were a current of 315 µA, an accelerating voltage of 15 kV, and vacuum operating at 0.003 mBar. Fourier Transform Infrared Spectroscopy (FT-IR-Spectrometer Nicolet 5700) was used to ensure the samples were homogeneous and to qualitatively estimate mineralogy (calcite) following Henry et al. (2017).

4.3.3   Stable isotope measurement and data analysis

Clumped isotopes, $\delta^{18}O$ and $\delta^{13}C$ measurements were carried out in the Qatar Stable Isotope Laboratory at Imperial College London using fully automated IBEX (Imperial Batch EXtraction) system. The details of stable isotope measurement method is described in Chapter 2. The uncertainty of the isotopic measurements in this study is reported by 1 standard error.

4.4   Results

4.4.1   Petrography

Textures of the analyzed samples are described in Table 4.1. Major allochems include rudist fragments, peloids, miliolids and molluscs fragments. Ehrenberg et al. (2018) reported that the rudist types in this interval are mainly *Glossomyophorus costatus* (Masse et al., 2015) and less abundant *Agriopleura cf. libanica* (Astre) (Masse and Fenerci-Masse, 2015).

The term 'skeletal grain' refers to >2 mm skeletal fragments that could be sampled using a dental drill. The term 'matrix' refers to the grain-supported packstone matrix, including both allochems and recrystallized mud (Figures 4.2, 4.3 and 4.4). The term "micritization" is used to refer to both the breakdown of original skeletal fragments to form micrite on the seafloor (Reid et al., 1992; Reid and Macintyre, 1998) and the microborings infilled by micrite (Bathurst, 1966). The matrix of thewackestone and packstone samples consists of micritized skeletal fragments/foraminifers ("Mic_x" and "F", Figure 4.2.B_1). This micritization is typically associated with seafloor processes (Reid et al., 1992; Reid and Macintyre, 1998). Another micritization signature identified in the thin sections was boring infilling ("Bor") within rudist shell fragments ("Rud", Figure 4.3.E_1 and Figure 4.4.H_1). The precipitation of micrite in open borings is classically interpreted as generated by the organism (Bathurst, 1966). There is also micrite ("Mic_y") found dispersed along (or within)equant/blocky calcite cement (Figure 4.2.A_1 and C_1).

Table 4.1. Sample descriptions.

Well Identifier	Depth (m)	Petrographic Description	Component Analyzed	Sample ID
Onshore Giant Field				
Ibrahim-911	2719	Packstone to wackestone, rudist, orbitolinid and foramninifers chamber filled by cement	Matrix (Mic$_x$) Skeletal (Rud)	K89220_m K89220_sk
Ibrahim-9139	2743	Packstone to wackestone, blocky calcite cement	Matrix (Mic$_x$)	L90004_m
	2745	Rudist (Glossomyophorus costatus) skeletal floatstones with micritized packstone matrix, blocky calcite cement with micrite inclusion	Matrix (Mic$_x$) Skeletal (Rud) Cement (Cm)	L90088_m L90088_sk L90088_cem
Ibrahim-919	2823	Packstone to wackestone, blocky calcite cement	Matrix (Mic$_x$)	M92641_m
	2829	Floatstones with packstone to wackestone matrix	Skeletal (Rud)	M92836_sk
Ibrahim-922[a]	2963	Packstone to wackestone with blocky calcite cement, peloids and miliolids fragments	Matrix (Mic$_x$) Skeletal (Rud)	N97205_m N97205_sk
Ibrahim-926[b]	2918	Grainstone to packstone with blocky calcite cement, miliolids and molluscs fragments	Matrix (Mic$_x$) Skeletal (Rud)	W957510_m W957510_sk
Ibrahim-973	2760	Packstone, forams chamber filled by cement	Matrix (Mic$_x$)	X90571_m
	2764	Rudist skeletal floatstones with packstone to wackestone matrix, equant/blocky calcite cement along with minor dolomite crystal	Matrix (Mic$_x$) Matrix (Mic$_x$) Cement (Cm)	X90704_m2 X90704_m1 X90704_cem
Ibrahim-980	2746	Rudist skeletal floatstones with packstone to wackestone matrix, micritized rudist, blocky calcite cement	Matrix (Mic$_x$) Matrix (Mic$_x$) Mic. Skeletal (Rud$_m$)	Y90101_m2 Y90101_m1 Y90101_sk(mic)
Offshore Giant Field				
Rainy-9316	2886	Floatstones with micritized packstone matrix, equant/blocky calcite and minor dolomite cement	Matrix (Mic$_x$) Skeletal (Rud)	Z94708_m Z94708_sk

[a] Sample obtained 63m below free-water level

[b] Sample obtained 18m below free-water level

Based on plane-polarized and crossed-polarized light photomicrograph, there are texturally preserved (Figure 4.3.E) and partially altered rudist shells (Figure 4.3.F) found in the samples. The preserved rudists show a better preservation of the original shell with a lateral aggrading prism of calcitic shell layers and homogeneous crystal size (Figure 4.3.E$_2$), similar to Aptian rudist shells found in Crismina Fort, Portugal (Skelton, 2018). The partially preserved rudists reveal some differences in the calcite crystal mosaic between the smaller crystals (square mark with label) and bigger crystal (triangle mark with label) (Figure 4.3.F$_2$). This difference reveals that some of rudists are partially altered, similar to the partially-altered (micritized) rudist shells found in Mt Varchera, Italy (Frijia et al., 2015).
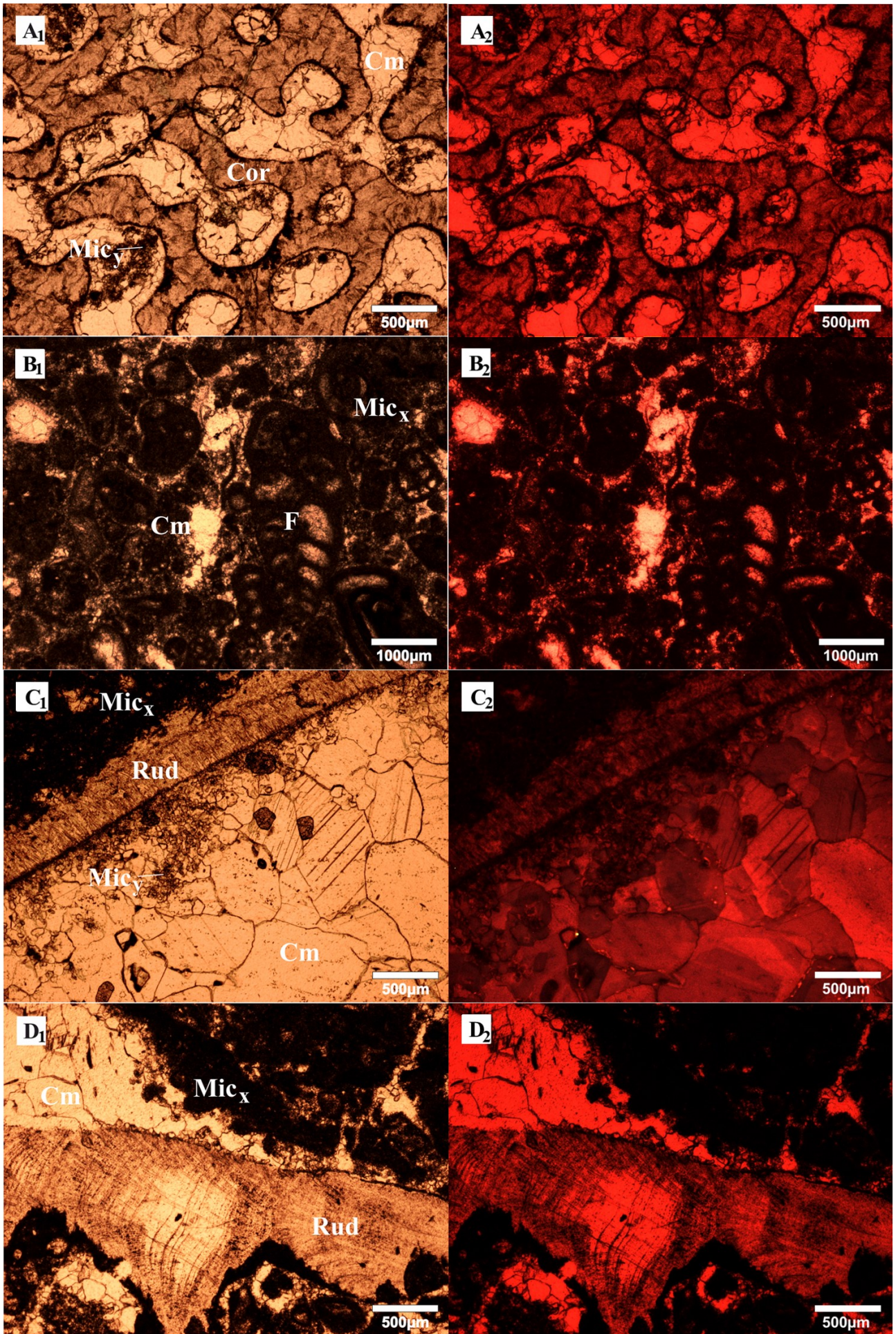
Figure 4.2. Photomicrographs with plane light (left) and cathodoluminescence (right). A. Sample M92641 of Ibrahim-919 well, coral (Cor) with equant calcite cement (Cm) formed along the micrite (Mic$_y$); B. Sample L90088 of Ibrahim-9139 well, rudist skeletal floatstone with micritize packstone matrix with fragments/foraminifers (Mic$_x$ and F); C. Sample X90704 of Ibrahim-973 well, rudist skeletal (Rud) floatstone with equant/blocky calcite cement (Cm); D. Sample L90088 of Ibrahim-9139 well, rudist skeletal floatstone with micritize packstone matrix (Mic$_x$). The "Mic$_y$" micrite found dispersed along (or within) this equant/blocky calcite cement has a brighter luminescence compare to "Mic$_x$".
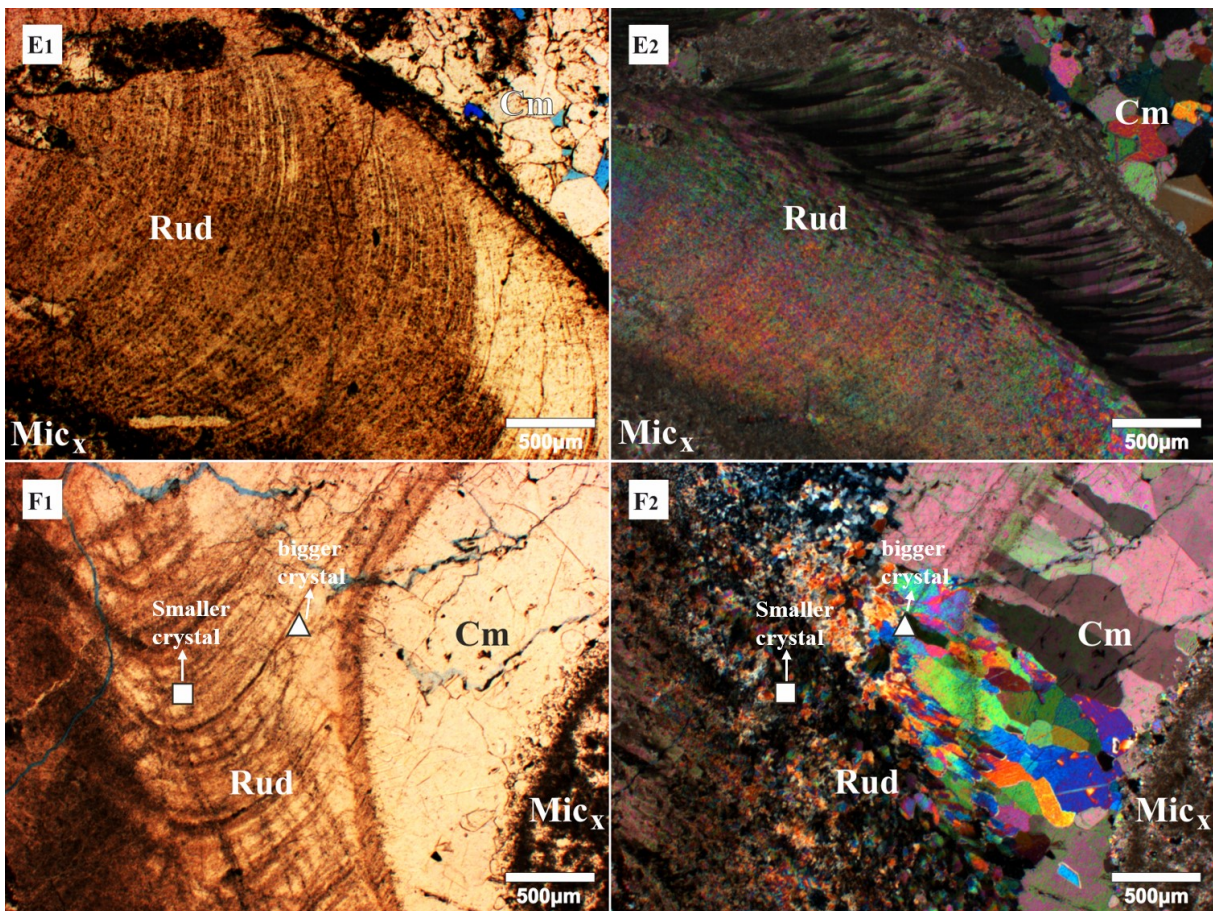
Figure 4.3. Photomicrographs of rudist shells with plane light (left) and crossed-polarized light (right). E$_1$, E$_2$. Sample K89220 of Ibrahim-911 well, with evidence of a better preserved lateral aggrading prism of the shell with homogeneous calcite crystal size; F$_1$, F$_2$. Sample N97205 of Ibrahim-922 well, with evidence of textural difference within the rudist shell of the smaller crystal size mosaic (square mark with label) compare to the bigger crystal mosaic (triangle mark with label) showing partially altered rudist shell.

Based on photomicrographs of plane-polarized and crossed-polarized light, there are two sets of rudist: texturally preserved (Figure 4.3.E) and partially altered rudist shells (Figure 4.3.F). The preserved

rudists are indicated by a better preservation of the original shell with a lateral aggrading prism of calcitic shell layer and homogenous crystal size (Figure 4.3.E_2) that have a similar presentation to the Aptian rudist shell found in Crismina Fort, Portugal (Skelton, 2018). Meanwhile, the partially - preserved rudists exhibit a difference in the crystal mosaic that can be observed by comparing the crystal size (Figure 4.3.F_2). Similar partially-altered (micritized) rudist shells were found in Mt. Varchera, Italy (Frijia et al., 2015). In this study, it is also found that a fine-sized recrystallized-rudist segment ("Rud_m") has a similar texture to the enclosed matrix distinguished from the original rudists ("Rud") (Fig. 4.G1 to 4.H2). Skeletal chamber and interparticle porosity are mainly filled by an equant-blocky calcite cement ("Cm", Figure 4.2.C and D). Along with this equant calcite cement, occurs a rhombic-crystal dolomite cement (Cm_d), with the brightest cathodoluminescence and void-filling characteristics found in this study (Figure 4.4.H_2). Cathodoluminescence petrography reveals that the cements have a brighter luminescence compared to both skeletal fabric (rudists) and the packstone-wackestone matrix (Figure 4.4.H_1 and H_2). In summary, petrographic observations defined six recognizable diagenetic fabrics in the study area (Figure 4.5): micritized-matrix, micritized bright luminescent rudist, dark luminescent rudist, bright-luminescent micrite, equant/blocky calcite cement, and dolomite cement. Note that the micrite (Mic_y) and the dolomite cement (Cm_d) were excluded for isotopic analysis because of sampling-size limitations (Table 4.1), while the rudists sample ("Rud_m" and "Rud") were obtainable due to visual difference (lustre and color) within the shell.
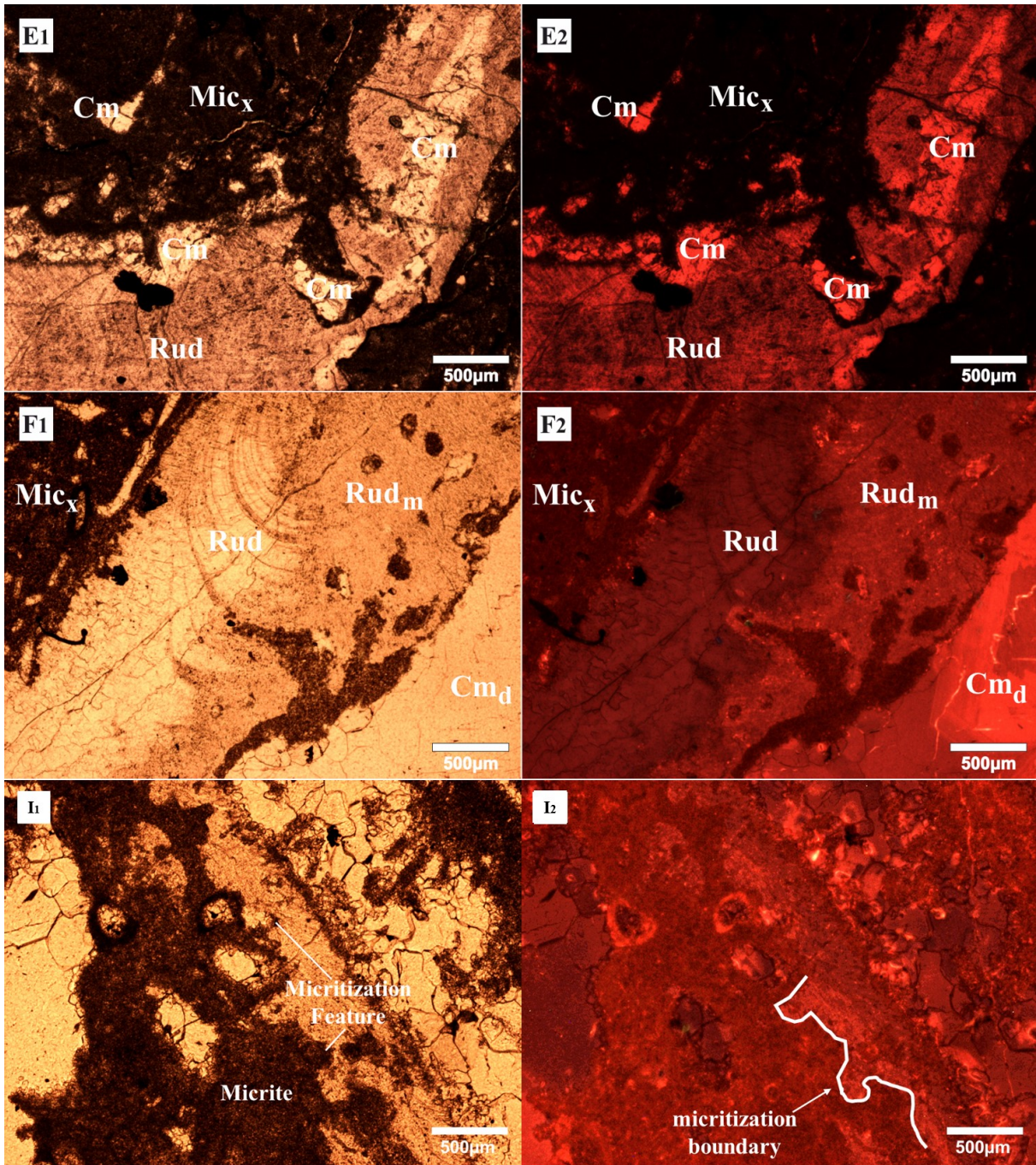
Figure 4.4. Photomicrographs with plane light (left) and cathodoluminescence (right). G_1, G_2. Sample M92641 of Ibrahim-919 well from onshore field, with evidence of equant/blocky calcite cements replacing the mud matrix and plugging most of intraparticle porosity (Cm); H_1, H_2, I_1, I_2. Sample Z94708 of Rainy-9316 well from offshore field, with evidence that (1) calcite cement formed within interparticle porosity, (2) rudists are partially recrystallized (Rud_m) and (3) the occurrences of dolomite cement (Cm_d). The skeletal fabric shows a dissolution pattern interpreted here as remnant micritization related to seafloor diagenesis (I_1 and I_2).
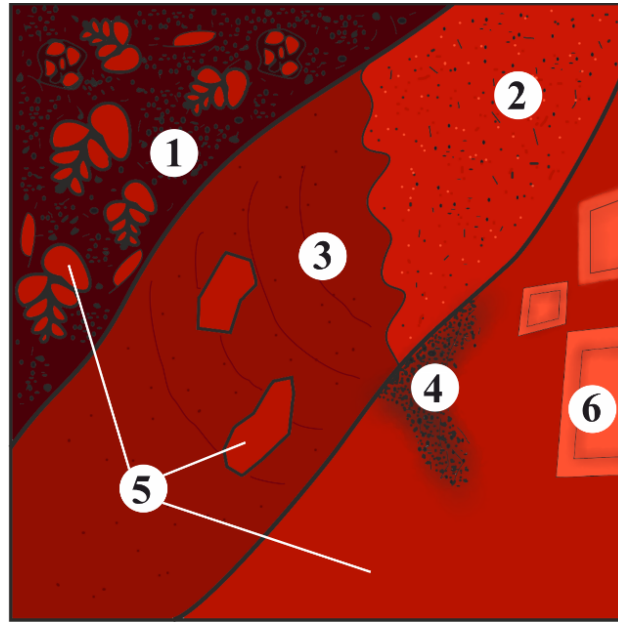
Figure 4.5. Carbonate diagenesis model for the Barremian carbonate reservoir zone in this study, based on both plane light and CL photomicrographs. Chronological events include: Early seafloor micritization processes of (1) micritized-matrix "Mic_x" and (2) micritized-bright luminescent rudist "Rud_m"; recrystallization processes associated with burial diagenesis of (3) dark luminescent rudist "Rud" and (4) bright-luminescent micrite "Mic_y"; and burial-cementation processes of (5) equant/blocky calcite cement "Cm" and (6) dolomite cement "Cm_d".

4.4.2   Clumped isotope (Δ_{47}), $\delta^{18}O$ and $\delta^{13}C$ results

The $\delta^{18}O$ values (Table 4.2; Figure 4.6) range from -7.87 to -5.23‰ with an average value of -7.18‰ for the matrix (Mic_x), -7.23 to -5.31‰ with an average value of -6.60 ‰ for the skeletal grains (Rud) and -8.98 to -8.88‰ with an average value of -8.93‰ for the blocky calcite cement (Cm). The $\delta^{18}O$ values generally increase with to burial depth (Figure 4.6.b). The $\delta^{13}C$ values range from +2.23 to +3.24‰ with an average value of +2.85 ‰ for the matrix, +2.32 to +3.24‰ with an average value of +2.89‰ for the skeletal grains and +3.48 to +3.51‰ with an average value of +3.49‰ for the cement. There is no noticeable trend in $\delta^{13}C$ value with depth except for the skeletal grains (Figure 4.6.c). The highest $\delta^{18}O$ and lowest $\delta^{13}C$ were derived from the matrix and skeletal grains from the deepest sample in the onshore field (Ibrahim-922 well). The cement, however, shows noticeable isotopic signature differences compared to matrix and the skeletal grains (Figure 4.7). The $\delta^{13}C$ and $\delta^{18}O$ bulk isotopic results are consistent with previous analyses of Barremian carbonate reservoir matrix (Vahrenkamp et al., 2014; Barata et al., 2015) and cement (Cox et al., 2010). The data of this study showed a narrower range of values from each rock component compared to previous studies, possibly due to sampling from a narrower stratigraphic interval.

Table 4.2. Carbonate clumped isotope values (Δ_{47}) and bulk isotope composition ($\delta^{18}O$ and $\delta^{13}C$) of reservoir samples from both study locations. The skeletal fragment/rudist are indicated with an 'sk' extension on the end of sample number. The matrix are indicated by 'm1' and 'm2' and the cement by 'cem' extensions after the sample number. Sample Y90101_sk is a micritized rudist and treated as a matrix in the text.

Sample ID	Depth (m)	n	$\delta^{13}C$ (‰, VPDB)	$\delta^{13}C$ SE (‰)	$\delta^{18}O$ (‰, VPDB)	$\delta^{18}O$ SE (‰)	$\delta^{18}O$ fl. [a] (‰, SMOW)	$\delta^{18}O$ fl. SE (‰)	Δ_{47} (‰, I-CDES)	Δ_{47} SE (‰)	Δ_{47} Temperature [b] (°C)
Onshore Giant Field											
K89220_m	2719	4	2.57	0.02	-7.47	0.04	4.95	0.32	0.463	0.004	82
K89220_sk	2719	3	2.57	0.03	-7.14	0.11	3.76	0.38	0.482	0.006	72
L90004_m	2743	3	2.82	0.02	-7.29	0.10	4.68	0.32	0.469	0.005	79
L90088_m	2745	3	3.41	0	-7.69	0.05	5.27	1.15	0.457	0.014	86
L90088_sk	2745	3	2.84	0.01	-6.82	0.05	4.09	1.16	0.482	0.016	72
L90088_cem	2745	3	3.51	0.01	-8.98	0.09	3.86	0.81	0.458	0.011	86
M92641_m	2823	3	3.18	0.01	-6.73	0.03	4.18	0.09	0.482	0.001	72
M92836_sk	2829	4	3.18	0.02	-7.23	0.03	3.07	0.84	0.490	0.011	68
N97205-m[c]	2963	3	2.25	0.02	-5.23	0.14	5.13	0.69	0.490	0.011	68
N97205-sk[c]	2963	3	2.23	0.03	-5.31	0.08	3.73	0.91	0.507	0.013	60
W957510-m[c]	2918	3	3.31	0	-7.26	0.04	4.10	1.05	0.476	0.014	75
W957510-sk[c]	2918	3	3.24	0.03	-6.44	0.04	4.33	0.98	0.484	0.013	71
X90571_m	2760	3	2.86	0.02	-7.01	0.03	4.12	0.82	0.479	0.011	74
X90704_m2	2764	3	3.41	0.04	-7.84	0.12	5.20	0.75	0.456	0.009	87
X90704_m1	2764	3	3.27	0.05	-7.8	0.03	4.77	0.25	0.461	0.003	84
X90704_cem	2764	3	3.48	0.05	-8.88	0.12	3.82	0.99	0.459	0.012	85
Y90101_m2	2746	4	3.29	0.03	-7.21	0.05	5.38	0.83	0.461	0.011	84
Y90101_m1	2746	4	2.88	0.03	-6.98	0.04	4.76	0.09	0.472	0.001	78
Y90101_sk(mic)	2746	4	3.11	0.02	-7.87	0.09	5.56	0.81	0.451	0.010	90
Offshore Giant Field											
Z94708_m	2886	3	3.14	0.09	-7.04	0.18	4.17	0.86	0.478	0.012	74
Z94708_sk	2886	3	3.09	0.10	-6.83	0.05	3.11	0.56	0.494	0.007	66

[a] Calculated diagenetic fluid $\delta^{18}O$ SMOW from calcite $\delta^{18}O$ and Δ_{47} temperature using Kim and O'Neil (1997) equation. [b] The calculated subsurface temperature from Δ_{47} value using Anderson et.al. (2021) equation. [c] Samples obtained below oil water level

The $\Delta47$ values range from 0.456 to 0.490 ‰ (n = 13) with an average value of 0.470 ± 0.017 ‰ for the matrix, 0.451 to 0.507 ‰ (n = 6) with an average value of 0.581 ± 0.028‰ for the skeletal grain, and 0.458 to 0.459 ‰ (n = 2) with an average value of 0.459 ± 0.001‰ for the cement (the laboratory's carbonate standards uncertainty is used for the cement). The clumped isotope temperature ranges from 68 to 90 °C with an average value of ~80 ± 11 °C for the matrix, 60 to 72°C with an average value of 68 ± 6°C for the skeletal grain and 85 to 86°C with an average value of ~85 ± 3°C for the cement (Table 4.1). There is a subtle temperature ($T\Delta_{47}$) decline with an increase in burial depth. The temperatures obtained on skeletal grains are also lower than the temperatures of matrix and cements at the same depth (Figure 4.6.a). The clumped isotope temperatures (Figure 4.5.a) are 32 to 70°C lower

than the present day subsurface, temperatures based on the regional (15 fields) geothermal gradient (Ehrenberg et al., 2020).
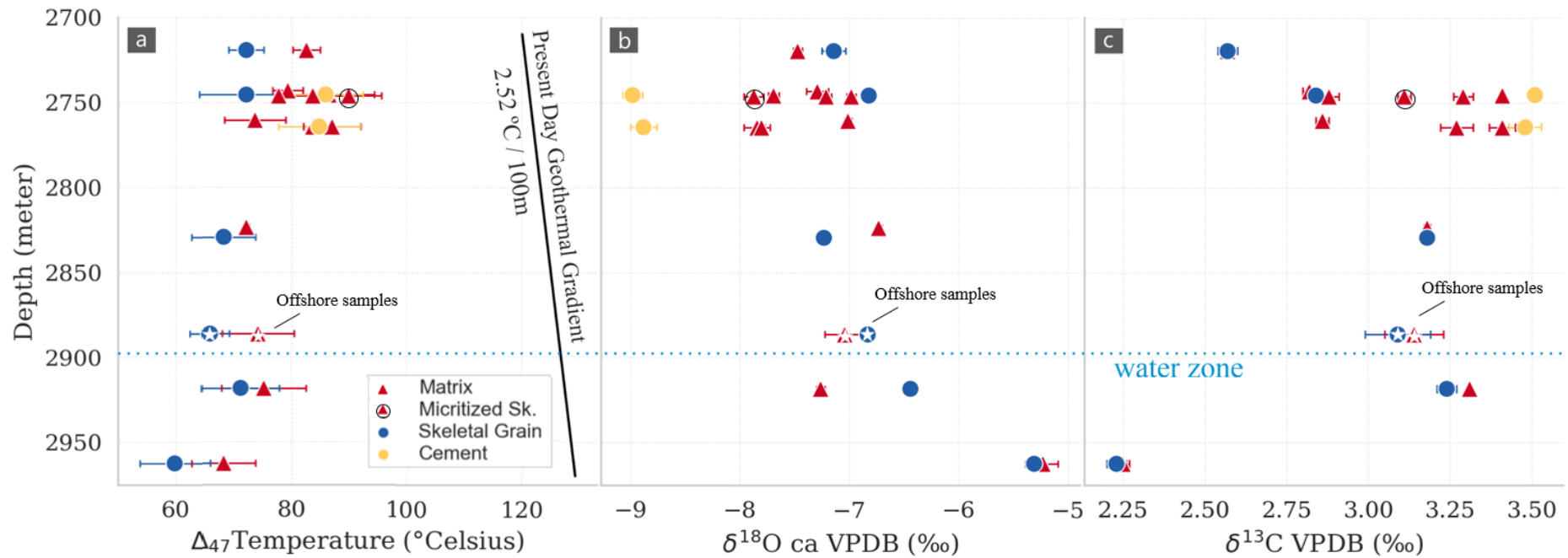
Figure 4.6. Results of (a) Δ_{47} (b) $\delta^{18}O$ and (c) $\delta^{13}C$, all plotted against depth for both study locations. The present-day geothermal gradient in the Barremian carbonate reservoir temperature obtained from previous study of 15 fields onshore and offshore area (Ehrenberg et al 2020) is also shown. The error bar represents 95% confident level of the measurement. Both matrix and skeletal grains results from the offshore field at 2886 meters depth are marked by a star symbol inside the marker. The water zone is located at the base of a hydrocarbon column and the transition zone of the reservoir, where the water saturation (Sw) is 100%.
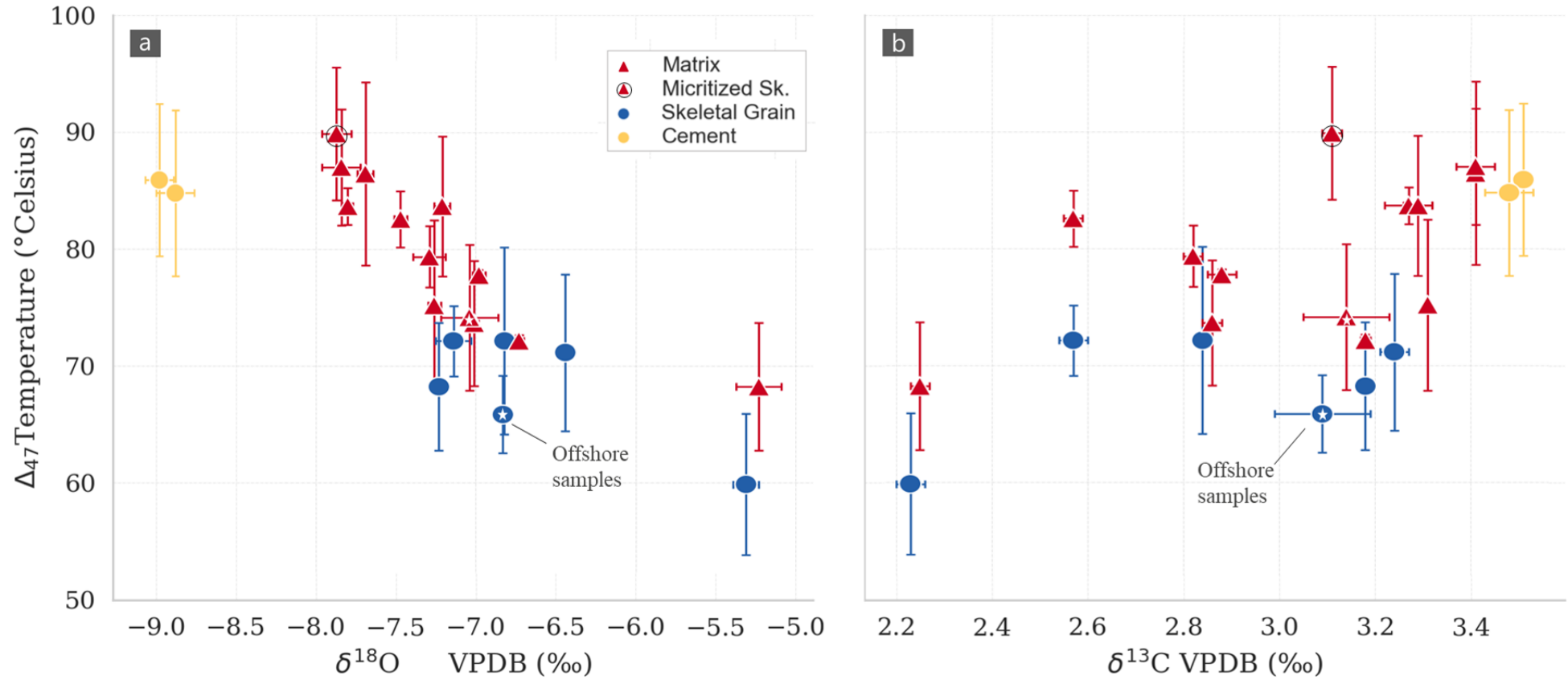
Figure 4.7. Results of (a) $\delta^{18}O$ and (b) $\delta^{13}C$ plotted against Δ_{47}-temperature of sample matrix, skeletal grain and cement for both study locations. The Δ_{47}-temperature was calculated using the Anderson et.al (2021) equation. No distinctive isotopic difference between the onshore and offshore samples.

4.5   Discussion

4.5.1   Water-rock ratio and recrystallization process of different rock fabrics

Except for the samples from the onshore Ibrahim-922 well, the matrix and skeletal grains all formed a 'major group' (Figure 4.8, group 2). This major group is a cluster of bulk isotope ($\delta^{13}C$ and $\delta^{18}O$) data from most of the samples (13 out of 17) and comprised the matrix (Mic_x), skeletal grain (Rud), and micritized skeletal grain (Rud_m) with a distinctive $\delta^{13}C$ range of +2.57 to +3.41 ‰ VPDB and $\delta^{18}O$ of -7.87 to -6.44 ‰ VPDB (Figure 8, group 2). This major group appeared to be similar (overlap) the bulk isotope value to Field "B" with $\delta^{13}C$ range from +2.8 to +3.9 ‰ VPDB and $\delta^{18}O$ of -6.8 to -4.9 ‰ VPDB (Vahrenkamp et al., 2014). The deepest sample from the Ibrahim-922 well, which located in the flank of the anticline, collected below the free-water level, exhibits the lowest $\delta^{18}O$ and $\delta^{13}C$ values of this study (Figure 4.8, group 3) distinguished from the major group possibly due to different diagenetic processes. Further discussion is focused on the major group and the cement to address the first objective of this study, which is to further understand the response of different fabrics to thermal resetting concerning clumped isotopes (Figure 4.8, group 1 and 2). Previously, Δ_{47} temperatures estimated for the matrix carbonates of this Barremian reservoir ranged from 53 to 84°C (Barata et al., 2015) and 59 to 72°C (Vahrenkamp et al., 2014). Matrix temperatures interpreted from the present study are 68 to 90 °C. Based on the maximum temperature reported in all studies, solid-state reordering of clumped isotopes within minerals is unlikely as a temperature of >120°C is required (Henkes et al., 2014). The isotopic composition and the temperature (Δ_{47}) record of the major group here is therefore affected exclusively by fluid-rock interaction.
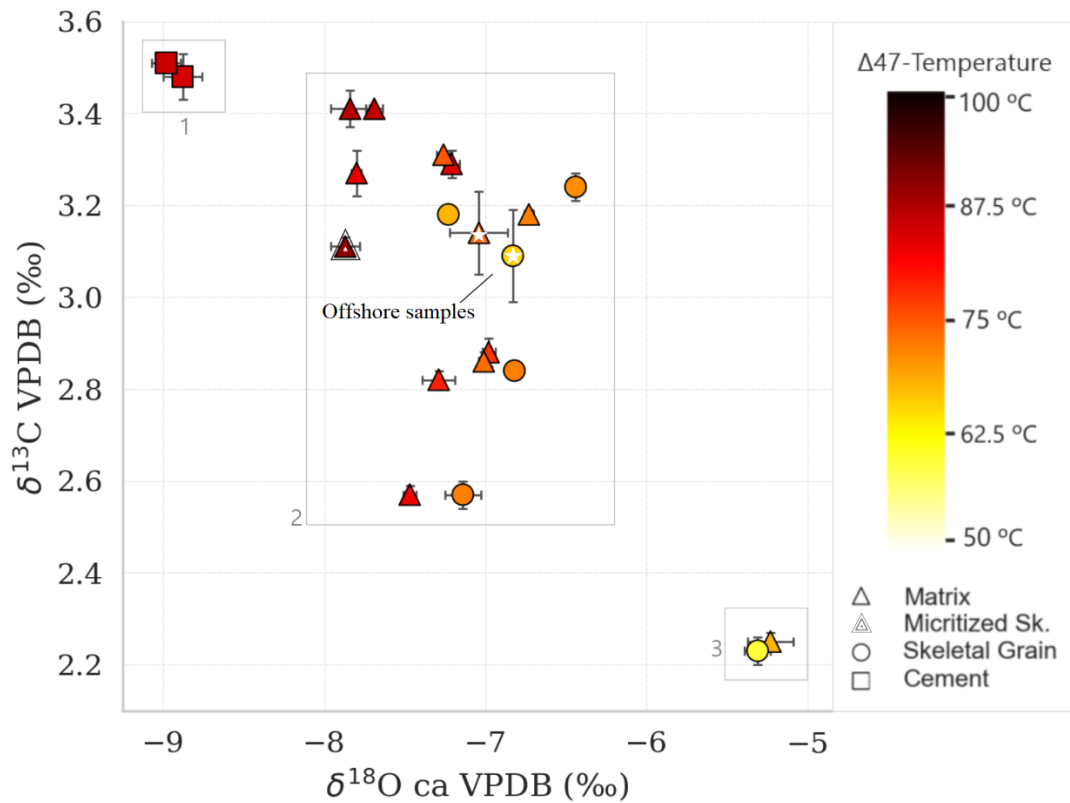
Figure 4.8. Combination of $\delta^{18}O$, $\delta^{13}C$ and Δ_{47}-temperature relationships suggests that there are three distinctive isotope groups. Group 1 comprises only cements, group 2 comprises matrix, skeletal grains and micritized skeletal grain with a range of recorded temperatures. The offshore samples (star symbol) fit in group 2. Group 3 comprises matrix and skeletal grains from the Ibrahim-926 well (N97205).

In the subsurface, fluid-rock interaction may have prompted recrystallization (dissolution-(re)precipitation). The term recrystallization is used to describe a process involving dissolution and precipitation that usually involves changes in crystal size or shape without a change in mineralogy (Flügel, 2010). This term is used here to contrast/differentiate the cementation process where the crystallization of carbonates in the cavities does not involve simultaneous in-situ dissolution and precipitation. In this study, a model was built to test the difference in recrystallization pattern and its fluid-rock interaction between rock fabrics. The model was built based on the assumption that: 1. The sample with the coldest Δ_{47}-temperature represents the original rock condition (or least diagenetic alteration) before continuous recrystallization during progressive burial; 2. the fluid composition of this original rock condition is consistent through burial, implying continuous replenishment/recharge of water of open system. The constant fluid composition of 25.45‰ SMOW (N97205-sk, coldest Δ_{47}-temperature) was used to calculate the traditional temperature value using $\delta^{18}O_{calcite}$ of each sample before it plotted against the true Δ_{47}-Temperature (Figure 4.9). In this model, any data fall to this 1-1 line imply that minerals precipitated at equilibrium temperature from a fluid with identical and consistent $\delta^{18}O_{fluid}$ values through burial (Figure 4.9). The consistency of $\delta^{18}O_{fluid}$ values in the system

during the length of burial period can only be achieved in the open system and in the high water: rock ratio. The test results shows that this is the case for the cement and the skeletal grains, which are distributed along 1-1 line (Figure 4.9). However, the matrix samples fall on a different trend ("micrite trend", no fluid charge) that is distinct (Figure 4.9). This distinctive trend suggests that the matrix tends to recrystallize in a different system due to the $\delta^{18}O_{fluid}$ shift , thus demonstrating a difference in water-rock ratios between rock fabrics.
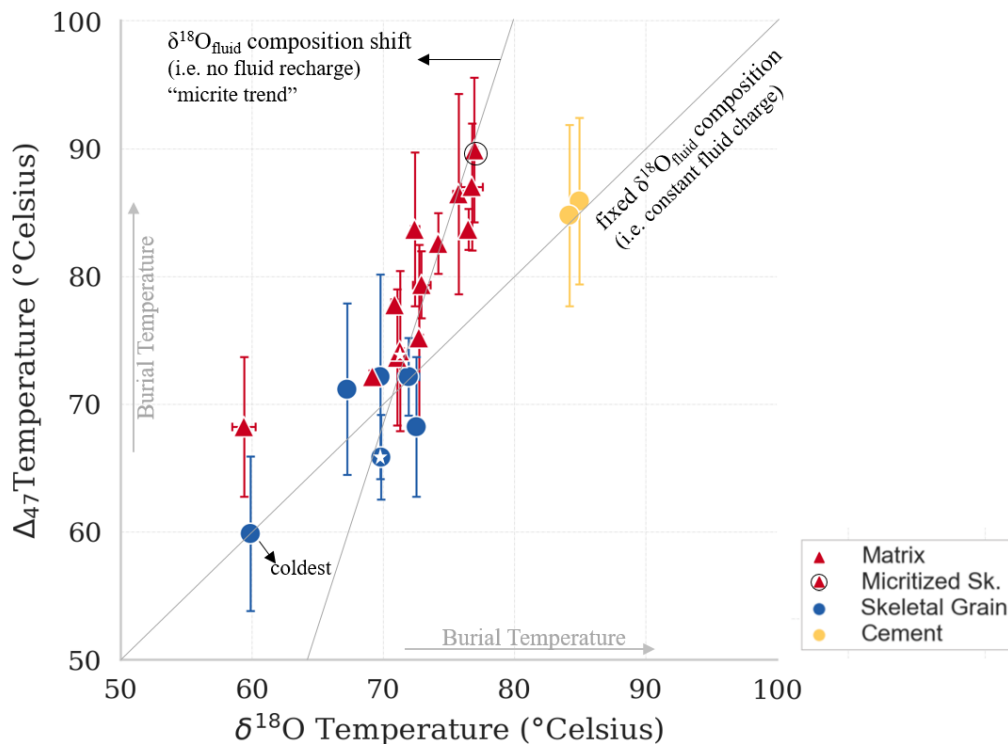
Figure 4.9. A model to test the difference in recrystallization pattern and its fluid-rock interaction between rock fabrics. Using the lowest temperature sample (Δ_{47}T) available (skeletal grains N97205_sk), the best approximation for the initial diagenetic fluid oxygen isotope composition ($\delta^{18}O_{Fluid}$) is obtained. This fluid composition is then used along with the $\delta^{18}O_{calcite}$ of each sample to calculate a δ^{18}O-Temperature (Kim and O'Neil, 1997) and TΔ_{47} plot. Matrix defines a different trend compared to skeletal grains and cement.

4.5.2 Water-rock ratio and nature of diagenetic fluid associated with cements and skeletal grains

To gain more insight into the recrystallization events, it is crucial to also determine the oxygen isotopic composition ($\delta^{18}O_{fluid}$) of the diagenetic fluid. Except for the matrix, the calculated $\delta^{18}O_{fluid}$ values are similar to those reported in previous studies, +0.89 to +4.13‰ SMOW (Barata et al., 2015) and +3.3 to +4.9‰ SMOW (Vahrenkamp et al., 2014). A plot of the calculated $\delta^{18}O_{fluid}$ (SMOW) against TΔ_{47}

and the $\delta^{18}O$ calcite isolines (Figure 4.10) shows that the cements are formed at 85 °C with a $\delta^{18}O_{fluid}$ of 3.8 ‰ SMOW, which is within error of the skeletal grain $\delta^{18}O_{fluid}$ values (3.07-4.33‰, Figure 4.10). The diagenetic fluid ($\delta^{18}O_{fluid}$) consistency between the cement and the skeletal grains (3.07–4.33‰), compared to the enrichment of its mineral's $\delta^{18}O$ composition (−9.0 to −5.3‰), confirms the large water-rock ratios during recrystallization processes on these rock fabrics. This large water-rock ratio environment is predictable (see Chapter 2.1.3), as it was also isotopically recognized in a diagenetic fluid study of Arabian Gulf Coast's (Sheppard, 1986) and Palmarito Formation, Venezuela (Shenton et al., 2015).

The skeletal grains (Rud) comprised a bigger crystal size compared to the enclosed micrite (i.e. Figure 4.2.D and Figure 4.4.H) with lower temperature ($T\Delta_{47}$). The lowest recorded temperature of skeletal grain (60°C, 1SE = 6°C) retains the closest temperature to the 32°C to 43°C corrected-sea surface temperature of Barremian to Aptian period at $< \pm 30°$ paleolatitude (O'Brien et al., 2017). Therefore, it is suggested that this fabric retains the temperature of the early burial stage, which is closer to the temperature record during deposition, possibly because the bigger grain size prevents later episodes of recrystallization. The smaller crystal of the micritized-skeletal segments (Rud_m), however, has experienced a recrystallization process in a low water-rock ratio and records a temperature of 90°C (1SE = 6°C) closer to the present-day formation temperature (122°C, 2746 m), and very similar temperature to the range of enclosed matrix (68°C to 90°C; n = 13) (Figure 4.10).

4.5.3 Water-rock ratio and nature of the diagenetic fluid associated with the matrix

A plot of the calculated $\delta^{18}O_{fluid}$ (SMOW) against $T\Delta_{47}$ and the $\delta^{18}O$ calcite isolines (Figure 4.10) shows that the $\delta^{18}O_{calcite}$ of the matrix samples is near constant at -7‰ yet clumped isotope temperatures vary broadly (66-90˚C) resulting in a relatively large spread in calculated $\delta^{18}O_{fluid}$ (Figure 4.10, Trend 2), suggesting rock buffering system. In rock-buffered case, the oxygen isotope exchange equilibrium is reached with the isotopic compositions buffered by solid rock (see Chapter 2.1.3). Thus, the $\delta^{18}O$ value of the mineral would be retained or consistent through burial recrystallization process while the fluid $\delta^{18}O$ enriched (Figure 4.10, Trend 2). The $\delta^{18}O_{fluid}$ enrichment in this matrix is predictable and is similar to the 'closed-system pathway' in Palmarito and Bird Spring Formation, Venezuela (Shenton et al., 2015). All of these conditions support previous studies that suggested a low water-rock diagenetic environment is intrinsic to non-porous rocks (i.e. matrix) (Budd, 1989) whereas other rock textures in the same formation (in this case, rudist wackestone/packstone) show evidence of higher water/rock ratios. This finding suggest that a crystal size could have more impact to the mineral's proclivity towards recrystallization exceeding the water/rock ratio aspect, as the larger crystal size (large skeletal grain) tend to recrystallize early with lower temperature in contrast to the more

finely crystalline (enclosed matrix) which tend to be more reactive and continue to record a wide range of temperature towards the maximum burial condition. Thus, it is also suggesting that the matrix (micrite) is a more useful recorder of maximum burial conditions and can be key to reconstructing a detailed thermal and diagenetic history.
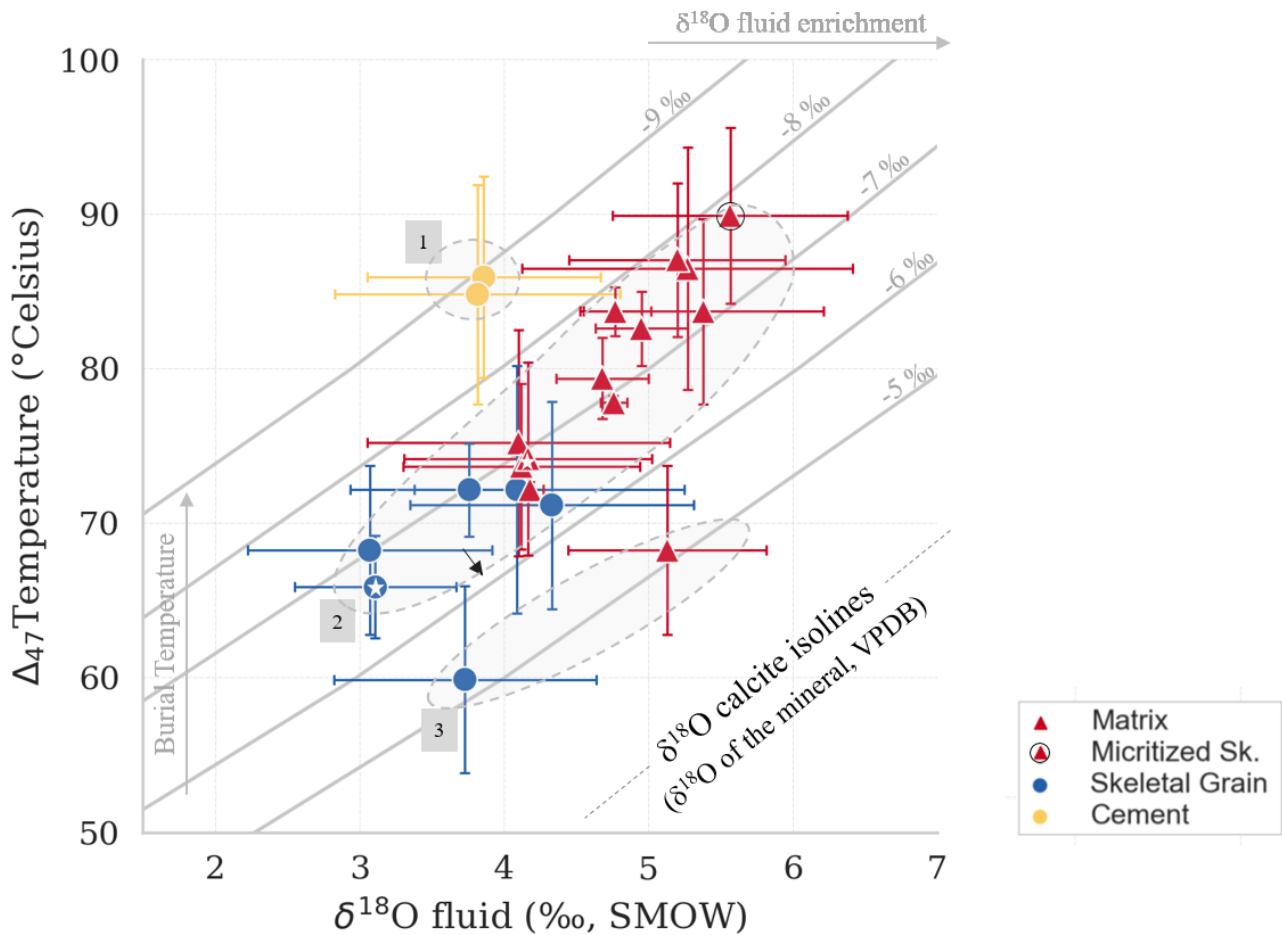
Figure 4.10. Calculated Δ_{47}-temperature versus the calculated $\delta^{18}O$ of the diagenetic fluid. Fluid compositions were reconstructed using the Friedman and O'Neil (1977) equation. The main pattern of the three-isotopic group from the previous plot ($\delta^{18}O$ vs $\delta^{13}C$), particularly group 2 can still be recognized. Both skeletal fragments and cements appear to be have a lower associated $\delta^{18}O_{Fluid}$ than the matrix. The offshore samples (star symbol) is indistinguishable from the onshore samples. The data distribution along the -7‰ (VPDB) $\delta^{18}O_{ca}$ line seems to show precipitation along a constant $\delta^{18}O$ calcite line with increasing temperature and $\delta^{18}O_{fluid}$ enrichment (group 2), suggesting rock-buffered recrystallization.

4.5.4 Timing of recrystallization for each fabric

As stated in the introduction, the carbonate reservoir of the UAE area was chosen because its thermal history, which has been well-studied (Schmoker and Halley, 1982; Schmoker et al., 1985; Alsharhan, 1989; Oswald et al., 1995; Neilson et al., 1996; Brown, 1997; Neilson et al., 1998; van Buchem et al., 2002b; Cox et al., 2010; Vahrenkamp et al., 2014; Barata et al., 2015; Paganoni et al., 2016; Morad et al., 2019; Ehrenberg and Wu, 2019; Ehrenberg et al., 2020). A study of the relationship between oil emplacement and diagenesis has been performed in this reservoir using oil-fluid inclusion and porosity trend analysis (Neilson et al., 1996; Neilson et al., 1998), along with a calibrated-burial and paleotemperature model of the reservoir (Barata et al., 2015). Here, the broad recrystallization-temperature record from the clumped isotope technique was combined with the previous burial and paleotemperature model (Barata et al., 2015) to connect a recrystallization age for the carbonate fabrics based on the temperatures they record. Using this approach, a composite burial history graph was created (Figure 4.11). The upper Barremian carbonate is shown by black burial-history lines in Figure 4.11. The $T\Delta_{47}$ of these results are categorized by each fabric and shown as a matrix (red), micritized matrix (red with dark circle), skeletal grain (blue) and cement (yellow). The data's 95% confidence level is translated into an age error and plotted in the same colored line.
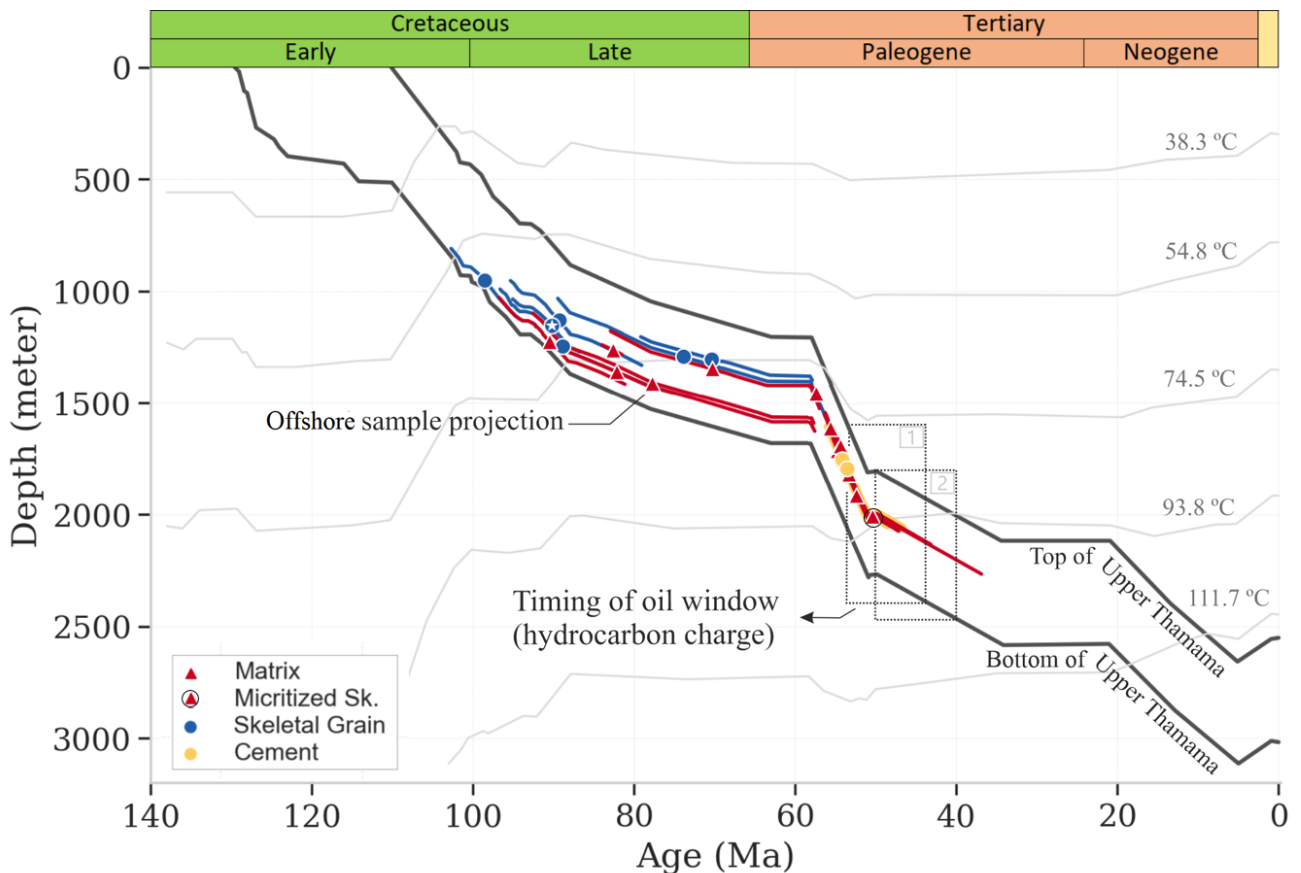
Figure 4.11. Burial history model of the Barremian carbonate formation from the onshore field from Barata et al. (2015) and Ehrenberg et al. (2020a). The dashed box represents the reported timing of

hydrocarbon charge. Box number 1, the oil window and hydrocarbon charging reported at 40-50 Ma (Taher, 1996); box number 2, the hydrocarbon charge reported at 54-55 Ma for the onshore and 44 Ma for the offshore areas (Gumati, 1993). The temperatures recorded by clumped isotopes (colored symbols) suggest cessation of recrystallization at a time compatible with oil emplacement. The offshore samples are projected to this burial history based on similarity of the burial history (Ehrenberg et al., 2020a).

Skeletal grains are likely to have recrystallized during shallow (0.9–1.3 km) burial, given the fact that they record temperatures between 60 °C and 72 °C. Using the existing temperature and time of the calibrated-burial history model in the area (Barata et al., 2015), the timing of precipitation (recrystallization) of the skeletal grains can be traced and determined between 98 and 70 Ma (Blue marker, Figure 4.11). Note that the uncertainties aspect of this burial history is not explained in the previous report and thus cannot be accounted for in this study. Compared to the skeletal grains, the cements are precipitated at greater burial depth and higher burial temperatures (85 to 86°C), implying a timing of precipitation between 54 to 53 Ma (Yellow marker, Figure 4.11). The timing of cement precipitation is compatible with Cenozoic-tectonic events that led to rapid burial (Figure 4.11) followed by uplift and tilting towards the NE along with thrusting and folding in the east of Abu Dhabi (Vahrenkamp et al., 2014).

Meanwhile, the matrix (Red marker, Figure 4.11) seems to have continuously recrystallized over a period of time, recording wide range of temperatures between 68 to 90 °C. This implies a timing of between 90 to 50 Ma (Red marker, Figure 4.11). This result is at odds with previous diagenesis study of this formation, which reported that the matrix recrystallized earlier, in the Cenomanian to Santonian 100-83 Ma (Barata et al., 2015a) or Turonian-Campanian 93-72 Ma (Vahrenkamp et al., 2014). It is recognized that a major difference between this study and the two previous studies (Barata et al 2015, Vahrenkamp et al 2014) is that this study has analysed separate diagenetic fabric, whereas the previous authors analysed bulk-rock. This detailed clumped isotope record on rock fabrics thus sheds light on the detailed diagenetic history of this formation.

4.5.5   Oil emplacement and cessation of diagenesis

The observation that matrix temperatures are 32 °C to 53 °C lower than present-day reservoir temperatures in the two fields suggests that the matrix continuously recrystallized through early burial but ceased reacting before reaching the current maximum burial temperature. Notice that the same process of dissolution-(re)precipitation cessation also occurred below the current oil zone, below oil water contact. This can be explained by hydrocarbon adherence on the carbonate surfaces (i.e. a thin

film of oil formed around pore interiors of carbonate reservoirs) as a result of the contact between positively charged calcite surfaces with the negative dipoles in oil (Zhang and Austad, 2006; Sagbana et al., 2022) which diminish its chemical reactivity even when the pores are filled with water (Frye and Thomas, 1993). The highest recrystallization temperature recorded in the samples is 90°C, which can be translated into a timing of last recrystallization at 50 Ma. The exact age is difficult to pin down, and, using the 95% confidence interval, results in an estimated range of 53 to 37 Ma (Red line extension, Figure 4.11).

Evidence for oil migration events and timing of hydrocarbon emplacement in the cement of the reservoir has been previously studied using petroleum-fluid inclusions (Gumati, 1993; Neilson et al., 1996; Taher, 1996; Neilson et al., 1998). The best estimate for the timing of hydrocarbon charging in the carbonate formation was between 40 and 50 Ma (Taher, 1996)(Dashed box number 2, Figure 4.11), whereas another study suggested between 54 and 55 Ma for the onshore reservoirs and 44 Ma for the offshore area (Gumati, 1993) (Dashed box number 1, Figure 4.11). The overlap between documented ages for hydrocarbon emplacement and the timing of the last recrystallization event suggests that the end of carbonate diagenesis in this reservoir was synchronous with hydrocarbon charging (Figure 4.11). Thus, it is considered likely that the inhibition of diagenesis was a consequence of the displacement of water by hydrocarbons.

The argument as to whether diagenesis (i.e. recrystallization and cementation) continues after hydrocarbon emplacement has been debated for years (Feazel and Schatzinger, 1985; Scholle and Halley, 1989; Walderhaug, 1990; Ramm, 1992; Oelkers et al., 1992; Neilson et al., 1996; Neilson et al., 1998; Cox et al., 2010; Kolchugin et al., 2016) (see Chapter 2.1.4). Here, the results are not supportive of the idea that cementation occurred after petroleum charging (Burruss et al., 1985) or that hydrocarbon charging occurred in the Late Cretaceous for these reservoirs (Alsharhan, 1989; Oswald et al., 1995). Instead, this study supports models that suggest that oil displacement of pore water in the Cenozoic led to retardation of cementation (Neilson et al., 1996; Neilson et al., 1998) (see Chapter 2.1.4). The exact mechanisms responsible for this process are beyond the scope of this study, but previous work has suggested that, for carbonate minerals, the inhibition of new cement nucleation of carbonate begins at lower oil saturation in the pore space than in water-wet siliciclastic minerals (Cox et al., 2010), and that selective loss of permeability can occur after carbonate reservoirs filled with hydrocarbons, interrupting the transport of aqueous carbonate cement species and the effective rate of diffusion of carbonate cement species in water (Cox et al., 2010; Worden, 1999).

4.6 Conclusions

This study demonstrate that different carbonate fabrics recrystallize at different water/rock ratios. The finer-grained matrix continued to recrystallize even at low water/rock ratio, rock-buffered condition, during the deeper burial history in reservoir rocks in the studied Barremian limestone interval. The matrix records a wide range of temperatures, suggesting continuous recrystallization between 90 to 50 Ma based on established thermal histories. The maximum temperature recorded by the matrix is lower than the present-day formation temperature, suggesting the stoppage of dissolution-(re)precipitation diagenetic reactions before the time of maximum burial. Based on a composite burial history model, this diagenesis stoppage is shown to coincide with the timing of oil emplacement. The argument of whether oil emplacement retards diagenesis (cementation) has been debated, and this finding potentially bring a conclusive element for this debate in carbonate systems. The results of this study also extend the application of clumped isotope analyses to petroleum migration study.

CHAPTER 5

CONSTRAINING THE KINETIC PARAMETERS OF CALCITE VS DOLOMITE RECRYSTALLIZATION IN NATURAL SYSTEMS

5.1   Introduction

Clumped isotope (Δ_{47}) thermometry is a technique that recovers the temperature of carbonate formation or recrystallization ($T\Delta_{47}$) of all carbonate phases without relying on knowledge of the $\delta^{18}O$ of the fluid from which the carbonate minerals developed (Ghosh et al., 2006;Eiler, 2007). This technique has been widely employed to reconstruct the burial history of carbonate formations in sedimentary basins (Dennis and Schrag, 2010; Passey and Henkes, 2012; Lechler et al., 2013; Snell et al., 2013; Garzione et al., 2014; Fan et al., 2014; Stolper and Eiler, 2015; Winkelstern and Lohmann, 2016; Gallagher et al., 2017; Lloyd et al., 2017; John, 2018; Lawson et al., 2018; Mangenot et al., 2018; Lacroix and Niemi, 2019; Naylor et al., 2020; Ryb et al., 2021; Hemingway and Henkes, 2021). Although the study of clumped isotopes in buried carbonate formations offers great promise to many geological problems, concerns about post-depositional alteration of the Δ_{47} isotope signature from the effects of burial and exhumation, including diagenetic modification via dissolution-precipitation recrystallization, have emerged, particularly with rock-buffered systems ('closed system' in another study) (Stolper and Eiler, 2015; Brenner et al., 2018; Lloyd et al., 2018; Ryb et al., 2021).

In a rock-buffered system, the low water-rock ratio conditions can still induce recrystallization along with Δ_{47} isotope-exchange reactions. In this case, the $\delta^{13}C$ and $\delta^{18}O$ compositions remain invariant (or incur minor variations) while the Δ_{47} reset reflects the ambient burial or exhumation temperature. Even if no recrystallization occurs, Δ_{47} may be reset during a process known as 'solid-state reordering' (Dennis and Schrag, 2010; Passey and Henkes, 2012; Stolper and Eiler, 2015; Brenner et al., 2018; Lloyd et al., 2018; Ryb et al., 2021).Solid-state reordering, during the exhumation process, may drive the Δ_{47} values to enter the 'apparent equilibrium or blocking temperature' (Passey and Henkes, 2012; Stolper and Eiler, 2015; Ryb et al., 2017) which is related to the cooling rate (Dodson, 1973; Passey and Henkes, 2012). This blocking temperature is independent of the original formation temperature and peak burial temperature (Stolper and Eiler, 2015; Ryb et al., 2017). Understanding this process and its effects on clumped isotope reordering could help researchers understand the details of the thermal and diagenetic histories of carbonate formations during peak burial through exhumation.

Studies of solid-state reordering in different carbonate minerals have been performed to help understand and constrain the burial–exhumation histories. Using controlled heating experiments,

analyses of the kinetic parameters have been conducted on calcite (Passey and Henkes, 2012; Henkes et al., 2014; Stolper and Eiler, 2015; Brenner et al., 2018), dolomite (Lloyd et al., 2018), and aragonite (Staudigel and Swart, 2016; Chen et al., 2019). The cooling rates from these experiments have been inferred within a factor of five or more, from ten degrees per day to a few degrees per million years (Passey and Henkes, 2012). These kinetic parameters have been used as inputs in models to predict the change in Δ_{47} in response to different thermal scenarios. So far, application of such models have been used to constrain the temperature-time (T-t) histories during burial and exhumation in sedimentary basins (Shenton et al., 2015; Gallagher et al., 2017; Ingalls, 2019; Lacroix and Niemi, 2019; Naylor et al., 2020; Ryb et al., 2021; Fernandez et al., 2021) and metamorphic environments (Lloyd et al., 2017; Ryb et al., 2017).

Carbonate minerals, such as calcite and dolomite, are commonly present in ancient rock deposits. Of these, calcite is typically used to reconstruct burial history (Gallagher et al., 2017; John, 2018; Fernandez et al., 2021). Analysis using dolomite needs to be undertaken carefully, as hydrothermal dolomite replacement (Machel and Lonnee, 2002) can sometimes happen under the influence of high temperature, fault-controlled, hydrothermal fluids (Boni et al., 2000; Al-Aasm, 2003; Luczaj et al., 2006). On the other hand, different carbonate rock fabrics in the same sample can yield different recrystallization temperatures through burial (see Chapter 4). It has also been suggested that fine-grained carbonate fabrics are more susceptible to recrystallization during diagenesis (Shenton et al., 2015; Winkelstern and Lohmann, 2016) and record a wider temperature range (see Chapter 4) than their coarse-grain counterparts. These illustrations highlight the complexity of Δ_{47} analysis of carbonate rocks in natural situations that are difficult to replicate in the laboratory. One method to understand Δ_{47} exchange reactions through burial–exhumation complexity is to use geological samples as a natural laboratory, which provides a testing ground for examining the isotopic behaviour of multiple minerals with a similar burial history.

In this study, rocks at various stages of the burial process and across a regional orogeny were used. Five locations were selected based on the burial depth reached by the carbonate intervals, from shallow to deep burial: the Haushi-Huqf in Oman, the Central Oman High, one offshore location in the Arabian Gulf, the Musandam Peninsula (UAE) and the Jabal Akhdar, Central Oman Mountains. The objectives of this study were: (1) to study and contrast recrystallized calcite and (early) dolomite clumped isotope records in samples that have undergone similar burial and exhumation histories, then confirm the difference in kinetics between calcite and dolomite in natural samples;(2) to investigate the cooling phase and compare the apparent blocking temperatures of calcite and early dolomite in various burial–exhumation histories; and (3) to demonstrate a clear relationship between closure temperature and mineral cation ordering in early dolomites and test whether a similar relationship occurred in the

hydrothermal system (late dolomite). Cretaceous, Jurassic, and Permian carbonate formations, developed in a stable carbonate platform in the Arabian Peninsula, were chosen to achieve the study objectives. These carbonate intervals underwent different burial history stages, with some places experiencing a stage of exhumation.
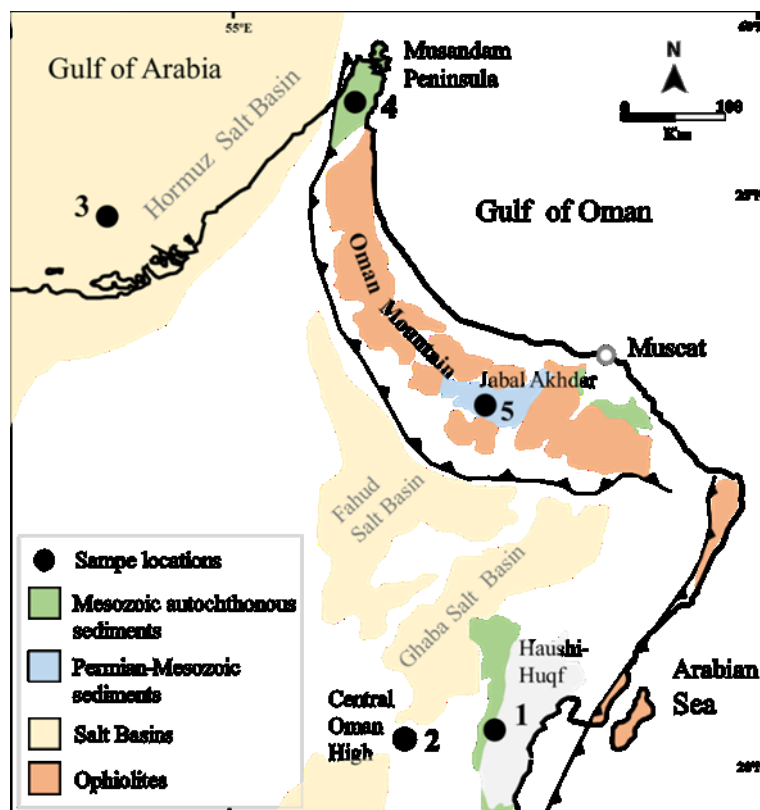
Figure 5.1. Study locations from shallow to deep burial tectonic settings: 1. the Haushi-Huqf in Oman (outcrop); 2. the Central Oman High (core); 3. offshore Arabian Gulf (core); 4. the Musandam Peninsula (outcrop); and 5. the Jabal Akhdar, Central Oman Mountains (outcrop). Regional map modified from (Loosveld et al., 1996; Cooper et al., 2014).

5.2   Geological setting of the sample locations

The stratigraphy of carbonate rocks within the Oman area provides an ideal sequence to explore the clumped isotope variability of recrystallized carbonates because the same stratigraphic intervals were buried to different degrees, from as shallow as 400 m to 9000 m deep (Figure 5.1; Table 5.1) (Ries and Shackleton, 1990; Warburton et al., 1990; van Buchem et al., 2002a; Montenat et al., 2003; Alsharhan and Nairn, 2003; Immenhauser et al., 2004; Rousseau et al., 2005; Abd-Allah et al., 2009; Searle et al., 2014; Beckert et al., 2015; Noufal et al., 2016; Hönig et al., 2017; Bergmann et al., 2018a; John, 2018; Grobe et al., 2019; Carminati et al., 2020; Aldega et al., 2021). The maximum burial stratigraphic depth in each area (Table 5.1) were derived from burial modelling results of Immenhauser et al.,

(2004), Bergmann et.al., (2018), Adlan and John (2023), Carminati et.al., (2020), and Grobe et.al., (2019) (Figure 5.3).

The Cretaceous carbonate interval in Haushi-Huqf (Area 1, outcrop, Figure 5.1) was deposited on a relatively stable shelf (Montenat et al., 2003; Sena et al., 2014) that subsided slowly in a relatively low-temperature regime based on geothermal gradient (John, 2018). The estimation of maximum burial depth reached by the Cretaceous interval in the Haushi-Huqf High is 400 m, based on post-Cretaceous sediment coverage (Immenhauser et al., 2004; Sattler et al., 2005), while clumped isotope estimation using recrystallized oysters suggests a deeper setting at 1.0-1.2km (John, 2018). The Qishn Formation in the same area was deposited during the Barremian-Aptian stages (Beydoun et al., 1993) and is equivalent to the Upper Kharaib and Lower Shu'aiba formations in the northern part of Oman (Figure 5.2). The Central Oman High (Area 2, core, Figure 5.1) is located in the southern part of the Ghaba Salt Basin and comprises stratigraphic units similar to the Haushi-Huqf area (Figure 5.2). The Mesozoic carbonate interval in this area was buried to ~400 to 1200 m (Bergmann et al., 2018a). The Central Oman High area is dominated by long-term uplift, with younger sedimentary units thinning towards, and onlapping, the high (Ries and Shackleton, 1990; Bergmann et al., 2018a). The uplift of both the Central Oman High and the Haushi-Huqf appear complementary to the subsidence of the Ghaba Salt Basin (Ries and Shackleton, 1990).

The Cretaceous Thamama Group, offshore Arabian Gulf (Area 3, core, Figure 5.1), comprises carbonate units that range in thickness from 685 to 762 m and can be divided into four formations: Habshan, Lekhwair, Kharaib, and Shuaiba (Alsharhan, 1990) (Figure 5.2). The Cretaceous interval in this area was buried at ~2500 to 3000 m depth and remains subsided until the present day (Barata et al., 2015b; Ehrenberg et al., 2020).

The Jurassic carbonate interval in the Musandam Peninsula (Area 4, outcrop, Figure 5.1) consists of the ~1,500 m thick Musandam Group, which is made up of three formations (Carminati et al., 2020; Figure 5.2). This interval was overridden during Late Cretaceous obduction by multiple thrust sheets consisting of the Hawasina Complex (Bechennec et al., 1990; Carminati et al., 2020) and ophiolites (Searle and Cox, 1999; Carminati et al., 2020). A burial history model showed that the maximum burial depth reached by the Jurassic interval was ~5100 metres (Carminati et al., 2020). Eocene to Miocene uplift and erosion then took place and were followed by Neogene cooling (Grobe et al., 2019; Carminati et al., 2020).

The Permian carbonate interval of the Akhdar Group in Jabal Akhdar, Central Oman Mountains (Area 5, outcrop, Figure 5.1) consists of a thick succession of carbonates, including the early diagenetic dolomite (Khuff equivalent) that formed as a result of hypersaline brine reflux (Vandeginste et al.,

2014; Beckert et al., 2015). The Middle to Upper Jurassic Sahtan Group in this area is composed of massive carbonate units with ~30 to 400 m thickness (Rousseau et al., 2005). The hydrothermal-late dolomite was emplaced along the Precambrian–Permian unconformity and up through the Permian Akhdar Group (Beckert et al., 2015). Both the Permian and the Jurassic strata in this area are overlain by allochthonous units of the Hawasina complex (Bechennec et al., 1990; Carminati et al., 2020) and ophiolites (Searle and Cox, 1999; Carminati et al., 2020) which reached a maximum burial depth of 8-10 km (Grobe et al., 2019). The area experienced uplift (Hanna, 1990), folding (Warburton et al., 1990) and erosion from Miocene to recent times, exposing the oldest units (Precambrian) in the centre, followed by younger sedimentary beds (up to Cretaceous age) towards the outer rim (Beckert et al., 2015).
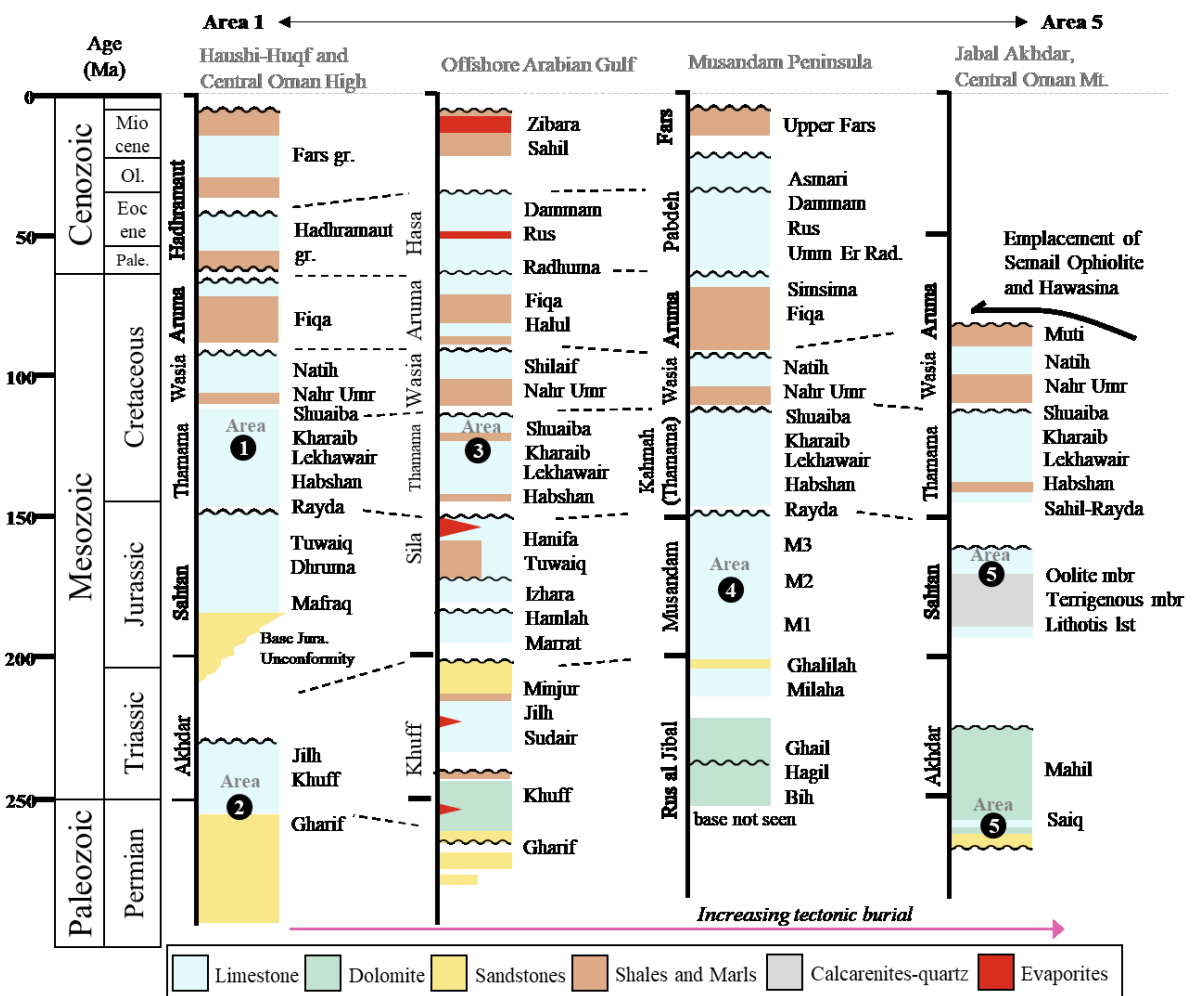
Figure 5.2. The sample position on the stratigraphic column of each region was modified from (Loosveld et al., 1996; Cooper et al., 2018). 1) the Cretaceous Thamama Group in the Haushi-Huqf; 2) the Permian Akhdar Group in the Central Oman High (Bergmann et al., 2018); 3) the Cretaceous Thamama Group in the offshore Arabian Gulf; 4) the Jurassic Mudandam Group in the Musandam

Peninsula; 5) the Jurassic Sahtan Group and Permian Akhdar Group on the Jabal Akhdar, Central Oman Mountains.
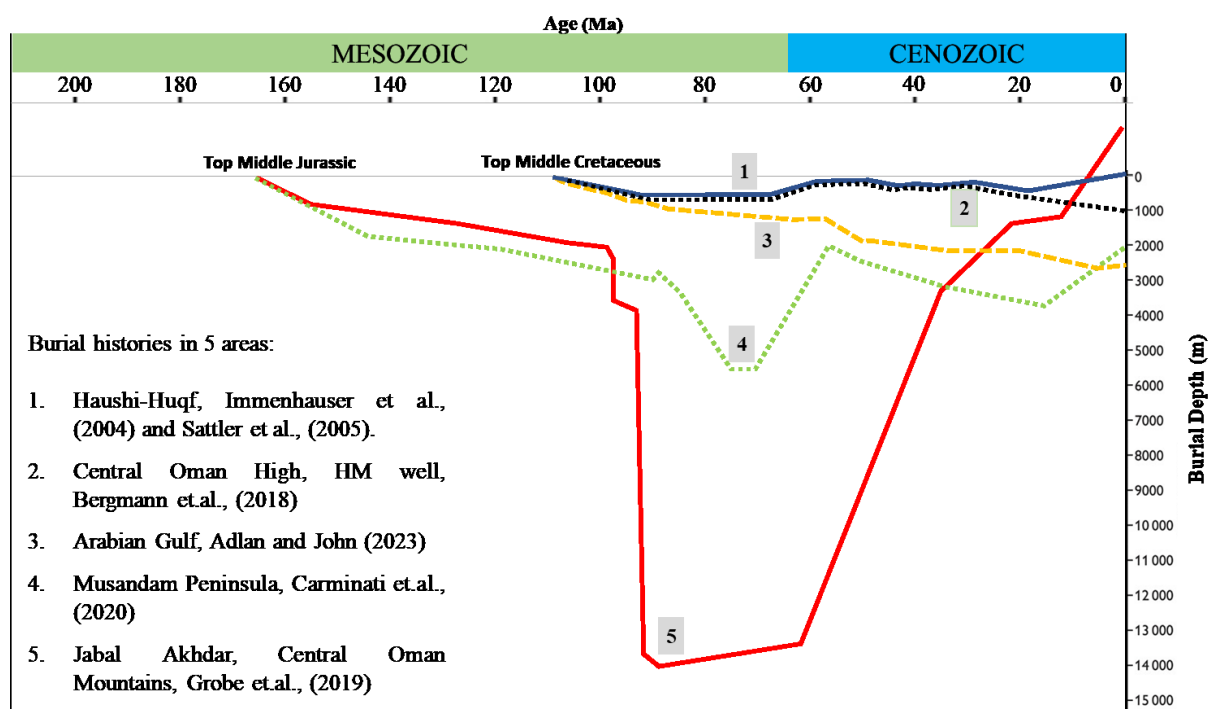
Figure 5.3. Burial histories in 5 areas, differentiated by line colors and dash type. Burial histories in Area 1, 2 and 3 represented by top Middle Cretaceous, while in Area 4 and 5 are represented by top Middle Jurassic.

5.3 Materials and methods

5.3.1 Materials

In total, 34 samples (19 calcites and 15 dolomites) were collected in Oman and the United Arab Emirates during previous field studies by the research group at Imperial College (Vandeginste et al., 2013; Sena et al., 2014; Beckert et al., 2015; John and Hönig, 2015) (Table 5.1). The calcites and dolomites of HM well from Area 2 were collected and published by Bergmann et.al. (2018). In Area 3, Cretaceous samples were collected from subsurface core at ~3000 m to contrast it with Cretaceous samples in Area 1. Except for Area 2 and 3, all samples collected from outcrop (Table 5.1).

Table 5.1 Location and sample source

Area	Formation or Group	age of interval	Maximum burial depth[a] (m)	total sample	Temp. Estimation [c] (°C)	Specimen
1. Haushi-Huqf, Oman	Qishn Fm.	Cretaceous	400	3	47	Outcrop
2. Central Oman High, Oman [b]	Khuff Fm.	Permian	1115-1199	2	55	Core
3. offshore Arabian Gulf	Kharaib Fm.	Cretaceous	2943-2950	8	130	Core
4. Wadi Naqab, Musandam Peninsula	Musandam II	Jurassic	5100	7	168	Outcrop
5. Jabal Akhdar, Central Oman Mt.	Sahtan Gr.	Jurassic	8000	6	169	Outcrop
5. Jabal Akhdar, Central Oman Mt.	Saiq Fm.	Permian	9000	16	187	Outcrop

a) The maximum burial stratigraphic depth of Jabal Akhdar Central Oman Mountains obtained from Grobe et.al., (2019), distance between Jurassic and Permian sampling location is ~1km; The maximum burial depth of Musandam Peninsula obtained from Carminati et.al. (2020) model; Haushi-Huqf burial from Immenhauser et al.(2004) and Sattler et al. (2005).

b) Permian interval data collected from HM well by Bergmann et.al.(2018).

c) Expected temperature of the samples on maximum burial depth: the geothermal gradient for Haushi-Huqf and Oman Central High area were obtained from Bergmann et.al. (2018), the offshore-Arabian Gulf area from Ehrenberg et.al. (2020), Musandam Peninsula area from Ali et.al. (2017) Tibat-1ST well and Oman Mountain from Schütz et.al. (2018) NB-22 well.

Samples from the Cretaceous units in the Haushi-Huqf were laminated mudstone to wackestone, textured limestone, and mud-dominated peritidal dolostone in the Qishn Formation (Sena et al., 2014). Detailed facies descriptions and palaeo-environmental interpretations of the Qishn Formation in this area can be found in Sena et al. (2014). In the offshore Arabian Gulf (the same sample interval as in Chapter 4), packstone to wackestone textured limestone and finely crystalline texture dolostone layers were collected from below the water-oil contact of reservoir zone in the Barremian-Aptian, Kharaib Formation. The detailed facies description of this interval is indistinguishable from the adjacent region (Ehrenberg et al., 2018) and the palaeo-environmental interpretation of this interval can be found in van Buchem et al. (2002a) and Yamamoto et al. (2018). The dolomite in this formation is most abundant in the lower two-thirds of the interval (Ehrenberg et al., 2016).

The Jurassic rock samples were obtained from two locations: the Musandam Peninsula and the Jabal Akhdar (Figure 5.2). In the Musandam Peninsula, microbial laminate mudstone was collected from the Musandam II Formation outcrop in Wadi Naqab (Hönig and John, 2015). The dolomite was collected from the dolomitised burrow infilling of the mudstone of the Musandam II Formation outcrop. Facies description and palaeo-environmental interpretation of this formation can be found in Hönig and John (2015). In the Jabal Akhdar, Central Oman Mountains, grey limestone and brown stratabound dolostone were collected from the Jurassic Sahtan Group outcrop (Vandeginste et al., 2013). The limestone bed sampled consists of mudstone to wackestone texture with a previous report of microsparitization (Vandeginste et al., 2013). The stratabound dolomite in this area was interpreted to have formed during early diagenesis (Vandeginste et al., 2013).

In addition, Permian outcrop samples were also collected 1 km away from the Jurassic samples, towards the centre of Jabal Akhdar dome. Finely laminated limestone and finely crystalline brown early dolomite were collected from the Saiq Formation outcrop (Beckert et al., 2015). As a comparison,

previously published Permian data from the Central Oman High (calcite and dolomite from HM well HM-13-1 at 1115 m depth and HM-14-1 at 1199 m depth) are also used (Bergmann et al., 2018a) (Figure 5.2).

Calcite and dolomite were sampled from fine grained matrix, as these are more prone to recrystallization (see Chapter 4). In an attempt to collect single mineral phases, cut surfaces were sampled using a dental drill at the lowest possible speed (1000-2000 rpm). To obtain a homogeneous powder size, the samples were subsequently gently crushed with an agate mortar and pestle and then sieved through a 125 μm sieve.

5.3.2 Petrography

Petrographic observations were made using a transmitted light Zeiss Axioskop 40, followed by cathodoluminescence (CL) microscopy on a Nikon Eclipse 50i microscope equipped with a CITL cathodoluminescence MK5-2 stage. The operating conditions for the CL stage were a current of 315 μA, an accelerating voltage of 15 kV, and a vacuum operating at 0.003 mBar.

5.3.3 FTIR mineralogy and X-ray diffraction analysis of dolomite

Fourier transform infrared spectroscopy (FT-IR-Spectrometer Nicolet 5700) was applied to all samples to screen for mineralogical homogeneity and to qualitatively estimate mineral content (calcite or dolomite) following Henry et al. (2017).

In addition, X-ray diffraction characterization for dolomite samples focused on quantification of dolomite content, dolomite stoichiometry, and dolomite cation ordering (Kaczmarek and Sibley, 2014). Measurements of stoichiometry and cation ordering were carried out in the Carbonate Petrology and Characterization Laboratory at Western Michigan University. Measurements were undertaken on a Bruker D2 Phaser Diffractometer equipped with a CuKα anode, using a 2θ range of 20-60˚, a step size of 0.018˚/step, and a count time of 1 s/step. Peak positions were calibrated using powdered fluorite (CaF_2) as an internal standard (Kaczmarek and Thornton, 2017).

The percentage of dolomite was calculated using the background-corrected intensity ratio of the dolomite [104] reflection to the sum of the intensities of the dolomite [104] and calcite [104] reflections (Royse et al., 1971). Dolomite stoichiometry was calculated using the calibrated position of the dolomite [104] reflection consistent with the approach developed by Lumsden (1979). All values of dolomite stoichiometry in the database are reported as mole % $MgCO_3$. The degree of cation ordering

was determined using the ratio of the background-subtracted intensities of the dolomite [015] and [110] reflections following the methods of Goldsmith and Graf (1958) and Gregg et al. (2015).

5.3.4 Clumped isotopes

Clumped isotopes, $\delta^{18}O$ and $\delta^{13}C$ measurements were carried out in the Qatar Stable Isotope Laboratory at Imperial College London using fully automated IBEX (Imperial Batch EXtraction) system. The detailed method is described in Chapter 2. Calculations and corrections of raw Δ_{47}, $\delta^{18}O$ and $\delta^{13}C$ were performed using the free software Easotope (John and Bowen, 2016). The bulk isotopic value of $\delta^{18}O$ is corrected for acid digestion at 90°C by multiplying the value by 1.0081 using the published fractionation factor of (Kim et al., 2007) for calcite and 1.0093 for dolomite (Rosenbaum and Sheppard, 1986).

5.3.5 Modeling

A forward solid-state reordering model was created to test various geological scenarios that might explain the calcite and dolomite Δ_{47} records and also to find potential benefits of reconstructing thermal history using co-occurring calcite and early dolomite. Two models were examined based on the competing burial/exhumation scenarios. For the Arabian Gulf burial scenario, the model assumes an initial mineralization temperature for calcite and dolomite of 25°C (Δ_{47}=0.590‰ with 0.01‰ uncertainty), compatible with estimates for equatorial sea surface paleotemperatures (O'Brien et al., 2017). Based on the present-day formation temperature, a final temperature of 130°C (Δ_{47}=0.394‰) was assumed reflecting the maximum burial depth. Reordering models were simulated for a 125 Ma burial period initialized from 0 to 125 timescales, respectively, according to the depositional ages of the interval (Barremian). All calculations were performed using *isotopylog*, an online accessible open-source package in Python 3.7 (Hemingway, 2020). In contrast, the Jabal Akhdar exhumation scenario assumes an initial peak burial temperature for calcite and dolomite of 280°C (Δ_{47}=0.277‰). Based on present-day surface temperatures, an end temperature of 25°C (Δ_{47}=0.590‰) was used. A previous study suggested that uplift on Jabal Akhdar was initiated at ~80 Ma (Grobe et al., 2019). Thus, the reordering models were simulated for the past 80 million years.

The models tested the paired-diffusion model equation (Stolper and Eiler, 2015) on calcite minerals and the disordered kinetic model equation (Hemingway and Henkes, 2021) for both calcite and dolomite. The calcite mineral in the paired-diffusion model (Stolper and Eiler, 2015) uses specific activation energy (μ_E) of 250.7 ± 13.6 kJ mol−1 and pre-exponential factor (v_0) of 34.2 ± 2.3 min−1 (Hemingway and Henkes, 2021), while the disordered kinetic model uses activation energy (μ_E) of

224.3 ± 27.6 kJ mol-1 and pre-exponential factor (v_0) of 31.5 ± 4.6 min-1 (Hemingway and Henkes, 2021). The dolomite in the disordered kinetic model uses a specific activation energy (μ_E) of 230.3 ± 47.7 kJ mol-1 and a pre-exponential factor (v_0) of 29.0 ± 6.8 min-1 (Hemingway and Henkes, 2021). This paired reaction-diffusion model attributes the change in Δ_{47} to the neighboring singly-substituted carbonate group pair interactions, where the group can then diffuse through the crystal lattice to exchange isotopes (Stolper and Eiler, 2015). On the other hand, the recent adaptable disordered kinetic model attributed the change in Δ_{47} as random-walk O_{18} diffusion which increases the reordering rates naturally through the carbonate lattice (Hemingway and Henkes, 2021). The model predicts Δ_{47} values at sequential time steps of the imposed temperature-time (T-t) histories. The predicted Δ_{47} values were then compared to the measured Δ_{47} in the samples. Details of the kinetic model derivation, including the Arrhenius parameters adaptation, are described in Hemingway and Henkes (2021). The final predicted Δ_{47} values for the present day were then directly compared to the measured Δ_{47} of the samples. The temperatures from Δ_{47} values were then calculated using Anderson et al. (2021b) equation.

5.4   Results

5.4.1   Petrography observations

Cathodoluminescence imaging of the limestone show that the Cretaceous samples in Area 3 consist of wackestone to packstone textures with clear sparite crystal replacement inside the skeletal fragments with micritic matrix (Figure 5.4.A). In this figure, dully-luminescent sparitic patches or equant-blocky calcite exist within the interparticle porosity and also in the skeletal remnants as a replacement. The micrite in this limestone shows a range of dark to bright red luminescence (Figure 5.4.A). Towards the deeper burial realm of Musandam Peninsula (Area 4, maximum stratigraphic depth of 5100 m), the Jurassic interval consists of micritized-ooids wackestone with medium-sized dolomite rhombs (10-30 μm in diameter) floating in a calcite cement matrix (Figure 5.4.B). In this figure, the replacement of dolomite patches is recognized inside the ooids nuclei. A trace of dedolomitization is recognized in some of the dolomite cement (Figure 5.6.F). In the deepest burial realm of Jabal Akhdar (Area 5, maximum stratigraphic depth of 8000 m), the Jurassic interval consists of micrite-dominated mudstone-wackestone with patches of sparite or blocky calcite crystals existing within clasts or skeletal remnants (Figure 5.5.C). The Permian interval consists of micritic mudstone and wackestone with equant-blocky calcite crystals existing within skeletal remnants (Figure 5.5.D). Equant-blocky calcite was found in both Jurassic and Permian samples in Jabal Akhdar is non-luminescent (Figure 5.5.C, D).

69

Cathodoluminescence photomicrographs of dolostones show that the Cretaceous samples in offshore Arabian Gulf (Area 3) consist of fine to medium, nonplanar-a to planar-e dolomite crystals that have irregular or extensively interlocking contacts between rhomb crystals (Figure 5.6.E). In Musandam Peninsula (Area 4), variation of dolomite crystals in the Jurassic interval is recognized from fine to medium, nonplanar-a to planar-e dolomite with cloudy/sucrostic texture of brown-fine crystals and interlocking contacts (Figure 5.6.F). A signature of calcification/dedolomitization with dull luminescence exists inside the dolomite nuclei in Musandam Peninsula. In the deepest burial stage of Jabal Akhdar, the Jurassic interval consists of medium, planar-e dolomite crystals with intens fine-micritic dolomite (Figure 5.7.G). Some irregularities on the rim of dolomite rhombs with inclusion-rich nuclei are recognized (Figure 5.7.G). Meanwhile, the Permian interval in Jabal Akhdar consists of fine to medium, planar-e to nonplanar-a dolomite crystals interlocking with each other (Figure 5.7.H). In Figure 5.7.H, the contact between crystals and the fine crystal matrix in this sample appears to have brighter luminescence compared to the darker dolomite rhombs. Details of sample name information in each area are shown in Table 5.2.
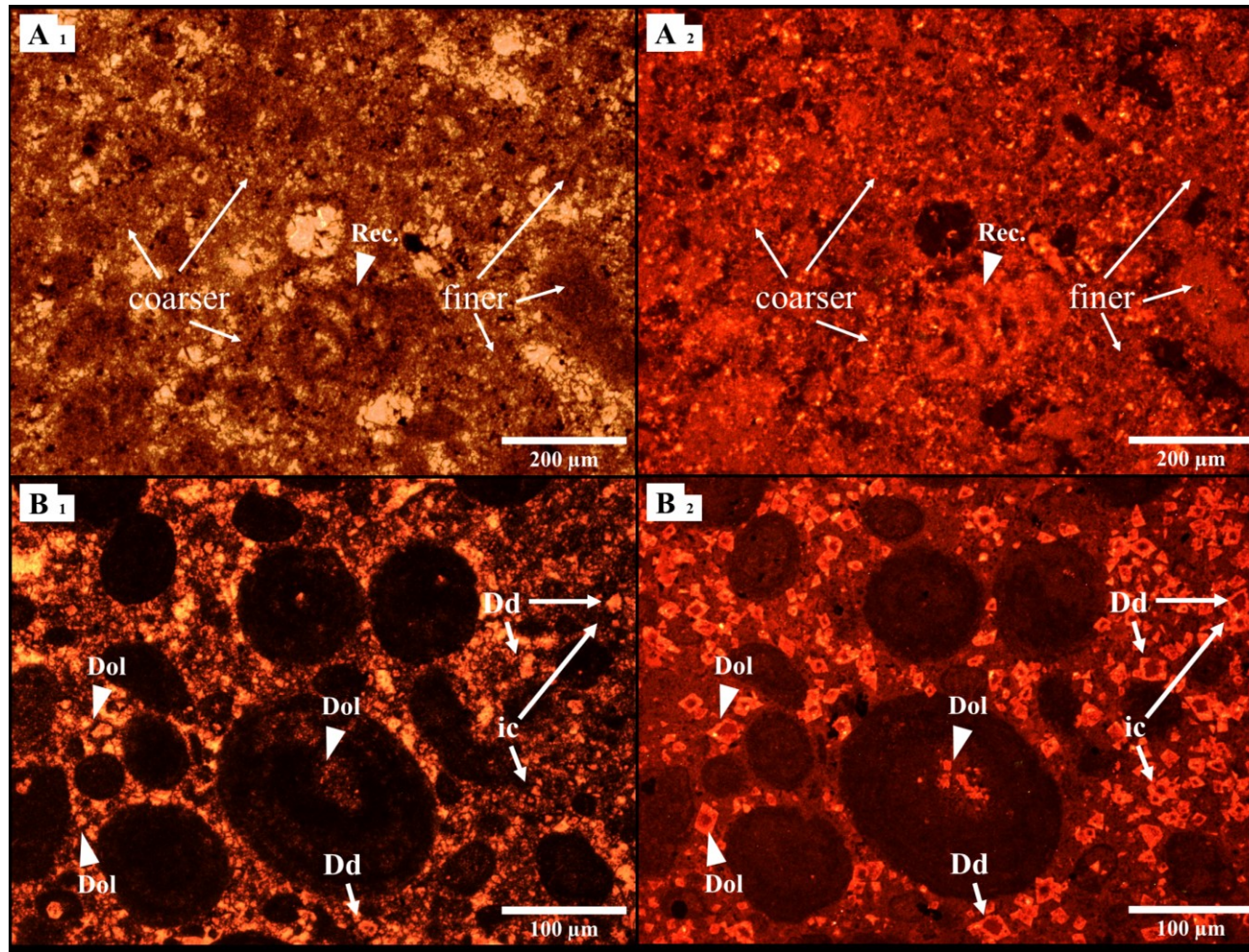
Figure 5.4. Limestone photomicrographs with plane light (left) and cathodoluminescence (right). A) Ibrahim6840 Cretaceous sample from offshore Arabian Gulf, Area 3, comprises wackestone-packstone texture, recrystallized skeletal grain, and inhomogenous crystal sized-micrite with series of dark to bright red luminescence. B) WN625_Gry Jurassic sample from Musandam Peninsula, Area 4, comprises micritized-ooids wackestone with dolomite rhombs float in a calcite cement matrix and ooids. A trace of calcitification (dull luminescence) is recognized inside dolomite rhombs. 'Rec.': recrystallized foram; 'Dol': dolomite cement; 'Ms': micro-seam fracture; 'ic': interlocking contact; 'Bc': equant-blocky calcite.
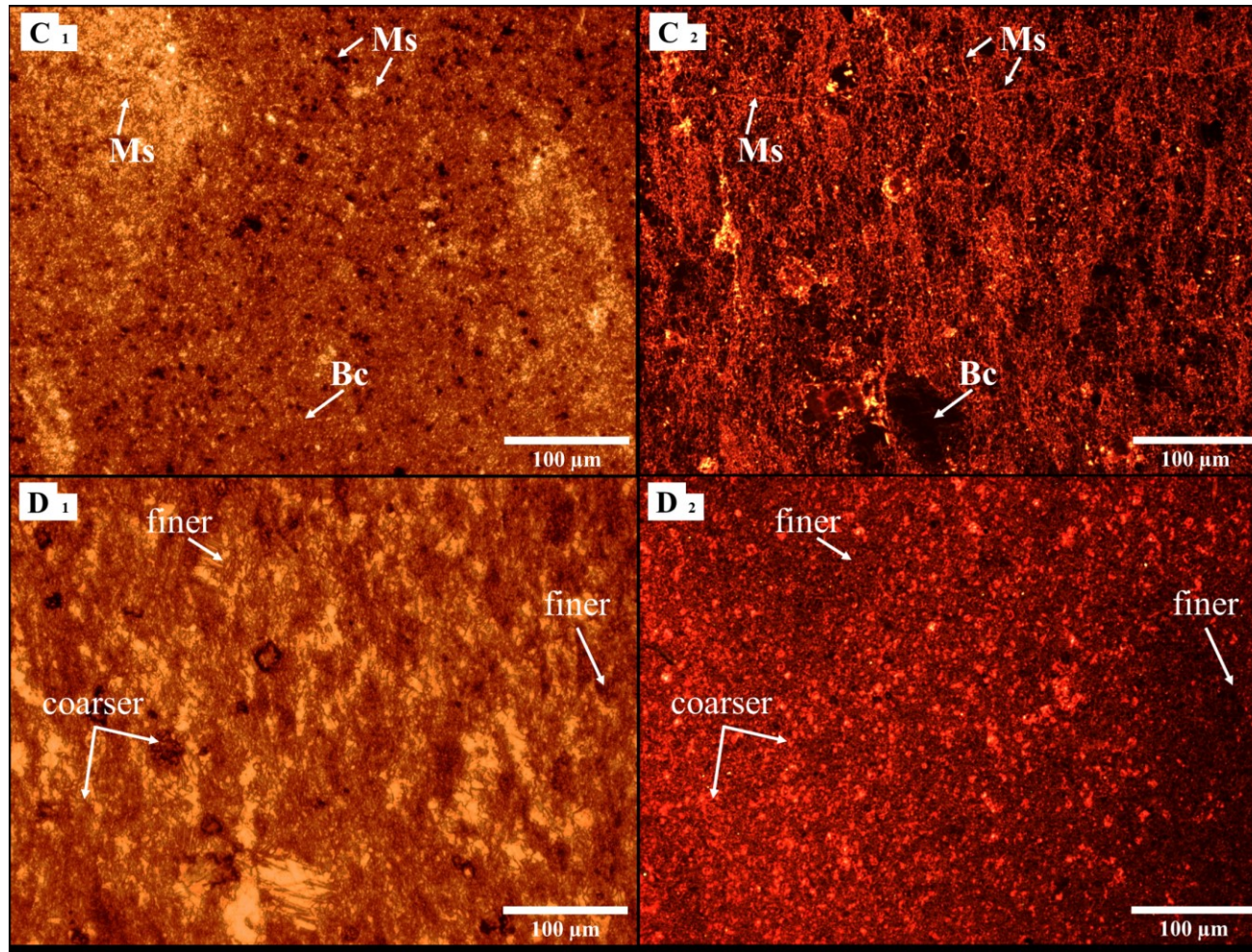
Figure 5.5. Limestone photomicrographs with plane light (left) and catho-doluminescence (right). C) Mist-6 Jurassic sample from Jabal Akhdar, Area 5, comprises micrite-dominated mudstone-wackestone with patch of sparite or equant-blocky calcite crystal. D) Ak-7 Permian sample from Jabal Akhdar, Area 5, consists of mudstone with inhomogenous crystal sized-micrite. 'Rec.': recrystallized foram; 'Dol': dolomite cement; 'Ms': micro-seam fracture; 'ic': interlocking contact; 'Bc': equant-blocky calcite.
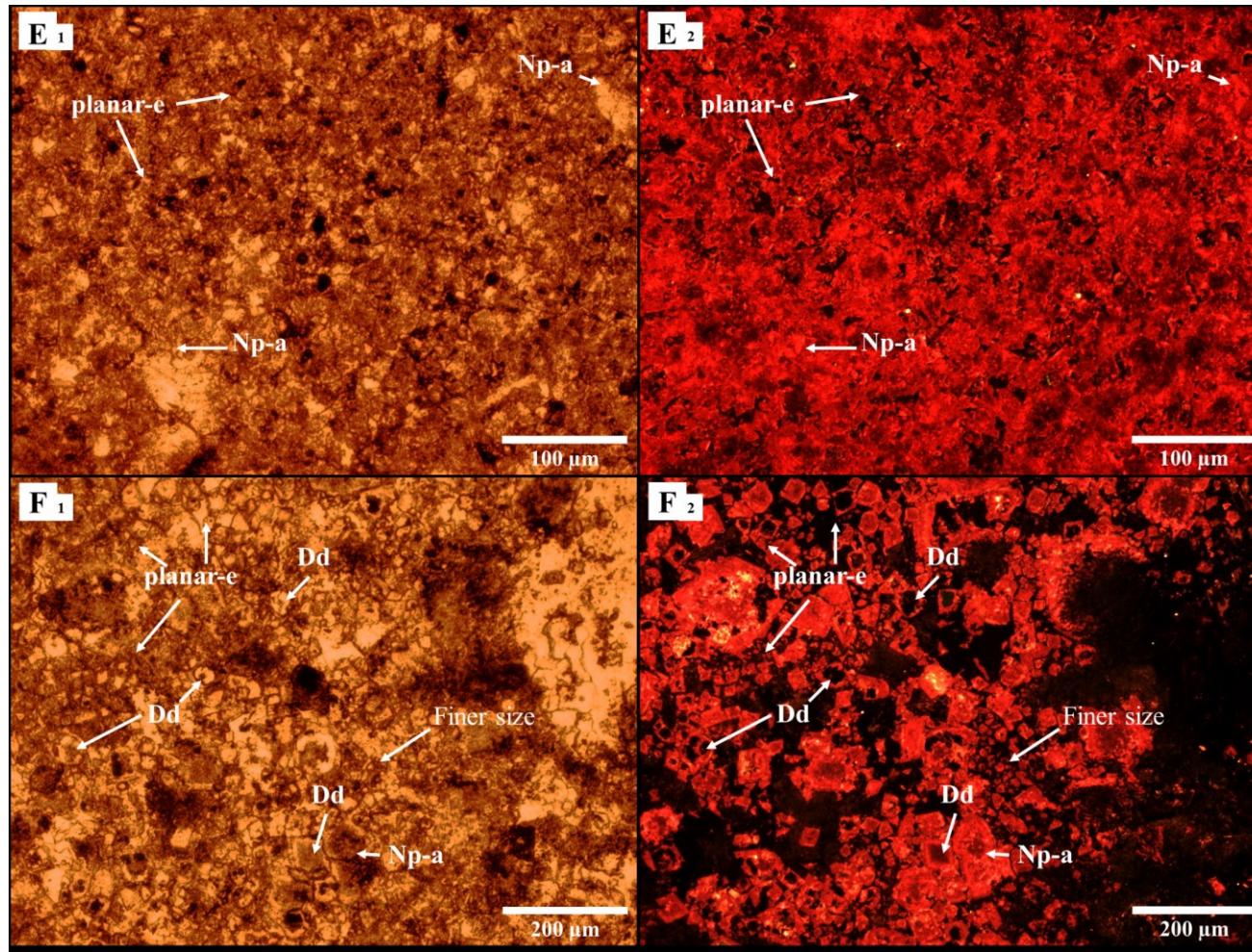
Figure 5.6. Dolostone photomicrographs with plane light (left) and cathodoluminescence (right). E) Ibrahim652 Cretaceous sample from offshore Arabian Gulf, Area 3, consists of fine to medium nonplanar-a to planar-e dolomite crystals with irregular or extensively interlocking contact. F) WN526_Gry Jurassic sample from Musandam Peninsula, Area 4, consists of fine to medium nonplanar-a to planar-e dolomite crystals with a trace of calcitification/dedolomitization (dull luminescence) recognized inside rhomb nucleus. 'Dd': dedolomitization; 'ic': interlocking contact; 'Np-a': nonplanar-a
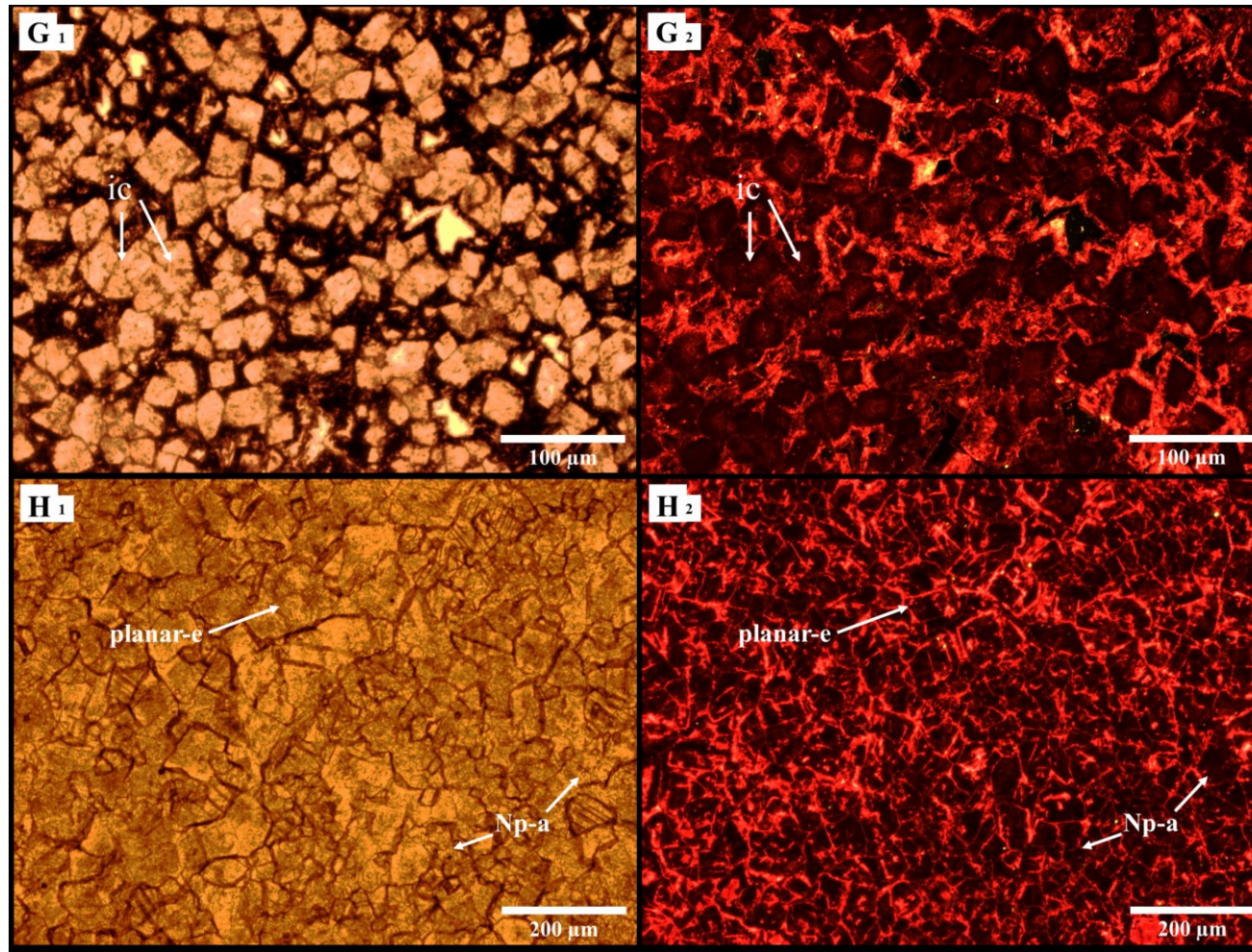
Figure 5.7. Dolostone photomicrographs with plane light (left) and catho-doluminescence (right). G) Mist-9 Jurassic sample from Jabal Akhdar, Area 5, comprises dark luminescent planar-e to planar-s dolomite with interlocking crystals. The micritic matrix in catho-doluminescence image appears to have brighter luminescence compared to the medium-sized rhomb crystals. H) Ak-25 Permian samples from Jabal Akhdar, Area 5, consist of fine to medium planar-e to nonplanar-a dolomite crystals interlocking each other. 'Dd': dedolomitization; 'ic': interlocking contact; 'Np-a': nonplanar-a

5.4.2   δ¹⁸O and δ¹³C results

The bulk isotope composition ($\delta^{18}O$ and $\delta^{13}C$, ‰ VPDB) of calcite and early dolomite (Table 5.2) are presented in Figure 5.5 A. From shallow to deep stages of burial, the $\delta^{18}O$ and $\delta^{13}C$ of the samples increase from Area 1 towards Area 5 depending on the age of the interval:

Area 1, Haushi-Huqf, shows that the $\delta^{18}O$ values of Cretaceous carbonates in this study range from -5.78 to -0.31‰ (Figure 5.5 B), whereas the $\delta^{13}C$ values range from -0.04 to 1.70‰. In comparison to other Cretaceous samples, the $\delta^{18}O$ values in oysters reportedly range from -2.88 to -2.47‰ and $\delta^{13}C$ values range from 0.15 to 1.4‰ (John, 2018). The dolomite reportedly ranges from -1.46 to -0.21‰ for $\delta^{18}O$ and -0.46 to 2.5‰ for the $\delta^{13}C$ (Sena et al., 2014).

A previous report on Area 2, Central Oman High, revealed that the $\delta^{18}O$ values of Permian carbonates range from -4.4 to 1.07‰ (Bergmann et al., 2018a) (Figure 5.5 D), while $\delta^{13}C$ values range from -0.63 to 4.88‰ (Bergmann et al., 2018a). In Area 3, offshore Arabian Gulf, the $\delta^{18}O$ values of Cretaceous carbonates range from -8.37 to -4.86‰ (Figure 5.5 B), whereas the $\delta^{13}C$ values range from 2.92 to 4.85‰. In the same formation of the same anticline, the calcite samples from the shallower-oil rich reservoir interval range from -6.94 to -6.74‰ for $\delta^{18}O$ and 3.05 to 3.32‰ for the $\delta^{13}C$ (see Chapter 4) (Figure 5.4 B).

In Area 4, Musandam Peninsula, the $\delta^{18}O$ values of Jurassic carbonates range from -4.24 to -2.74‰ (Figure 5.5 C) and the $\delta^{13}C$ values range from -3.97 to 2.32‰. The $\delta^{18}O$ values in this area were previously reported to range from -9.27 to -6.97‰, and $\delta^{13}C$ values range from -2.37 to 1.82‰ for calcite (Vandeginste and John, 2012). The $\delta^{18}O$ values range from -4.95 to –1.74‰ and $\delta^{13}C$ values range from -2.71 to -1.73‰ for dolomite (Vandeginste and John, 2012) (Figure 5.5 C). In Area 5, Jabal Akhdar, the $\delta^{18}O$ values of Jurassic carbonates range from -8.14 to -3.38‰ (Figure 5.5 C), while the $\delta^{13}C$ values range from 0.05-2.03‰. The $\delta^{18}O$ values of Permian carbonates range widely from -7.49 to 0.38‰, while the $\delta^{13}C$ values range from 2.00 to 6.38‰ of $\delta^{13}C$ values (Figure 5.5 D).

5.4.3   Clumped isotopes (Δ₄₇)

The Δ_{47} values (‰, I-CDES) of Cretaceous carbonates in this study range from 0.522 to 0.541‰ in the Haushi-Huqf samples and show an overall decrease toward the offshore Arabian Gulf region (0.368 to 0.504‰, Table 5.2). The calcite samples from the Arabian Gulf have higher Δ_{47} values compared to dolomites in the same stratigraphic interval. The Jurassic Δ_{47} values range from 0.343 to 0.479‰ for the Musandam Peninsula samples, similar to the values in the Jabal Akhdar area (0.323 to 0.418‰,

Table 5.2). The Permian Δ_{47} values for the Jabal Akhdar samples overall range from 0.298 to 0.442‰ (Table 5.2). Both Jurassic and Permian calcite samples in Jabal Akhdar have higher Δ_{47} values compared to dolomites in the same stratigraphic interval.

The maximum burial depth reached by the carbonate samples increases from Area 1 towards Area 5 and is reflected in the clumped isotope temperature ($T\Delta_{47}$) in Table 5.2. The calculated clumped isotope temperature for the Cretaceous carbonates ranges from 45°C to 53°C in the Haushi-Huqf region and is higher in the offshore Arabian Gulf region (61°C to 154°C, Table 5.2). The Jurassic sample temperatures range from 74°C to 182°C for the Musandam Peninsula samples, and range from 112°C to 208°C in the Jebel Akhdar region (Table 5.2). The Permian temperature for the Jabal Akhdar samples ranged from 95°C to 248°C (Table 5.2). The temperature difference between late dolomite and early dolomite in this area was relatively small.

Table 5.2. Carbonate clumped isotope values (Δ_{47}) and bulk isotope composition ($\delta^{18}O$ and $\delta^{13}C$) of areas used in the study, including its mineralogical information.

Sample Information	Mineralogy-FTIR[a]	Depth[b] (m)	% Dolomite XRD	n	$\delta^{13}C$ (‰,VPDB)	$\delta^{13}C$ SE (‰)	$\delta^{18}O$ (‰,VPDB)	$\delta^{18}O$ SE (‰)	$\delta^{18}O$ fl.[c] (‰,SMOW)	$\delta^{18}O$ fl. SE (‰)	Δ_{47} (‰,I-CDES)	Δ_{47} SE (‰)	Δ_{47} Temp.[d] (°C)	Dolomite Cation Ordering[e] (015:110)	Dolomite Stoichiometry[e] (mole % MgCO$_3$)
Area 1 , Haushi-Huqf outcrop, Oman															
Cretaceous															
SGF37 [f]	Calcite	400	-	3	1.34	0.04	-4.87	0.02	2.08	0.36	0.535	0.008	47	-	-
E37	Dolomite	400	84	3	1.70	0.01	-5.78	0.04	2.00	0.69	0.522	0.009	53	0.45	50.8
I5	Dolomite	400	100	3	-0.04	0.03	-0.31	0.13	6.22	0.97	0.541	0.012	45	0.49	51.0
Area 2 , Central Oman High, subsurface core, Oman															
Permian															
HM-13-1[g]	Calcite	1115	-	2	4.90	0.01	-4.44	0.01	1.37	1.97	0.529	0.024	43	-	-
HM-14-1[g]	Dolomite	1199	-	2	4.88	0.01	-2.55	0.01	0.80	0.41	0.518	0.011	49	-	-
Area 3 , Offshore, subsurface core, Arabian Gulf															
Cretaceous															
Z94708-m[h]	Calcite	2886	-	3	3.14	0.09	-7.04	0.18	4.17	0.86	0.478	0.012	74	-	-
Z94708-sk[h]	Calcite	2886	-	3	3.09	0.10	-6.83	0.05	3.11	0.56	0.494	0.007	66	-	-
Ibrahim484M	Calcite	2950	-	4	3.40	0.20	-6.36	0.05	4.09	0.57	0.488	0.008	69	-	-
Ibrahim484R	Calcite	2950	-	3	3.43	0.03	-7.11	0.07	6.24	0.52	0.452	0.005	89	-	-
Ibrahim6840	Calcite	2950	-	4	2.92	0.04	-4.86	0.06	4.39	0.40	0.504	0.006	61	-	-
Ibrahim708S	Calcite	2950	-	3	3.23	0.03	-8.37	0.08	9.43	0.70	0.400	0.007	125	-	-
Ibrahim652	Dolomite	2943	83	5	4.61	0.16	-6.5	0.09	12.63	1.13	0.387	0.013	136	0.79	51.3
Ibrahim653	Dolomite	2943	91	3	4.85	0.01	-6.33	0.05	14.62	0.60	0.368	0.005	154	0.65	51.0
Area 4 , Wadi Naqab outcrop, Musandam Peninsula															
Jurassic															
WN526	Calcite	5100	0	3	-3.97	0.02	-2.90	0.06	8.37	0.44	0.479	0.005	74	-	-
WN453_Gry	Calcite	5100	0	4	-0.27	0.02	-3.67	0.02	10.71	1.61	0.441	0.019	96	-	-
WN627	Calcite	5100	0	3	2.01	0.05	-3.03	0.06	16.68	1.27	0.382	0.013	141	-	-
WN625_Gry	Calcite	5100	0	4	2.32	0.16	-2.74	0.13	20.36	1.25	0.348	0.013	176	-	-
WN625_Red	Dolomite	5100	31	5	2.30	0.13	-3.99	0.22	16.55	1.20	0.373	0.012	150	0.61	50.2
WN526_Gry	Dolomite	5100	12	4	0.09	0.04	-3.17	0.11	19.81	0.94	0.349	0.008	175	TLTQ	50.7
WN453_Wsk	Calcite	5100	0	3	1.75	0.03	-4.24	0.07	19.33	1.26	0.343	0.012	182	-	-

continue

Sample Information	Mineralogy-FTIR[a]	Depth[b] (m)	% Dolomite XRD	n	$\delta^{13}C$ (‰,VPDB)	$\delta^{13}C$ SE (‰)	$\delta^{18}O$ (‰,VPDB)	$\delta^{18}O$ SE (‰)	$\delta^{18}O$ fl.[c] (‰,SMOW)	$\delta^{18}O$ fl. SE (‰)	Δ_{47} (‰,I-CDES)	Δ_{47} SE (‰)	Δ_{47} Temp.[d] (°C)	Dolomite Cation Ordering[e] (015:110)	Dolomite Stoichiometry[e] (mole % MgCO$_3$)
Area 5, *Jabal Akhdar outcrop, Central Oman Mountain*															
Jurassic															
Mist-2	Calcite	8000	-	3	0.05	0.00	-8.14	0.03	9.82	1.10	0.399	0.012	126	-	-
Mist-6	Calcite	8000	-	3	1.27	0.01	-4.50	0.02	15.74	1.30	0.376	0.014	147	-	-
Mist-5	Dolomite	8000	82	3	0.52	0.03	-5.93	0.09	10.37	0.43	0.418	0.004	112	0.51	49.8
Mist-9	Dolomite	8000	94	3	1.73	0.04	-3.38	0.01	15.27	1.31	0.393	0.014	131	0.40	50.3
Mist-31	Dolomite	8000	46	3	2.03	0.01	-5.34	0.05	16.05	0.45	0.364	0.004	158	0.40	49.7
Mist-8	Dolomite	8000	32	3	1.69	0.02	-7.35	0.11	18.28	1.28	0.323	0.011	208	0.63	50.7
Permian															
MPA11A	Calcite	9000	-	5	2.41	0.02	-6.13	0.07	13.48	1.04	0.382	0.011	141	-	-
MPA11B	Calcite	9000	-	4	3.36	0.31	-7.49	0.51	6.69	3.27	0.442	0.033	95	-	-
WSNE2_C	Calcite	9000	-	4	2.00	0.06	-6.40	0.16	13.02	1.41	0.384	0.014	139	-	-
AK-13	Calcite	9000	-	3	6.04	0.09	-3.35	0.10	19.94	0.05	0.346	0.001	178	-	-
AK-7	Calcite	9000	-	3	5.46	0.01	-2.82	0.02	19.65	0.76	0.354	0.013	169	-	-
MPA35	Dolomite	9000	100	3	6.38	0.03	-0.58	0.05	18.73	0.97	0.387	0.010	136	0.58	51.1
AK-23	Dolomite	9000	100	3	6.08	0.01	-1.06	0.01	24.99	0.67	0.321	0.006	211	0.69	51.1
AK-24	Dolomite	9000	100	3	5.92	0.05	-1.05	0.05	22.10	0.04	0.348	0	176	0.71	51.1
AK-25	Dolomite	9000	100	3	6.02	0.01	-0.02	0.04	26.96	1.65	0.313	0.014	223	0.79	51.6
AK-27	Dolomite	9000	98	3	3.21	0.03	0.38	0.09	22.45	1.29	0.359	0.012	164	0.56	51.2
WBH_25	Dolomite (L)	9000	100	3	5.68	0.03	-6.46	0.06	16.73	0.79	0.346	0.007	178	0.53	50.9
MPA12AG	Dolomite (L)	9000	93	3	3.47	0.08	-7.86	0.15	15.81	2.16	0.341	0.021	184	0.52	50.5
MPA24	Dolomite (L)	9000	88	4	3.49	0.01	-6.24	0.04	15.92	1.63	0.356	0.016	167	0.48	49.8
MPA34	Dolomite (L)	9000	100	4	6.38	0.06	-1.96	0.09	15.28	1.05	0.409	0.012	118	0.57	51.1
WSNE2_M	Dolomite (L)	9000	100	4	3.71	0.02	-4.59	0.07	19.60	1.45	0.337	0.014	189	-	-
WSNE2_WC	Dolomite (L)	9000	100	3	4.31	0.02	-4.51	0.02	24.09	1.35	0.298	0.011	248	0.38	49.4

[a] Fourier-transform infrared spectroscopy mineralogy after Henry et.al. (2017): The late dolomite (L) collected and determined by previous study, Beckert et.al.(2015); Cm = cement.

[b] Estimated maximum burial stratigraphic depth of Jabal Akhdar Central Oman Mountains obtained from Grobe et.al., (2019), distance between Jurassic and Permian sampling location is ~1km; maximum burial depth of Musandam Peninsula obtained from Carminati et.al. (2020) model; Haushi-Huqf burial from Immenhauser et al.(2004) and Sattler et al. (2005).

[c] Calculated diagenetic fluid $\delta^{18}O$ SMOW from calcite $\delta^{18}O$ using Kim and O'Neil (1997) equation.

[d] The calculated temperature from Δ_{47} value using Anderson et.al. (2021) equation.

[e] Analytical procedure of X-ray diffraction following Mancha and Kaczmarek (2021).

[f] Cretaceous calcite sample with maximum temperature record measured by Patel (2019).

[g] Permian samples with maximum temperature record from Bergmann et.al.(2018).

[h] Calcite samples from Adlan and John (2023).
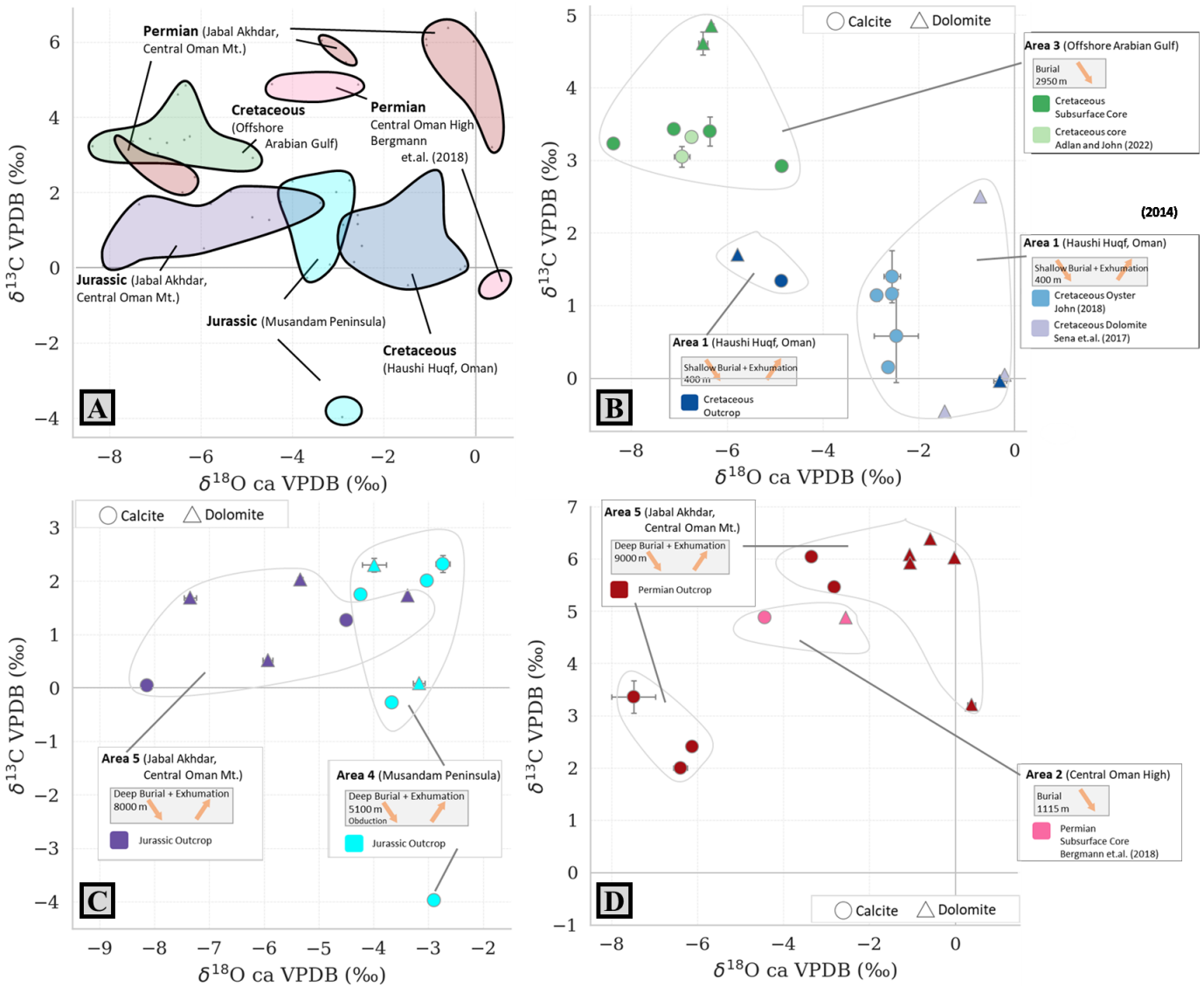
Figures 5.8. Crossplots of $\delta^{18}O$ and $\delta^{13}C$ of each area used in this study. A) Comparison of $\delta^{18}O$ and $\delta^{13}C$ composition including the burial history information on each area. B) Cretaceous samples from an outcrop in Haushi-Huqf and subsurface core in the offshore Arabian Gulf. C) Jurassic samples from an outcrop in the Musandam Peninsula and Jabal Akhdar area, Central Oman Mountains. D) Permian samples from 1115 m depth subsurface core in Oman Central High compared to outcrop in Jabal Akhdar. Data in Oman Central High are obtained from (Bergmann et al., 2018a).

79
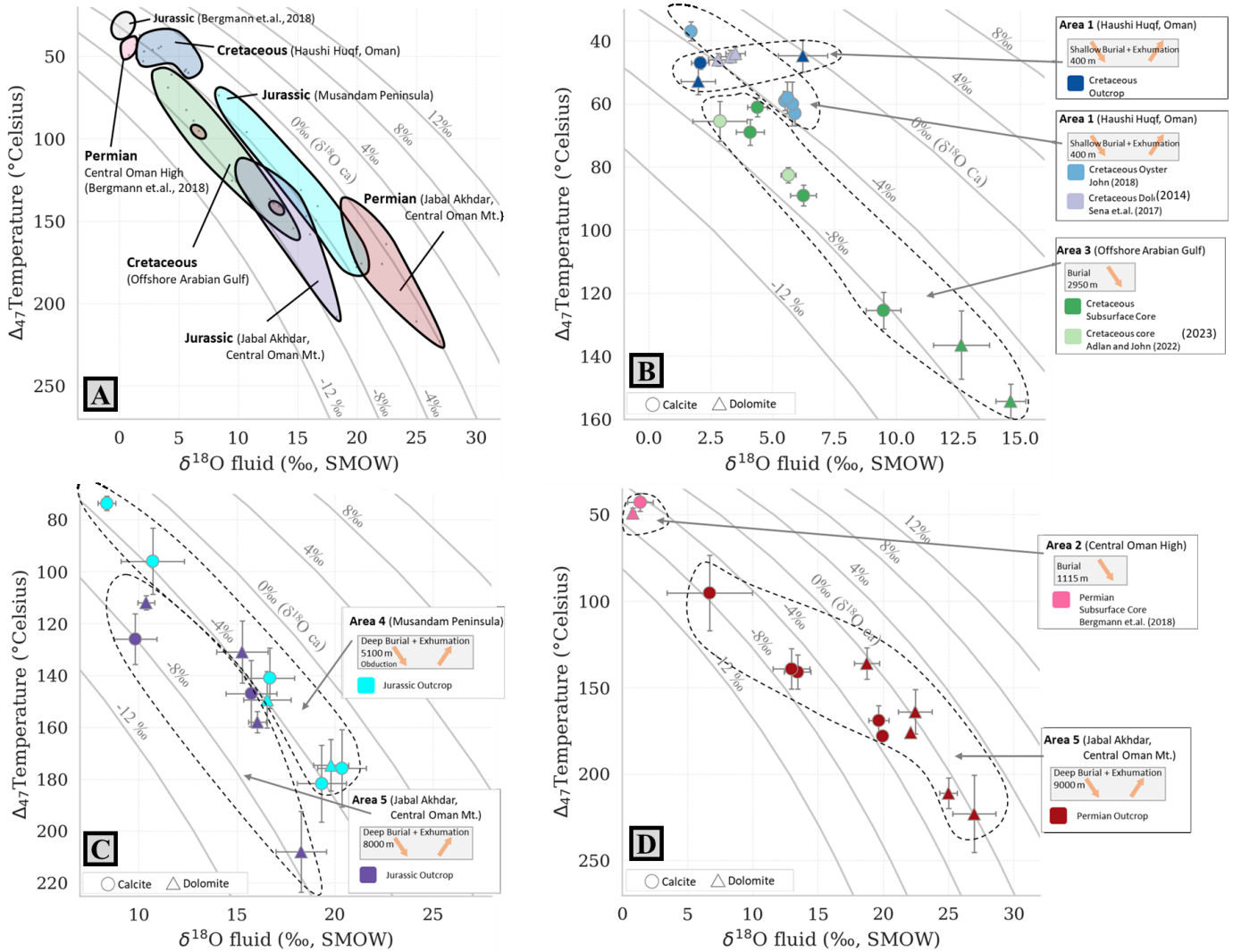
Figure 5.9. The Δ_{47}-temperatures versus the calculated $\delta^{18}O$ values of the diagenetic fluid. Values were reconstructed using the Friedman and O'Neil (1977) equation for calcite and Horita (2014) equation for dolomite. A) Overall data per area, including the burial history information. B) Cretaceous samples from an outcrop in Haushi-Huqf and subsurface core in the offshore Arabian Gulf. C) Jurassic samples from outcrops in the Musandam Peninsula and Jabal Akhdar. D) Permian samples from outcrop in Jabal Akhdar, including Central Oman High data from (Bergmann et al., 2018a).

5.5 Discussion

5.5.1 Evidence of recrystallization

In general, similar typical diagenetic processes were recognized in all areas, including mechanical compaction as evidenced by interlocking crystal contacts (Figure 5.4 B and Figure 5.7 G), replacement of the skeletal fragment materials (Figure 5.4 A), precipitation of non-luminescent calcite and inclusion-rich dolomite (Figure 5.4 A, Figure 5.5.C, Figure 5.6 E, Figure 5.7.G, and Figure 5.7.H), and microfractures (Figure 5.5 C).

A specific recrystallization pattern occurred in Area 3, including evidence of intensive micritization of skeletal grains and the inhomogeneous crystal size of the micrite (Figure 5.4 A). This micrite size variation (crystal enlargement) is consistent with deep burial diagenesis signature (Flügel, 2010) which occurs deeper than 2 km (Immenhauser, 2022). This burial signature has been previously reported in the region by Sirat et al. (2016). Overall, the variation in the morphological features found in the calcite crystals is consistent with the alteration signature caused by burial compaction and cementation (Lambert et al., 2006; Deville de Periere et al., 2011; Alsuwaidi et al., 2021).

For the dolostone in Area 3, the distribution of the fine crystal-micrite (Figure 5.6 E) appears to ignore pre-existing crystal boundaries, and it is consistent with recrystallization (Kırmacı, 2013). Most of the dolomite used in this study consists of fluid inclusion-rich dolomite crystals (Figure 5.6 and Figure 5.7), which is also consistent, with a recrystallization signature (Nielsen et al., 1994; Reinhold, 1998; Kırmacı, 2013). The presence of a range of luminescence in fine-grained textures of both dolomite and calcite is interpreted here as proof of recrystallization, following Scholle and Ulmer-Scholle (2003) and Flügel (2010).

The signature of burial diagenesis in $\delta^{18}O$ was also recognized in some areas. In the Cretaceous, for example, progressively depleted $\delta^{18}O$ values are observed with increasing depth (Figure 5.8 B, Area 1 towards Area 3), an observation consistent with diagenesis during progressive burial (Moore, 1989c; Nelson and Smith, 1996; Al-Mojel et al., 2018). A similar depletion trend was also found in the $\delta^{18}O$ of Jurassic samples towards the area with a deeper burial stage (Figure 5.8 C, Area 4 towards Area 5). This pattern is consistent with temperature-dependent $\delta^{18}O$ fractionation/depletion of both calcite and dolomite at elevated temperatures (Friedman and O'Neil, 1977; Immenhauser, 2022).

5.5.2 Water-rock ratio during recrystallization processes

The $\delta^{18}O$ values of the recrystallized carbonates (Figure 5.8 A) exhibit a decreasing trend associated with temperature elevation, which is consistent with what has been found in previous studies in other

sedimentary basins (Moore and Druckman, 1981; Choquette et al., 1990; Moore and Wade, 2013). In the burial realm or subsurface conditions, the $\delta^{18}O$ of recrystallized minerals is controlled by a temperature-dependent fractionation of oxygen isotopes between mineral and fluid (Anderson and Arthur, 1983; Moore and Wade, 2013). Thus, it is crucial to appreciate the oxygen isotopic composition of the diagenetic fluid ($\delta^{18}O_{fluid}$) to understand the environment in which carbonates precipitated. The nature of fluid-rock interaction is examined by combining Δ_{47} temperature with $\delta^{18}O$ of the minerals to calculate $\delta^{18}O_{fluid}$ using the Kim and O'Neil (1997) equation for calcite and Horita (2014) equation for dolomite (Table 5.2). Fluid-rock interactions and water-rock ratio can be predicted using the stable-isotope exchange trajectories between minerals and fluids (see Chapter 2.4.2). The calculated $\delta^{18}O_{fluid}$ of each sample is plotted against the clumped isotope temperature (TΔ_{47}) to investigate the evolution of diagenetic fluid and interpret fluid-rock interaction involved in the recrystallization process (Figure 5.9 A). The mineral $\delta^{18}O$ composition ($\delta^{18}O_{ca}$) is shown as isolines. The results show that the $\delta^{18}O_{fluid}$ evolves towards heavier composition with increasing temperature, corresponding to a deeper burial regime (Haushi-Huqf area towards Jabal Akhdar area) (Figure 5.9 A). Note on Area 4 and 5, based on the burial history (Figure 5.3 and Table 5.1), the recorded Δ_{47}-temperature are likely to represent a closure/blocking temperature (see Chapter 2.1.3). In this case, fluid-water interaction and water-rock ratio analysis depict stable-isotope exchange trajectories of recrystallization in the cooling period (exhumation).

Area 1 is the shallowest area in this study. The calcite recrystallization patterns in this area are broadly similar to the previous reports on recrystallized oysters with invariant $\delta^{18}O_{ca}$ mineral (John, 2018), suggesting a low water-rock ratio, based on the isotope exchange trajectories between minerals and fluids. However, the wide variability in $\delta^{18}O_{ca}$ of the dolomite at relatively constant temperature suggests near-surface diagenetic influence on the samples.

Towards the deeper areas, the rest of the samples appear to have recrystallized with invariant $\delta^{18}O_{ca}$ compositions with wide temperature evolution (Δ_{47}): In Area 3, the $\delta^{18}O$ values of Cretaceous calcite and dolomite remain remarkably invariant at -6.67‰ ± 0.9‰ with a temperature range from 61°C to 125°C for calcite and a higher temperature range from 136°C to 154°C for dolomite (Figure 5.9 B). In Area 4 and Area 5, the $\delta^{18}O$ values of Jurassic calcite and dolomite were also relatively invariant at -3.39‰ ± 0.5‰ and slightly lower at -5.57‰ ± 1.6‰ in Area 5 (Figure 5.9 C). Interestingly, the $\delta^{18}O$ values of the Permian samples in Area-2 have similarities with the $\delta^{18}O$ values of the Permian sample in Area 5, with invariant calcite $\delta^{18}O$ values at -5.24‰ ± 1.8‰ and the heavier $\delta^{18}O$ for dolomite at -0.47‰ ± 0.5‰ (Figure 5.9 D).

Together with the constant $\delta^{18}O$ values, trends of diagenetic fluid evolution are recognized from all diagrams (Figure 5.9 B-C), from low temperature-low $\delta^{18}O_{fluid}$ to high temperature-high $\delta^{18}O_{fluid}$. Hence, these results are evidence that diagenetic alteration (i.e., recrystallization) of the samples in all areas occurred within low water-rock ratio conditions or rock-buffered systems, where the isotopic composition of carbonate remained relatively invariant through burial and exhumation.

5.5.3 Calcite vs. dolomite temperature

For each location, clumped isotope temperature results are presented for the mean, median, minimum, and maximum measurements of each co-located mineral (Table 5.3). Both the average and maximum clumped isotope temperatures of dolomites are surprisingly higher than calcite across a range of maximum burial depths (Table 5.3), with the exception of the Central Oman High data (Bergmann et al., 2018a) and Musandam Peninsula samples. Note that the similarity between the average temperature of calcite and dolomite in the Central Oman High can be attributed to the dissemination of small rhombohedral dolomite found in the micrite matrix of the Permian limestone (Bergmann et al., 2018a). In the case of the Musandam Peninsula, the similarity between the maximum temperature recorded by dolomite and calcite is attributed to the low (less than 35%) dolomite–calcite ratio found in the dolomite sample, which likely caused by dedolomitization (Figure 5.4). Hence, in both cases, the mineralogy of one of the end members is questionable and discarded from the discussion below.
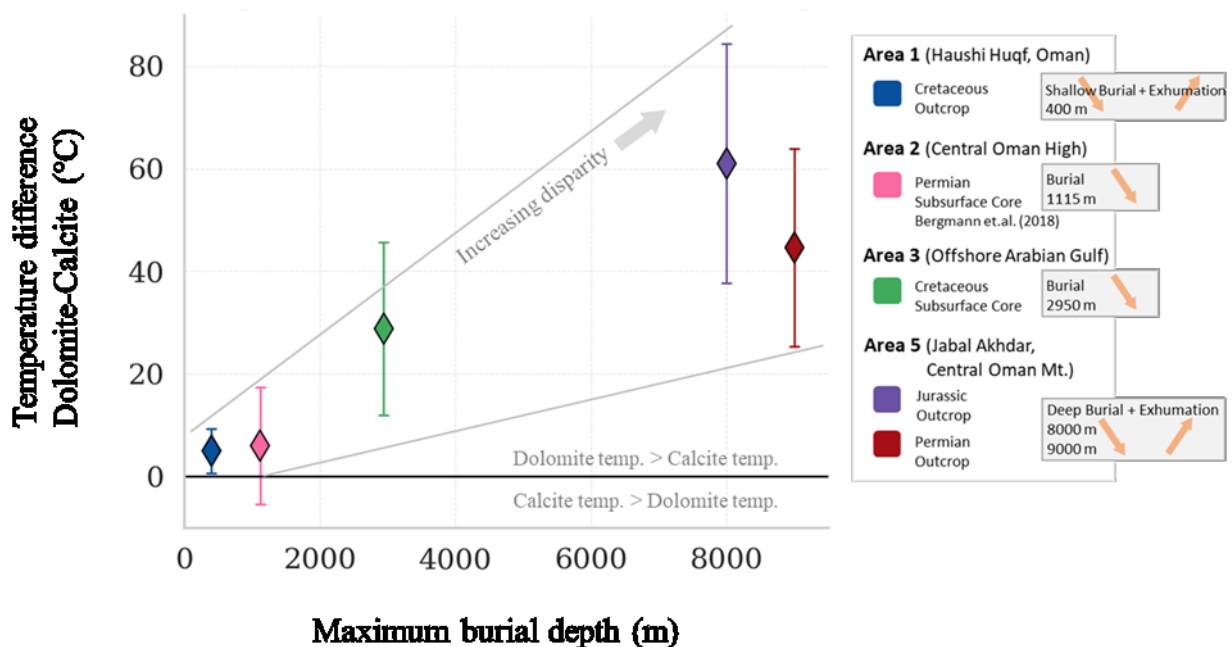
Figure 5.10. Difference between maximum Δ_{47}-temperature recorded in dolomite and calcite with respect to its maximum burial reached (see Table 5.1 and Figure 5.3). From left to right, Area 1 to

Area 5. The disparity between temperatures recorded in both minerals increases as the rock formation is buried deeper.

Considering the regional burial history, the difference between the maximum temperature recorded in Cretaceous dolomite and calcite in Haushi-Huqf (buried 400 m) is insignificant (5°C, with 1SE = 4°C). The temperature disparity becomes wider with increasing maximum burial estimates of the samples, forming a noticeable trend toward an increasing temperature regime (Figure 5.10). The difference between the maximum temperature recorded in Cretaceous dolomite and calcite offshore in the Arabian Gulf is 29±17°C. The disparity between temperatures recorded in both minerals increases significantly in Jurassic rock in Jabal Akhdar (61±23°C) and in Permian rock of the Jabal Akhdar (45±19°C). These results provide evidence from natural samples that calcite and dolomite have different properties during recrystallization that could result in the recording of different clumped isotope signatures despite the same thermal history. This is consistent with lab experiments showing that different carbonate minerals have different C-O bond reordering kinetics, i.e., they have different Arrhenius parameters and variations in frequency factor (Lloyd et al., 2017; Lloyd et al., 2018; Hemingway and Henkes, 2021). As the minerals experience substantial burial heating (>100°C; Immenhauser, 2022), the kinetic difference will result in a greater impact on recorded temperature depending on the cooling rates.

Table 5.3. The Δ_{47}-temperature information of dolomite and calcite samples in each area, the maximum burial reached, and the temperature disparity between dolomite and calcite.

Sample Information	Depth[a] (m)	G.Geo. Temp.[b] (°C)	Δ_{47} Temp. [c] (°C)						$\Delta\Delta_{47}$Temp. [d] (°C) |Dol. - Cal.|	S.E. Temp. |Dol. - Cal.|
			n	Mean	S.E.	Median	Min	Max		
Area 1, *Haushi-Huqf outcrop, Oman*										
Cretaceous									5	4
Calcite [e]	400	47.5	24	34	4	35	21	47		
Dolomite [f]	400	47.5	5	47	2	45	44	53		
Area 2, *Central Oman High, subsurface core, Oman*										
Permian									6	11
Calcite [g]	1115	55.3	18	36	3	35	30	43		
Dolomite [g]	1199	56.3	3	36	11	33	28	49		
Area 3, *Offshore, subsurface core, Arabian Gulf*										
Cretaceous									29	17
Calcite	2950	130.0	4	86	14	79	61	126		
Dolomite	2943	130.0	2	145	9	145	136	154		
Area 4, *Wadi Naqab outcrop, Musandam Peninsula*										
Jurassic									-1	26
Calcite	5100	168.4	4	122	23	118	74	176		
Dolomite	5100	168.4	2	162	13	162	149	175		
Area 5, *Jabal Akhdar outcrop, Central Oman Mounta*										
Jurassic									61	23
Calcite	8000	169.3	2	137	11	137	126	147		
Dolomite	8000	169.3	4	152	21	145	112	208		
Permian									45	19
Calcite	9000	187	5	145	14	141	95	178		
Dolomite	9000	187	6	181	13	177	136	223		

[a] The maximum burial stratigraphic depth of Jabal Akhdar Central Oman Mountains obtained from Grobe et.al., (2019), distance between Jurassic and Permian sampling location is ~1km; The maximum burial depth of Musandam Peninsula obtained from Carminati et.al. (2020) model; Haushi-Huqf burial from Immenhauser et al.(2004) and Sattler et al. (2005).

[b] Expected temperature of the samples on given depth: the geothermal gradient for Haushi-Huqf and Oman Central High area were obtained from Bergmann et.al. (2018), the offshore-Arabian Gulf area from Ehrenberg et.al. (2020), Musandam Peninsula area from Ali et.al. (2017) Tibat-1ST well and Oman Mountain from Schütz et.al. (2018) NB-22 well.

[c] The calculated temperature from Δ_{47} value using Anderson et.al. (2021) equation.

[d] Difference (disparity) between max. clumped isotope temperature recorded on dolomite and calcite.

[e] including clumped isotope results of calcite sample measured by Patel (2019).

[f] including clumped isotope results of dolomite measured by Sena et.al. (2014).

[g] Permian interval data collected from HM well by Bergmann et.al.(2018).

5.5.4 Modeling applications

5.5.4.1 Offshore Arabian Gulf

In the Arabian Gulf area, calcites from the Cretaceous interval sit on the geothermal gradient temperature (Table 5.3). The maximum clumped isotope temperature recorded by calcite (126°C) is less than 1SE away from the current geothermal temperature (Ehrenberg et al., 2020) at the sampling point (130°C, Table 5.3). These results could be used to suggest that this calcite recorded the maximum burial depth, and only underwent burial (no exhumation). However, the maximum clumped isotope

temperatures recorded in dolomite in the same interval (7 m vertical difference) are not consistent with the formation temperature (136-154˚C), i.e. are from 6-24°C higher, suggesting the possibility of higher temperature history pre-dating the current conditions. The recalculated $\delta^{18}O_{fluid}$ values show that all of samples are formed in low water-rock ratios, fitting the isotope-exchange reactions via solid-state clumped isotope bond reordering (Dennis and Schrag, 2010; Passey and Henkes, 2012; Stolper and Eiler, 2015; Lloyd et al., 2018; Brenner et al., 2018). Thus, it is ideal for the forward modeling test. The model calculations predict the Δ_{47} development at sequential time steps of the imposed temperature-time (T-t) histories.
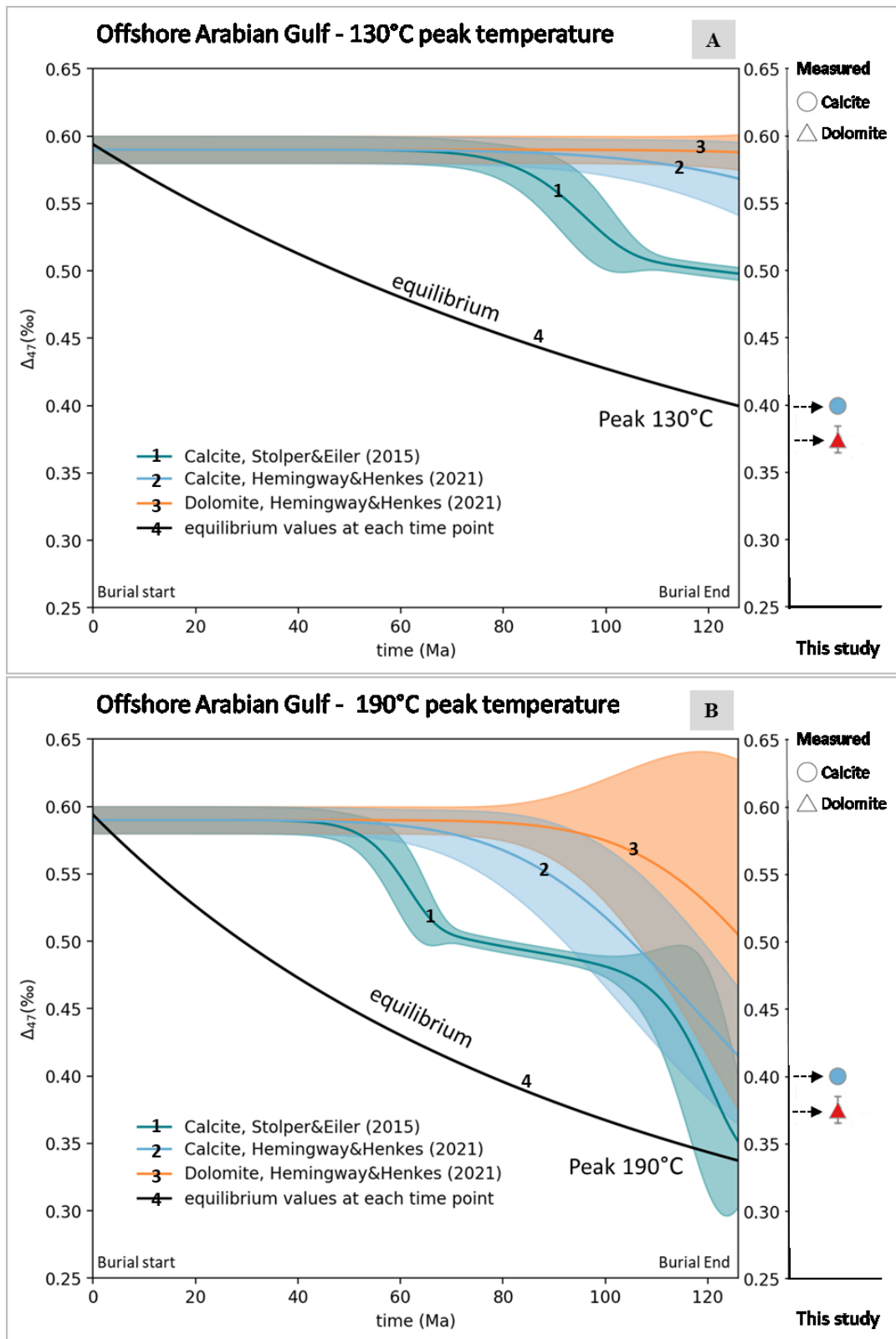
Figure 5.11 Result of the forward model of Δ_{47} development (A) with peak burial at present-day formation temperature of 130°C, where the prediction and actual clumped isotope temperature is inaccurate. Forward model (B) with a peak burial scenario of 190°C, where the model hardly fits the prediction. Colored bands around the lines are the uncertainty bounds of the mineral model. The equilibrium line represents the increase in the burial-heating temperature of the rock.

87

Using two different vets of kinetic parameters for the calcite and one kinetic model for dolomite, the first forward model result shows that the solid-state reordering model during progressive burial offshore in the Arabian Gulf is unlikely and does not fit the measured maximum temperature recorded in both calcite and dolomite (Figure 5.11 A). In this model (peak 130°C with 0.81 °C/Ma heating rate), the dolomite retained its initial Δ_{47} but calcite did not. The unaffected dolomite Δ_{47} is expected as previous studies suggest that the rates of solid-state clumped isotope reordering are slower in dolomite than in calcite (Eiler, 2011; Ferry et al., 2011; Ryb et al., 2017; Lloyd et al., 2017). This model demonstrates that solid-state reordering by itself is unable to bring both minerals to their present-day equilibrium temperature.

In order to reproduce the measured temperature of the samples, the peak temperature of the solid-state reordering heating model needs to be adjusted to 190°C with a 1.32 °C/Ma heating rate (Figure 5.11 B). In this case, the calcite mineral temperature prediction appeared to fit with the calibration, but the actual dolomite temperature is at the very end of the wide error range for dolomite prediction (Figure 5.11 B). Based on the disordered kinetic model equation (Hemingway and Henkes, 2021), the predicted calcite mineral reached 0.416 ± 0.050‰ (1SE) in Δ_{47} value compared to the actual maximum temperature record of 0.400 ± 0.007‰ (1SE), while the predicted dolomite mineral reached 0.502 ± 0.133‰ (1SE) in Δ_{47} value compared to the actual maximum temperature record of 0.368 ± 0.005‰ (1SE). The predicted calcite using the paired-diffusion model equation reached 0.353‰± 0.053‰ (1SE). All and all, the calcite mineral temperature prediction appeared to fit with the calibration considering the standard error margin (1SE), while the measured dolomite Δ_{47} temperature is at the very end of the wide error range for dolomite prediction (Figure 9 B).

Using the adjusted 190°C-peak model instead of the 130°C-peak model, one can argue that the Cretaceous interval in the offshore Arabian Gulf was likely buried ~1750 m deeper than its present-day depth to approximately 4700 m. In this case, the dolomite records 154°C temperature and retains it, while the calcite cooled down to the present-day formation temperature of 126°C. However, published burial histories in this area revealed no exhumation more significant than 200 m (Ehrenberg et al., 2020), meaning the Cretaceous interval is likely buried only ~200 m deeper than its present-day depth.

The modelling results here suggest that the solid-state reordering process by itself was unable to explain the current mineral temperature records, it is reasonable to postulate that both minerals must have been recrystallized progressively through burial. In this case, there are two ways to interpret the difference between calcite and dolomite temperature records:

First, it is possible that the calcite in this interval records current ambient temperature, while the dolomite records the older ambient temperature when the gradient geothermal was higher. In this case, the temperature disparity between dolomite and calcite is a function of cooling via a change in the geothermal gradient. It is suggested that the rifting phase in this sedimentary basin was associated with an instantaneous increase in heat flow in response to thinning of the lithosphere (McKenzie, 1978; Waples, 2001). Other studies, however, suggested a delay in the pulse of the heat flow after the rift has been initiated (Morgan, 1983; Wheildon et al., 1994; Waples, 2001). Given that heat flow is a function of the geothermal gradient and thermal conductivity, one can argue that the geothermal gradient in the area used to be higher than what is recorded in the dolomite.

Second, considering the minimum temperature difference of 6°C (between the coolest dolomite record in the samples and formation temperature), it is reasonable to suggest that the formation has been uplifted by 200 m (6°C difference) minimum. In this case, the difference in calcite and dolomite temperature is a function of tectonic uplift, and the maximum burial temperature is retained by dolomite. Either way, the data suggest that the temperature of this Barremian-Aptian interval of Kharaib Formation used to be higher historically compared to the present-day conditions.

5.5.4.2 Jabal Akhdar, Central Oman Mountains

In the Jabal Akhdar, a previous burial history model showed that the maximum burial depth reached by the Jurassic strata was ~8 km (Grobe et al., 2019). The post-compaction stratigraphic thickness between the Jurassic and the Permian samples is ~1 km; thus, suggesting that the maximum burial depth reached by the Permian sample was ~9 km. Using information from the geothermal gradient from well NB-22 (Schütz et al., 2018), the Jurassic sample should have reached 169°C at a maximum burial depth of 8 km, while the Permian sample reached 187°C at 9 km (Table 5.3). Interestingly, the clumped isotope measurement shows that the maximum temperature recorded by Jurassic calcite is 147°C±12°, similar to the predicted temperature at 8 km considering 1SE of the measurement (Table 5.3). The maximum temperature recorded by Permian calcite is 178±8°C, also similar to the estimated temperature at 9 km (Table 5.3). Coeval with the calcite, however, the maximum Δ_{47} temperature recorded by the dolomite in the Jurassic interval is higher (208±15°C), while the dolomite in the Permian interval recorded 223±22°C.

The clumped isotopes measured in the calcite and dolomite in Jabal Akhdar are not a reflection of the maximum burial temperature but a depiction of the 'blocking temperature' or 'apparent equilibrium temperature', which are sensitive only to the rate of cooling (Passey and Henkes, 2012; Stolper and Eiler, 2015; Ryb et al., 2017) (see Chapter 2). Therefore, the maximum burial temperature reached by

the Jurassic and Permian intervals should be higher (deeper burial). To test this, the exhumation model was created (Figure 5.12). The final predicted Δ_{47} values in the present day can then be directly compared to the measured Δ_{47} of the samples.

The exhumation model results show that the blocking temperature reached during the cooling/uplift event in Jabal Akhdar fits the measured maximum $\Delta47$ temperature for both calcite and dolomite (Figure 5.12). To achieve this result, an initial peak temperature of 280°C (Δ_{47}=0.277‰) with a cooling rate of 3.18°C /Ma for calcite and dolomite was required. Only at this peak temperature, the end result of the calcite mineral model reached a Δ_{47} of 0.350 ± 0.020‰ (1SE) matching the actual (clumped isotope) measurement record of 0.346 ± 0.001‰ (1SE). Likewise, the dolomite mineral model reached a Δ_{47} of 0.325 ± 0.031‰ (1SE) matching the actual measurement record of 0.313 ± 0.014‰ (1SE).

These results contradict previous studies from illite–smectite analysis in the Jabal Akhdar by Aldega et al. (2017), who argued for peak temperatures of 150–200°C on the northern flank and 120–150°C on the southern flank of Jabal Akhdar. However, this study predicted peak temperature of 280°C, which is in accordance with findings reported by a zircon fission track study in the pre-Permian basement indicating peak temperatures up to 280°C (Saddiqi et al., 2006) and a Raman spectroscopy study on carbonaceous material indicating peak burial temperatures of 266 to 300°C for the entire Jabal Akhdar (Grobe et al., 2016; Grobe et al., 2019). The modelling results here demonstrates the benefits of reconstructing thermal history using co-occurring calcite and early dolomite.

Jabal Akhdar, Central Oman Mountains
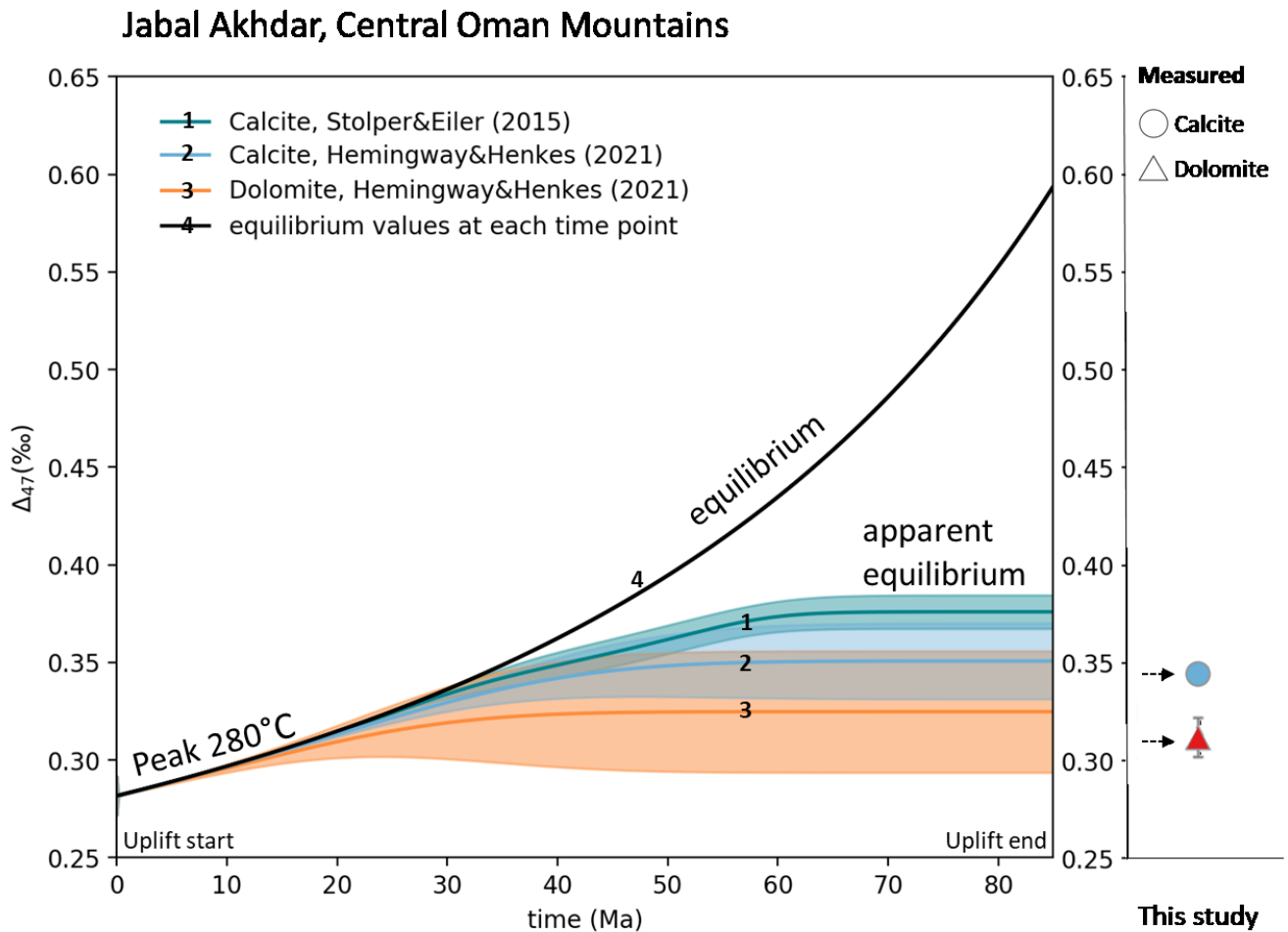
Figure 5.12. Results of the forward model of Δ_{47} development from peak burial 280°C cooled down to 25°C. Using the Hemingway and Henkes (2021) model, the prediction fits the actual clumped isotope temperature. Colored bands around the lines are the uncertainty bounds of the mineral model. The equilibrium line represents the cooling temperature (in Δ_{47}) of the rock in the exhumation process.

5.5.5 Effect of temperature on dolomite mineralogy

The mineralogy of dolomite has been used as a potential proxy to investigate the diagenetic environment (Reeder, 2000; Jones et al., 2001; Kaczmarek and Sibley, 2007, 2011; Manche and Kaczmarek, 2019). One of the fundamental parameters for this investigation is cation ordering, which refers to the degree to which Mg and Ca cations are distributed in their cation layers in the dolomite lattice (Reeder and Wenk, 1983; Kaczmarek and Thornton, 2017).

A previous study suggested that cation ordering develops faster at higher temperatures (Kaczmarek and Thornton, 2017). In this study, the early dolomite with a higher blocking temperature has a higher cation ordering compared to the early dolomites recording lower temperatures (Figure 5.13 A). In both intervals, the lower blocking temperature corresponds to lower cation ordering. Hence, this study

91

confirm that the progressive development of cation ordering is driven by temperature elevation, as previously suggested (Kaczmarek and Thornton, 2017).
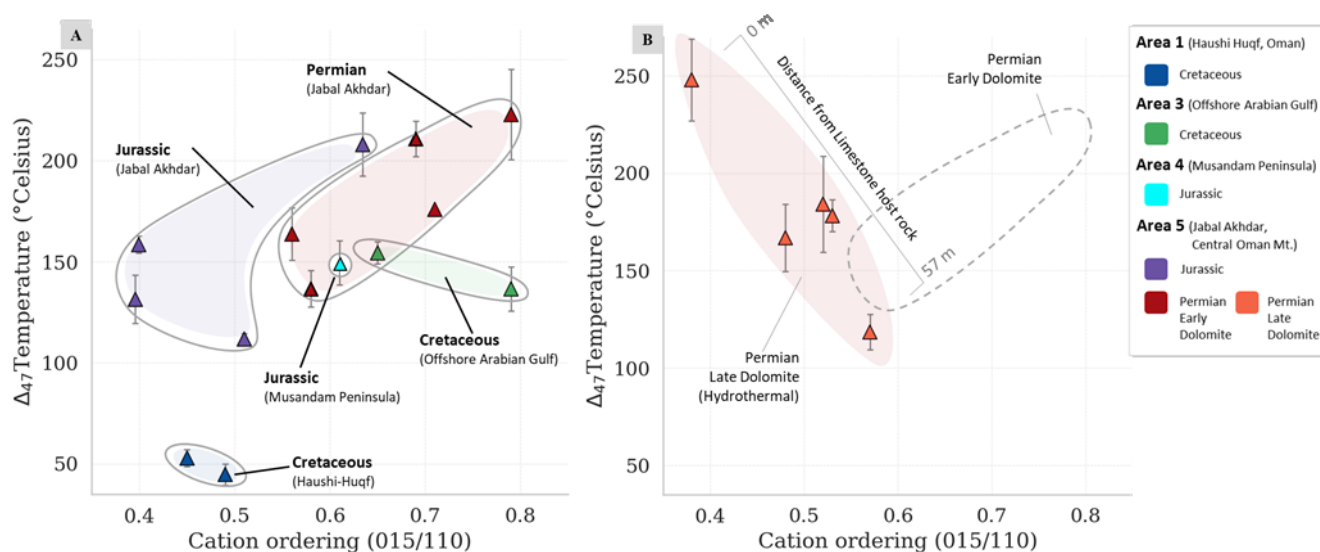
Figure 5.13. Dolomite [015]:[110] cation ordering and Δ_{47}-temperature relationship. A) Overall, high temperature (low Δ_{47}) dolomite corresponds to well-ordered cations. B) In contrast, the hydrothermal dolomite in Jabal Akhdar records a low value of cation ordering (poor-ordered cation) at high temperatures.

The late hydrothermal dolomite in Jabal Akhdar shows that the higher temperature dolomite corresponds to poorly ordered cations (Figure 5.13 B). This result is the reverse of the trends seen in the recrystallized early dolomite. The late dolomite in this area was emplaced along the Precambrian–Permian unconformity and up through the well-bedded limestone and early dolomite host rock during the exhumation event (Beckert et al., 2015). It is possible to explain the pattern observed by distance from the source of the hot fluids: cation ordering of the late dolomite decreases away from the initial limestone host rock, and increases closer to where the early dolomite host rock was replaced by late dolomite. In this case, the temperature variability corresponds to the flow direction of dolomite emplacement penetrating the lower limestone bed (higher temperature) towards the upper early dolomite bed (lower temperature). The result here is in accordance with findings reported by Von Der Borch and Jones (1976), Carballo et al. (1987), Rosen et al. (1988), and Perkins et al. (1994), indicating that Ca-rich dolomite (limestone replacement) corresponds to poorly ordered cations.

5.6 Conclusion

This study demonstrate that natural calcite and early dolomite record different clumped isotope values when subjected to the same thermal history. The calcite and dolomite used were collected from fine-grained carbonate rocks recrystallized at a low water-rock ratio, based on the stable-isotope exchange trajectories between minerals and fluids. The maximum clumped isotope temperature recorded in early dolomite found in this study is higher than for co-located calcite. This disparity is related to the difference in the kinetic parameters between the two minerals, and it appears to systematically increase as the rock formation is buried deeper. This systematic temperature difference confirms the laboratory experiments suggesting that the dolomite Δ_{47} records are more resistant to alteration during burial and exhumation (Hemingway and Henkes, 2021).

Calcite is the main mineral used in carbonate clumped isotope studies to reconstruct burial history. This study shows that clumped isotope temperature records of calcite in subsurface formation can appear to be in line with the gradient geothermal temperature, yet they not convey the whole geological story. In this study, both calcite and dolomite forward modelling in the subsurface formation are capable to detect an uplift event (i.e. offshore Arabian Gulf). In the exhumed area, both mineral records are able to predict the peak temperature reached by the formation (i.e., Jabal Akhdar). This study demonstrates how to identify more geological phenomena while reconstructing thermal history using two different but very common minerals: calcite and early dolomite at the same sampling point. This study confirm that dolomite has a higher closing temperature during cooling and offers additional constraints on the burial model.

Mineralogy investigation on the early dolomite confirms that the progressive development of cation ordering is driven by temperature elevation, as previously suggested by Kaczmarek and Thornton (2017). The early dolomite with a higher blocking temperature exhibits greater cation ordering than the lower temperature dolomite. A comparison with hydrothermal dolomite reveals that this relationship is reversed potentially due to the calcium content of the dolomite (Ca-rich dolomite). This study demonstrates that cation ordering and temperature development in late dolomite is likely to be related to the source of hydrothermal flow direction, as the dolomite emplacement penetrating the lower limestone bed (higher temperature) results in lower cation ordering, then continue towards the upper early dolomite bed (lower temperature) which results in high cation ordering.

CHAPTER 6

CONCLUSIONS AND FUTURE RESEARCH DIRECTIONS

6.1   Conclusions

The carbonate clumped isotope thermometer is one of the most effective tools for thermal history reconstruction in sedimentary basins, not only for carbonate formations at the shallow stage of burial but also in deeper stage burial through exhumation. Considering the unique nature of carbonate minerals (i.e., mineral reactivity and inclination to recrystallization), this technique allows us to understand the relationship between the recrystallization process in various tectonic settings and its post-depositional isotopic alteration of Δ_{47} signature, the $\delta^{18}O$ and $\delta^{13}C$. Community efforts to understand the thermal evolution of carbonate minerals via controlled laboratory experiments have been demonstrated to be applicable in carbonate rocks at various stages of the burial process across a regional orogeny.

The thesis aims were to investigate the robustness of clumped isotope thermometers to archive thermal history in recrystallized carbonates and to add more constraints on the thermal history reconstruction process using more mineral types. This is achieved through Chapters 3, 4 and 5 of the thesis, summarised in the following paragraphs. The rock specimens used for the clumped isotope's thermal history reconstruction can be sourced from both the outcrop specimens and subsurface cores with various degrees of contamination. In order to ensure the precision of carbonate clumped isotope measurement, the study first focused on methodological development, particularly on hydrocarbon contamination removal (1). Following this, the thermal history reconstructions of recrystallized carbonates in the natural laboratory were conducted from the shallowly buried rock formation (2) to the deeper stage, including the exhumation history (3). Detailed findings are outlined below.

Finding 1: Impact and effectiveness of Oxygen Plasma Ashing treatment and recommendations for safe sample treatment.

The isotopic measurement on hydrocarbon-rich samples, such as oil-stained carbonates, bituminous shales, or very high organic carbon content host rocks, can cause a problem in the Δ_{47}, $\delta^{18}O$ and $\delta^{13}C$ signals beyond the silver-trap capability. The molecular gaseous species produced by the reaction of organic components and phosphoric acid have similar molecular weights to the carbon dioxide molecules and bring isobaric effects that interfere with the mass spectrometric determination. Meanwhile, any effective treatment to remove organic material prior to carbonate clumped isotope analysis must maintain the original (initial) isotopic composition of the mineral while removing contaminants. This thesis shows that 30 minutes or more of oxygen plasma ashing on calcite powders

has the potential to alter the initial isotopic composition beyond analytical error, thus biasing paleo-temperature studies. It is postulated that this alteration occurs because the bonds between the lighter isotopes are preferentially broken by oxygen plasma ashing treatment, leading to an increase in the 'clumping' of the sample. The recommendation from this thesis is that any laboratory performing OPA should shorten the runs to 10 to 20 minutes, as plasma treatment of this duration here shows no alteration of the initial value of $\Delta_{47.}$ In addition, it is possible to safely remove additional organic matter by doing successive runs of 10 minutes, followed by a break and stirring of the sample.

Finding 2: Recrystallization and clumped isotope-thermal resetting of different limestone components.

The burial diagenesis on each carbonate fabric is controlled by the mineral-surface area available for reaction, the saturation state of diagenetic fluids, and the thermodynamic stability of the carbonate minerals being dissolved or precipitated. It is found that different carbonate fabrics recrystallize at different water-–rock ratios and with different susceptibility to thermal reset with respect to clumped isotopes. The finer-grained matrix continues to recrystallize even at a low water–rock ratio during the deeper burial history and records a wide range of temperatures, suggesting continuous recrystallization. In the case of the Barremian limestone interval, recrystallization continued between 90 and 50 Ma based on established thermal histories. The evidence that the process of dissolution and re-precipitation reactions in the study interval were stopped by oil emplacement is also found. The argument of whether oil emplacement retards diagenesis (cementation) has been debated, and this findings potentially provide a conclusive element to this debate in carbonate systems. At the same time, this study also extends the application of clumped isotope analyses to petroleum migration studies.

Finding 3: Kinetic differences between minerals in recrystallized limestone and dolostone for additional constraints in thermal history reconstruction.

Post-depositional alteration of the Δ_{47} isotope signature from the effects of burial–exhumation, including recrystallization, can be challenging, particularly 'solid-state reordering'. Here, the behaviour of clumped isotope-exchange reactions through burial complexity using a natural laboratory were studied, because the diagenetic complexity of ancient carbonates is difficult to replicate in the laboratory. The results show that natural calcite and early dolomite record different clumped isotope values when subjected to the same thermal history. The maximum clumped isotope temperature recorded in early dolomite found in this study is higher than for co-located calcite, which corresponds to the difference in the kinetic parameters between the two minerals. It is confirmed that the dolomite Δ_{47} records are more resistant to alteration during burial and exhumation. This study shows that the dolomite has a higher closing temperature during cooling and offers additional constraints on the burial model.

From the mineralogy investigation of dolomite, it is also found that the early dolomite's cation ordering is driven by temperature elevation. A comparison with hydrothermal dolomite reveals that this relationship is reversed. Here in the case study, It is demonstrated that cation ordering and temperature development in late dolomite is related to the source of hydrothermal flow direction.

6.2 Wider implications

There are five broader implications of this thesis, organised as follows:

1. The sample treatment for organic contaminant removal prior to isotopic analysis and radiocarbon dating has become standard practice. The result of the cleaning protocol in Chapter 3 of this thesis not only helps the application of isotopes measurement in challenging samples (i.e., oil-stained carbonates, bituminous shales, or very high organic carbon content host rocks) but also to improves the accuracy of paleoclimate study via isotopic analysis, that often use fluid based (NaOCl or H_2O_2) pre-treatment for organic contaminant removal which potentially mask or alter the original isotopic composition of the samples. The samples used for the paleoclimate study were often collected from the sea floor and its thick layer of sediment. Scientists use this accumulated sediment as a timeline to study paleoclimate, as each layer within the sediment may hold fossils of the tiny plants and animals that dominate the ocean and grains of dust and minerals that can tell about climate patterns. The cleaning protocol using OPA can be used as a standard method to clean the organic contaminant found in the sediment prior to isotope measurement, thus improving the accuracy of the isotope-paleoclimate study.

2. The topic of carbonate diagenesis is of fundamental importance to the academic domain and industry in the evaluation of hydrocarbon reservoir rocks. This thesis demonstrates that different carbonate fabrics recrystallize at different water-rock ratios as the water-rock interaction between fabrics diverges. Therefore, for a diagenesis study, examination of whole fabrics in the sample should be performed routinely, as it can decipher diagenetic events in more detail (e.g. cementation stoppage, Chapter 4) beyond what is typically obtained from bulk carbonate rocks. This method will help researchers unravel diagenetic events comprehensively.

3. Dolomite can form a primary precipitate in seawater, early diagenesis or a late burial diagenetic phase. Because of these multiple origins, the study of the kinetic of dolomite for clumped isotope-solid state reordering is less than that of calcite minerals. This thesis demonstrates that combining dolomite's cation ordering and clumped isotope analysis can help researchers understand new geological phenomena (e.g. the flow direction of dolomite emplacement,

Chapter 5.5.5). Thus, examining both cation ordering and clumped isotope shall be performed routinely, so that researchers can investigate the dolomite diagenesis and origin confidently.

4. This thesis demonstrates that clumped isotope paleothermometry on multiple fabrics in carbonate samples is necessary and should be used as a standard procedure for petroleum system analysis in hydrocarbon exploration. In the future, this approach will help determine the timing of oil migration in carbonate rocks when another alternative (i.e. fluid inclusion) is inaccessible.

5. Lastly, application on both calcite and dolomite for burial history analysis (Chapter 5) can be integrated into the basin modelling process as it can help build a better burial model and leads to the detection of new geological event. For example, the clumped isotope measurement may provide temperature history in carbonate-dominated source rock, including the maximum temperature information as alternative to Tmax from Rock-Eval pyrolysis. As a broader application, clumped isotope measurement results can be integrated into basin modelling software for thermal modelling calibration, thus improving the basin modelling effectiveness, especially when the standard calibration is unavailable (e.g. vitrinite, organic biomarkers).

6.3   Future research directions

Further investigations following on from this research may be usefully focused on (1) published work on clumped isotope that involves excessive time for plasma treatment, (2) challenge of clumped isotope measurement on micro fabrics with 2mm or less in sizes, (3) laboratory heating experiments for early dolomite to obtain variability of solid-state reordering kinetics that can be used for model prediction improvement, (4) whether the study of the timing of oil migration can be applied to other fields including its migration pathway and (5) understanding the relationship between mineralogy attributes of dolomite (cation ordering and stoichiometric) and the kinetic difference for a potential new proxy to understand dolomite replacement process. The detailed explanation is as follows:

1) Published work on clumped isotopes that involves excessive time for plasma treatment needs to be examined, as the value of clumped isotopes might be higher than the actual value (Chapter 4), translated to a lower (underestimation) clumped isotope temperature. However, correcting this value might be done carefully because different instruments might yield different effects due to different parameters such as power rate, which determines the radio frequency (RF), the working temperature inside the plasma chamber and its pressure chamber parameter. Thus, the degree of organic contaminant removal, including its potential alteration, might differ. Therefore, further examination of the effect of the OPA instrument with higher power (higher

RF) will be beneficial and worth checking. The next stage of investigation is to check whether the alteration by OPA will be significantly more extensive beyond 30 minutes of plasma exposure time.

2) The mass spectrometry used for clumped isotope measurement in this thesis requires 4 to 4.5mg of carbonate material for a single measurement (one replicate). The traditional Kiel device method, such as the dual inlet approach (Petersen and Schrag, 2014), has been used to achieve this weight requirement. Using the dual inlet method, other clumped isotope laboratories also require between 4 and 15mg carbonate material per replicate, limiting the possible applications of clumped isotope on smaller carbonate fabrics (<2mm), as it is challenging to acquire enough sample material for replicate analysis due to their small size. One of the options is to use a technique known as LIDI (long-integration dual-inlet), which reduces the 'wasted' gas remaining in the bellows and the sample vial, allowing the researcher to use fewer materials. Future research should focus on maximising the efficiency of this LIDI technique so that clumped isotopes can be measured with carbonate materials of ~3 mg or less. Improving the LIDI technique may open new avenues of research in the thermal history of rocks, diagenesis of carbonates, paleoceanography, palaeoclimatology and other current sample-size limited applications.

3) The results and discussions in this thesis have drawn attention to the kinetic parameters of solid-state reordering in dolomite minerals, including their cation ordering and stoichiometry. Kinetics studies through controlled heating experiments have mostly been conducted on calcite as opposed to dolomite (Passey and Henkes, 2012; Henkes et al., 2014; Stolper and Eiler, 2015; Brenner et al., 2018). So far, there has been only one dolomite heating experiment performed by Lloyd et al. (2018). A recent study shows that it is possible to create a new kinetic framework using multiple laboratory results of heating experiments, as recently demonstrated by Hemingway and Henkes (2021). This study used 42 data experiments with calcite as the majority mineral. As demonstrated by Hemingway and Henkes (2021), compiling experimental data results from the laboratory can help create a new kinetic framework and thus improve future model predictions of burial-thermal reconstruction. Thus, more heating experiments in dolomite should be performed.

4) The Oman-United Arab Emirates (UAE) carbonate reservoir is the most intensely studied reservoir rocks on earth. This thesis used a carbonate reservoir in UAE to study diagenetic cessation in carbonate rocks that led to a new application of clumped isotope to predict the timing of oil migration (Chapter 3). This analysis may now be confidently performed in the carbonate reservoir in the surrounding UAE area, which has a similar tectonic history. In the future, it is necessary to see the same approach performed on different oil fields in different

tectonic settings (i.e. Indonesia region) to confirm the clumped isotope technique's effectiveness in predicting oil migration. Future research needs to involve more wells data. The technique in Chapter 3 may also be developed further to predict the oil migration pathway, using samples below oil-water contact surrounding the oil field: If the recorded clumped isotope surrounding area is not similar (suggesting inhibition of cementation), it should be possible to pinpoint the migration pathway of oil.

5) Following the dolomite cation ordering results in Chapter 5, it is found that the progressive development of cation ordering is driven by the temperature elevation. This study shows that cation ordering is connected to the final $\Delta 47$-blocking temperature of minerals. Thus, it is important to examine the possibility of using cation ordering as an additional constraint for thermal history reconstruction in the future. In this thesis, the cation ordering and temperature development in late dolomite can be used to examine the source of the hydrothermal flow direction. Further laboratory experiments may be required focusing on the cation ordering behaviour in different types of dolomite. This experiment will be beneficial and worth investigating as it helps to create a new proxy to understand the process of dolomite replacement.

REFERENCES

Aase, N.E., Bjørkum, P.A. and Nadeau, P.H. (1996) The Effect of Grain-Coating Microquartz on Preservation of Reservoir Porosity1. AAPG Bulletin 80, 1654-1673. 10.1306/64EDA0F0-1724-11D7-8645000102C1865D.

Abd-Allah, A.M.A., Hashem, W.A. and Abdelghany, O. (2009) Post-obduction deformations of the northwestern end of the Hatta Shear Zone, El Rawdah area, Northern Oman Mountains. Math Comput Sci Eng, 79-90.

Adlan, Q., Davies, A.J. and John, C.M. (2020) Effects of oxygen plasma ashing treatment on carbonate clumped isotopes. Rapid Communications in Mass Spectrometry 34.ARTN e880210.1002/ rcm.8802

Adlan, Q., & John, C. M. (2023). Clumped isotope record of individual limestone fabrics: A potential method to constrain the timing of oil migration. Chemical Geology, 616, 121245.

Affek, H.P., Bar-Matthews, M., Ayalon, A., Matthews, A. and Eiler, J.M. (2008) Glacial/interglacial temperature variations in Soreq cave speleothems as recorded by 'clumped isotope' thermometry. Geochimica et Cosmochimica Acta 72, 5351-5360. 10.1016/j.gca.2008.06.031.

Al-Aasm, I. (2003) Origin and characterization of hydrothermal dolomite in the Western Canada Sedimentary Basin. J Geochem Explor 78, 9-15

Al-Mojel, A., Dera, G., Razin, P. and Le Nindre, Y.-M. (2018) Carbon and oxygen isotope stratigraphy of Jurassic platform carbonates from Saudi Arabia: Implications for diagenesis, correlations and global paleoenvironmental changes. Palaeogeography, Palaeoclimatology, Palaeoecology 511, 388-402. https://doi.org/10.1016/j.palaeo.2018.09.005

Aldega, L., Carminati, E., Scharf, A. and Mattern, F. (2021) Thermal maturity of the Hawasina units and origin of the Batinah Mélange (Oman Mountains): Insights from clay minerals. Marine and Petroleum Geology 133, 105316. https://doi.org/10.1016/j.marpetgeo.2021.105316

Alsharhan, A. (1989) Petroleum geology of the United Arab Emirates. Journal of Petroleum Geology 12, 253-288

Alsharhan, A.S. (1990) Geology and reservoir characteristics of Lower Cretaceous Kharaib Formation in Zakum Field, Abu Dhabi, United Arab Emirates. Geological Society, London, Special Publications 50, 299. 10.1144/GSL.SP.1990.050.01.16

Alsharhan, A.S. and Nairn, A.E.M. (2003) Chapter 6 - The end of the paleozoic and the early mesozoic of the middle east: The Absaroka Cycle, in: Alsharhan, A.S., Nairn, A.E.M. (Eds.), Sedimentary Basins and Petroleum Geology of the Middle East. Elsevier Science B.V., Amsterdam, pp. 161-233.

Alsuwaidi, M., Mohamed, A.A.I., Mansurbeg, H., Morad, S., Alsuwaidi, A., Al-Shalabi, E.W., Gomes, J., Al-Ramadan, K., Mohammed, I.Q. and Farouk, S. (2021) Depositional and diagenetic controls on reservoir quality of microporous basinal lime mudstones (Aptian), United Arab Emirates. Sediment Geol 420, 105925. https://doi.org/10.1016/j.sedgeo.2021.105925

Amo, M., Taniwaki, T., Yamanaka, M., Kato, A., Shinbo, E. and Shibuya, S. (2018) A Biomarker and Isotopic Study of the Source Rock Organofacies, Oil Families, Source-

oil Correlation and Thermal Maturity of Cenomanian Petroleum Systems in the Offshore Abu Dhabi, Abu Dhabi International Petroleum Exhibition & Conference.10.2118/192671-ms

Anderson, N.T., Kelson, J.R., Kele, S., Daeron, M., Bonifacie, M., Horita, J., Mackey, T.J., John, C.M., Kluge, T., Petschnig, P., Jost, A.B., Huntington, K.W., Bernasconi, S.M. and Bergmann, K.D. (2021a) A Unified Clumped Isotope Thermometer Calibration (0.5-1,100 degrees C) Using Carbonate-Based Standardization. Geophys Res Lett 48

Anderson, N.T., Kelson, J.R., Kele, S., Daëron, M., Bonifacie, M., Horita, J., Mackey, T.J., John, C.M., Kluge, T., Petschnig, P., Jost, A.B., Huntington, K.W., Bernasconi, S.M. and Bergmann, K.D. (2021b) A Unified Clumped Isotope Thermometer Calibration (0.5–1,100°C) Using Carbonate-Based Standardization. Geophys Res Lett 48, e2020GL092069. https://doi.org/10.1029/2020GL092069

Anderson, T.F. and Arthur, M.A. (1983) Stable isotopes of oxygen and carbon and their application to sedimentologic and paleoenvironmental problems. Stable Isotopes in Sedimentary Geology. SEPM Society for Sedimentary Geology. pp. 1.1-1.151. https://doi.org/10.2110/scn.83.10

Banner, J.L. and Hanson, G.N. (1990) Calculation of simultaneous isotopic and trace element variations during water-rock interaction with applications to carbonate diagenesis. Geochimica et Cosmochimica Acta 54, 3123-3137. https://doi.org/10.1016/0016-7037(90)90128-8

Barata, J., Vahrenkamp, V., Van Laer, P.J., Swart, P. and Murray, S. (2015) A Regional Analysis of Clumped Isotope Geochemistry to Define the Timing of Creation of Micro-Porosity in a Lower Cretaceous Giant Reservoir. In Abu Dhabi International Petroleum Exhibition and Conference. November 2015. https://doi.org/10.2118/177922-MS

Barclay, S.A., Worden, R.H. and Heasley, E.C. (1999) The effects of petroleum emplacement on diagenesis : a comparison between sandstone and carbonate reservoirs. Sciences Géologiques. Bulletins et Mémoires, 149-153

Barclay, S. A., & Worden, R. H. (2000). Effects of reservoir wettability on quartz cementation in oil fields. Quartz cementation in sandstones, 103-117.

Barker, C.E. (1983) Influence of time on metamorphism of sedimentary organic matter in liquid-dominated geothermal systems, western North America. Geology 11, 384-388

Bathurst, R. (1966) Boring algae, micrite envelopes and lithification of molluscan biosparites. Geol J 5, 15-32

Bechennec, F., Le Metour, J., Rabu, D., Bourdillon-de-Grissac, C., de Wever, P., Beurrier, M. and Villey, M. (1990) The Hawasina Nappes: stratigraphy, palaeogeography and structural evolution of a fragment of the south-Tethyan passive continental margin. Geological Society, London, Special Publications 49, 213-223

Beckert, J., Vandeginste, V. and John, C.M. (2015) Exploring the geological features and processes that control the shape and internal fabrics of late diagenetic dolomite bodies (Lower Khuff equivalent – Central Oman Mountains). Marine and Petroleum Geology 68, 325-340. https://doi.org/10.1016/j.marpetgeo.2015.08.038

Beckert, J., Vandeginste, V. and John, C.M. (2016) Relationship between karstification and burial dolomitization in Permian platform carbonates (Lower Khuff — Oman). Sediment Geol 342, 165-179. https://doi.org/10.1016/j.sedgeo.2016.07.001

Belkind, A. and Gershman, S. (2008) Plasma Cleaning of Surfaces. Vacuum Coating and Technology November, 46-57

Bergmann, K.D., Al Balushi, S.A.K., Mackey, T.J., Grotzinger, J.P. and Eiler, J.M. (2018a) A 600-Million-Year Carbonate Clumped-Isotope Record from the Sultanate of Oman. J Sediment Res 88, 960-979. 10.2110/jsr.2018.51

Bergmann, K.D., Finnegan, S., Creel, R., Eiler, J.M., Hughes, N.C., Popov, L.E. and Fischer, W.W. (2018b) A paired apatite and calcite clumped isotope thermometry approach to estimating Cambro-Ordovician seawater temperatures and isotopic composition. Geochimica et Cosmochimica Acta 224, 18-41

Bernasconi, S.M., Daëron, M., Bergmann, K.D., Bonifacie, M., Meckler, A.N., Affek, H.P., Anderson, N., Bajnai, D., Barkan, E., Beverly, E., Blamart, D., Burgener, L., Calmels, D., Chaduteau, C., Clog, M., Davidheiser-Kroll, B., Davies, A., Dux, F., Eiler, J., Elliott, B., Fetrow, A.C., Fiebig, J., Goldberg, S., Hermoso, M., Huntington, K.W., Hyland, E., Ingalls, M., Jaggi, M., John, C.M., Jost, A.B., Katz, S., Kelson, J., Kluge, T., Kocken, I.J., Laskar, A., Leutert, T.J., Liang, D., Lucarelli, J., Mackey, T.J., Mangenot, X., Meinicke, N., Modestou, S.E., Müller, I.A., Murray, S., Neary, A., Packard, N., Passey, B.H., Pelletier, E., Petersen, S., Piasecki, A., Schauer, A., Snell, K.E., Swart, P.K., Tripati, A., Upadhyay, D., Vennemann, T., Winkelstern, I., Yarian, D., Yoshida, N., Zhang, N. and Ziegler, M. (2021) InterCarb: A Community Effort to Improve Interlaboratory Standardization of the Carbonate Clumped Isotope Thermometer Using Carbonate Standards. Geochemistry, Geophysics, Geosystems 22, e2020GC009588. https://doi.org/10.1029/2020GC009588

Bernasconi, S.M., Hu, B., Wacker, U., Fiebig, J., Breitenbach, S.F.M. and Rutz, T. (2013) Background effects on Faraday collectors in gas-source mass spectrometry and implications for clumped isotope measurements. Rapid Commun Mass Sp 27, 603-612. 10.1002/rcm.6490

Beydoun, Z.R., Bamahmoud, M.O. and Nani, A.S.O. (1993) The Qishn Formation, Yemen: lithofacies and hydrocarbon habitat. Marine and Petroleum Geology 10, 364-372. https://doi.org/10.1016/0264-8172(93)90081-3

Bird, M.I., Charville-Mort, P.D.J., Ascough, P.L., Wood, R., Higham, T. and Apperley, D. (2010) Assessment of oxygen plasma ashing as a pre-treatment for radiocarbon dating. Quat Geochronol 5, 435-442. 10.1016/j.quageo.2009.10.004

Bjorkum, P.A. and Nadeau, P.H. (1998) Temperature controlled porosity/permeability reduction, fluid migration, and petroleum exploration in sedimentary basins. Journal of the Australian Petroleum Production & Exploration Association 38, 453-465. https://doi.org/10.1071/AJ97022

Bloch, S., Lander, R. H., & Bonnell, L. (2002). Anomalously high porosity and permeability in deeply buried sandstone reservoirs: Origin and predictability. AAPG bulletin, 86(2), 301-328.

Boni, M., Parente, G., Bechstaedt, T., De Vivo, B. and Iannace, A. (2000) Hydrothermal dolomites in SW Sardinia (Italy): evidence for a widespread late-Variscan fluid flow event. Sediment Geol 131, 181-200

Boomer, I. (1993) Paleoenvironmental Indicators from Late Holocene and Contemporary Ostracoda of the Aral Sea. Palaeogeogr Palaeocl 103, 141-153. Doi 10.1016/0031-0182(93)90140-E

Brasher, J.E. and Vagle, K.R. (1996) Influence of Lithofacies and Diagenesis on Norwegian North Sea Chalk Reservoirs1. Aapg Bull 80, 746-768. 10.1306/64ED88AE-1724-11D7-8645000102C1865D

Brenner, D.C., Passey, B.H. and Stolper, D.A. (2018) Influence of water on clumped-isotope bond reordering kinetics in calcite. Geochimica et Cosmochimica Acta 224, 42-63. 10.1016/j.gca.2017.12.026

Brown, A. (1997) Porosity variation in carbonates as a function of depth: Mississippian Madison Group, Williston Basin. AAPG Memoir 69: Reservoir Quality Prediction in Sandstones and Carbonates. 29-46.

Budd, D.A. (1989) Micro-rhombic calcite and microporosity in limestones: a geochemical study of the lower cretaceous thamama group, U.A.E. Sediment Geol 63, 293-311. https://doi.org/10.1016/0037-0738(89)90137-1

Budd, D.A., Frost, E.L., Huntington, K.W. and Allwardt, P.F. (2013) Syndepositional Deformation Features in High-Relief Carbonate Platforms: Long-Lived Conduits for Diagenetic Fluids. J Sediment Res 83, 14-38.10.2110/jsr.2013.3

Burnham, A.K., Braun, R.L., Gregg, H.R. and Samoun, A.M. (1987) Comparison of methods for measuring kerogen pyrolysis rates and fitting kinetic parameters. Energy & Fuels 1, 452-458

Burnham, A.K. and Sweeney, J.J. (1989) A chemical kinetic model of vitrinite maturation and reflectance. Geochimica et Cosmochimica Acta 53, 2649-2657

Burruss, R.C., Cercone, K.R. and Harris, P.M. (1985) Timing of hydrocarbon migration: evidenced from fluid inclusions in calcite cements, tectonics and burial history. SEPM Special Publication 36-Carbonate Cements.277-290. https://doi.org/10.2110/pec.85.36

Burst, J.F. (1969) Diagenesis of Gulf Coast clayey sediments and its possible relation to petroleum migration. AAPG Bulletin 53, 73-93

Carballo, J., Land, L.S. and Miser, D.E. (1987) Holocene dolomitization of supratidal sediments by active tidal pumping, Sugarloaf Key, Florida. J Sediment Res 57, 153-165.10.1306/212f8ad0-2b24-11d7-8648000102c1865d

Carminati, E., Aldega, L., Smeraglia, L., Scharf, A., Mattern, F., Albert, R. and Gerdes, A. (2020) Tectonic Evolution of the Northern Oman Mountains, Part of the Strait of Hormuz Syntaxis: New Structural and Paleothermal Analyses and U-Pb Dating of Synkinematic Calcite. Tectonics 39, e2019TC005936. https://doi.org/10.1029/2019TC005936

Chen, S., Ryb, U., Piasecki, A.M., Lloyd, M.K., Baker, M.B. and Eiler, J.M. (2019) Mechanism of solid-state clumped isotope reordering in carbonate minerals from aragonite heating experiments. Geochimica et Cosmochimica Acta 258, 156-173

Choquette, P. and Pray, L.C. (1970) Geologic Nomenclature and Classification of Porosity in Sedimentary Carbonates. AAPG Bulletin 54, 207-250

Choquette, P.W., James, N., McIlreath, I. and Morrow, D. (1990) Limestones—the burial diagenetic environment. Diagenesis: Geoscience Canada, Reprint Series 4, 75-111

Cohen, J. (1977) Chapter 1 - The Concepts of Power Analysis, in: Cohen, J. (Ed.), Statistical Power Analysis for the Behavioral Sciences. Academic Press, pp. 1-17.

Cooper, D.J.W., Ali, M.Y. and Searle, M.P. (2014) Structure of the northern Oman Mountains from the Semail Ophiolite to the Foreland Basin. Geological Society, London, Special Publications, 392(1), 129-153. https://doi.org/10.1144/SP392.7

Cooper, D.J.W., Ali, M.Y. and Searle, M.P. (2018) Origin and implications of a thrust-bound gypsiferous unit along the western edge of Jabal Sumeini, northern Oman Mountains. J Asian Earth Sci 154, 101-124. https://doi.org/10.1016/j.jseaes.2017.12.018

Cox, P.A., Wood, R.A., Dickson, J.A.D., Al Rougha, H.B., Shebl, H. and Corbett, P.W.M. (2010) Dynamics of cementation in response to oil charge: Evidence from a

Cretaceous carbonate field, U.A.E. Sediment Geol 228, 246-254. https://doi.org/10.1016/j.sedgeo.2010.04.016

Criss, R.E., Gregory, R.T. and Taylor, H.P. (1987) Kinetic theory of oxygen isotopic exchange between minerals and water. Geochimica et Cosmochimica Acta 51, 1099-1108. https://doi.org/10.1016/0016-7037(87)90203-1

Cummins, R.C., Finnegan, S., Fike, D.A., Eiler, J.M. and Fischer, W.W. (2014) Carbonate clumped isotope constraints on Silurian ocean temperature and seawater delta O-18. Geochimica et Cosmochimica Acta 140, 241-258.10.1016/j.gca.2014.05.024

Curtis, J.H., Hodell, D.A., Swart, P.K., Lohmann, K.C., McKenzie, J. and Savin, S. (1993) An Isotopic and Trace Element Study of Ostracods from Lake Miragoane, Haiti: A 10,500 Year Record of Paleosalinity and Paleotemperature Changes in the Caribbean. 631-152.10.1029/GM078p0135

D'Autry, W., Wolfs, K., Yarramraju, S., Schepdael, A. V., Hoogmartens, J., & Adams, E. (2010). Characterization and improvement of signal drift associated with electron ionization quadrupole mass spectrometry. Analytical chemistry, 82(15), 6480-6486.

D'Heur, M. (1984) Porosity and hydrocarbon distribution in the North Sea chalk reservoirs. Marine and Petroleum Geology 1, 211-238

Dai, X.J. (1996) Kinetic model of an RF discharge in oxygen. Aust J Phys 49, 1169-1180. Doi 10.1071/Ph961169

Dale, A., John, C.M., Mozley, P.S., Smalley, P.C. and Muggeridge, A.H. (2014) Time-capsule concretions: Unlocking burial diagenetic processes in the Mancos Shale using carbonate clumped isotopes. Earth and Planetary Science Letters 394, 30-37. 10.1016/j.epsl.2014.03.004

Davies, A.J. and John, C.M. (2017) Reducing contamination parameters for clumped isotope analysis: The effect of lowering Porapak (TM) Q trap temperature to below-50 degrees C. Rapid Communications in Mass Spectrometry 31, 1313-1323.10.1002/rcm.7902

Davies, A.J. and John, C.M. (2019) The clumped (C-13 - O-18) isotope composition of echinoid calcite: Further evidence for "vital effects" in the clumped isotope proxy. Geochimica et Cosmochimica Acta 245, 172-189. 10.1016/j.gca.2018.07.038

del Real, P.G., Maher, K., Kluge, T., Bird, D.K., Brown, G.E. and John, C.M. (2016) Clumped-isotope thermometry of magnesium carbonates in ultramafic rocks. Geochimica et Cosmochimica Acta 193, 222-250.10.1016/j.gca.2016.08.003

Dennis, K.J., Affek, H.P., Passey, B.H., Schrag, D.P. and Eiler, J.M. (2011) Defining an absolute reference frame for 'clumped' isotope studies of CO2. Geochimica et Cosmochimica Acta 75, 7117-7131.10.1016/j.gca.2011.09.025

Dennis, K.J. and Schrag, D.P. (2010) Clumped isotope thermometry of carbonatites as an indicator of diagenetic alteration. Geochimica et Cosmochimica Acta 74, 4110-4122.10.1016/j.gca.2010.04.005

Deville de Periere, M., Durlet, C., Vennin, E., Lambert, L., Bourillot, R., Caline, B. and Poli, E. (2011) Morphometry of micrite particles in cretaceous microporous limestones of the Middle East: Influence on reservoir properties. Marine and Petroleum Geology 28, 1727-1750. https://doi.org/10.1016/j.marpetgeo.2011.05.002

Dodson, M.H. (1973) Closure temperature in cooling geochronological and petrological systems. Contributions to Mineralogy and Petrology 40, 259-274. 10.1007/BF00373790

Durazzi, J.T. (1977) Stable Isotopes in Ostracod Shell - Preliminary-Study. Geochimica Et Cosmochimica Acta 41, 1168-1170. Doi 10.1016/0016-7037(77)90113-2

Ehrenberg, S.N., Lokier, S.W., Yaxin, L. and Chen, R. (2018) Depositional Cycles in a Lower Cretaceous Limestone Reservoir, Onshore Abu Dhabi, U.A.E. Journal of Sedimentary Research, 88(7), 753-776.10.2110/jsr.2018.41

Ehrenberg, S.N., Morad, S., Yaxin, L. and Chen, R. (2016) Stylolites and Porosity In A Lower Cretaceous Limestone Reservoir, Onshore Abu Dhabi, U.A.E. Journal of Sedimentary Research 86, 1228-1247.10.2110/jsr.2016.68

Ehrenberg, S. N., Skjevrak, I., & Gilje, A. E. (1995). Asphaltene-rich residues in sandstone reservoirs of Haltenbanken province, mid-Norwegian continental shelf. Marine and Petroleum Geology, 12(1), 53-69.

Ehrenberg, S.N. and Wu, Q. (2019) Dense Zones of the Kharaib Formation (Lower Cretaceous), United Arab Emirates. Journal of Sedimentary Research 89, 353-380. 10.2110/jsr.2019.20

Ehrenberg, S.N., Zhang, J. and Gomes, J.S. (2020) Regional porosity variation in Thamama-B reservoirs of Abu Dhabi. Marine and Petroleum Geology 114, 104245. https://doi.org/10.1016/j.marpetgeo.2020.104245

Eiler, J.M. (2007) "Clumped-isotope" geochemistry - The study of naturally-occurring, multiply-substituted isotopologues. Earth and Planetary Science Letters 262, 309-327. 10.1016/j.epsl.2007.08.020

Eiler, J.M. (2011) Paleoclimate reconstruction using carbonate clumped isotope thermometry. Quaternary Sci Rev 30, 3575-3588. 10.1016/j.quascirev.2011.09.001

Eiler, J.M. and Schauble, E. (2004) $^{18}O^{13}C^{16}O$ in Earth's atmosphere. Geochimica et Cosmochimica Acta 68, 4767-4777. https://doi.org/10.1016/j.gca.2004.05.035

Epstein, A.G., Epstein, J.B. and Harris, L.D. (1977) Conodont color alteration: an index to organic metamorphism, Professional Paper, Vol. 995, pp. 1-27. US Government Printing Office. https://doi.org/10.3133/ofr75379

Epstein, S., Buchsbaum, R., Lowenstam, H. and Urey, H.C. (1951) Carbonate-water isotopic temperature scale. GSA Bulletin 62, 417-426.

Epstein, S., Buchsbaum, R., Lowenstam, H.A. and Urey, H.C. (1953) Revised carbonate-water isotopic temperature scale. Geological Society of America Bulletin, 64(11), 1315-1326.

Epstein, S. A., & Friedman, G. M. (1983). Depositional and diagenetic relationships between Gulf of Elat (Aqaba) and Mesozoic of United States east coast offshore. AAPG bulletin, 67(6), 953-962.

Fallet, U., Boer, W., van Assen, C., Greaves, M. and Brummer, G.-J.A. (2009) A novel application of wet oxidation to retrieve carbonates from large organic-rich samples for ocean-climate research. Geochemistry, Geophysics, Geosystems 10(8). 10.1029/2009gc002573

Fan, M., Heller, P., Allen, S.D. and Hough, B.G. (2014) Middle Cenozoic uplift and concomitant drying in the central Rocky Mountains and adjacent Great Plains. Geology 42, 547-550

Feazel, C.T. and Schatzinger, R. (1985) Prevention of Carbonate Cementation in Petroleum Reservoirs. SEPM Special Publication 36-Carbonate Cements. 459. https://doi.org/10.2110/pec.85.36.0097

Fernandez, A., Korte, C., Ullmann, C.V., Looser, N., Wohlwend, S. and Bernasconi, S.M. (2021) Reconstructing the magnitude of Early Toarcian (Jurassic) warming using the

reordered clumped isotope compositions of belemnites. Geochimica et Cosmochimica Acta 293, 308-327. https://doi.org/10.1016/j.gca.2020.10.005

Ferry, J.M., Passey, B.H., Vasconcelos, C. and Eiler, J.M. (2011) Formation of dolomite at 40-80 degrees C in the Latemar carbonate buildup, Dolomites, Italy, from clumped isotope thermometry. Geology 39, 571-574. 10.1130/G31845.1

Finnegan, S., Bergmann, K., Eiler, J.M., Jones, D.S., Fike, D.A., Eisenman, I., Hughes, N.C., Tripati, A.K. and Fischer, W.W. (2011) The Magnitude and Duration of Late Ordovician;Early Silurian Glaciation. Science 331, 903-906. doi:10.1126/science.1200803

Fisher, R.A. (1936) Design of Experiments. British Medical Journal 1, 554. 10.1136/bmj.1.3923.554-a

Flügel, E. (2010) Diagenesis, Porosity, and Dolomitization, in: Flügel, E. (Ed.), Microfacies of Carbonate Rocks: Analysis, Interpretation and Application. Springer Berlin Heidelberg, Berlin, Heidelberg, pp. 267-338.

Friedman, I. and O'Neil, J.R. (1977) Compilation of stable isotope fractionation factors of geochemical interest. Data of geochemistry, KK1-KK12. https://doi.org/10.3133/pp440KK

Friedman and Sanders (1978) Principles of Sedimentology. New York: John Wiley & Sons. p. 792.

Frijia, G., Parente, M., Di Lucia, M. and Mutti, M. (2015) Carbon and strontium isotope stratigraphy of the Upper Cretaceous (Cenomanian-Campanian) shallow-water carbonates of southern Italy: Chronostratigraphic calibration of larger foraminifera biostratigraphy. Cretaceous Res 53, 110-139

Frye, G.C. and Thomas, M.M. (1993) Adsorption of organic compounds on carbonate minerals: 2. Extraction of carboxylic acids from recent and ancient carbonates. Chem Geol 109, 215-226. https://doi.org/10.1016/0009-2541(93)90071-P

Gallagher, T.M., Sheldon, N.D., Mauk, J.L., Petersen, S.V., Gueneli, N. and Brocks, J.J. (2017) Constraining the thermal history of the North American Midcontinent Rift System using carbonate clumped isotopes and organic thermal maturity indices. Precambrian Res 294, 53-66.1 0.1016/j.precamres.2017.03.022

Garzione, C.N., Auerbach, D.J., Smith, J.J.-S., Rosario, J.J., Passey, B.H., Jordan, T.E. and Eiler, J.M. (2014) Clumped isotope evidence for diachronous surface cooling of the Altiplano and pulsed surface uplift of the Central Andes. Earth and Planetary Science Letters 393, 173-181

Ghosh, P., Adkins, J., Affek, H., Balta, B., Guo, W., Schauble, E.A., Schrag, D. and Eiler, J.M. (2006) 13C–18O bonds in carbonate minerals: A new kind of paleothermometer. Geochimica et Cosmochimica Acta 70, 1439-1456. 10.1016/j.gca.2005.11.014

Ghosh, P., Eiler, J., Campana, S.E. and Feeney, R.F. (2007) Calibration of the carbonate 'clumped isotope' paleothermometer for otoliths. Geochimica et Cosmochimica Acta 71, 2736-2744. 10.1016/j.gca.2007.03.015

Giles, M.R., Stevenson, S., Martin, S.V., Cannon, S.J.C., Hamilton, P.J., Marshall, J.D. and Samways, G.M. (1992) The reservoir properties and diagenesis of the Brent Group: a regional perspective. Geological Society, London, Special Publications, 61(1), 289-327.

Gleadow, A.J.W., Duddy, I.R., Green, P.F. and Hegarty, K.A. (1986) Fission track lengths in the apatite annealing zone and the interpretation of mixed ages. Earth and Planetary Science Letters 78, 245-254. https://doi.org/10.1016/0012-821X(86)90065-8

Gluyas, J. G., Robinson, A. G., Emery, D., Grant, S. M., and Oxtoby, N. H. (1993) The link between petroleum emplacement and sandstone cementation, in Parker, J., ed., Petroleum Geology of the North west Europe, Geological Society of London, v. 4, p. 1395-1402.

Goldsmith, J.R. and Graf, D.L. (1958) Structural and compositional variations in some natural dolomites. The Journal of Geology 66, 678-693

Goreau, T.J. and Yonge, M. (1977) Coral skeletal chemistry: physiological and environmental regulation of stable isotopes and trace metals in Montastrea annularis. Proceedings of the Royal Society of London. Series B. Biological Sciences 196, 291-315. 10.1098/rspb.1977.0042

Gregg, J.M., Bish, D.L., Kaczmarek, S.E. and Machel, H.G. (2015) Mineralogy, nucleation and growth of dolomite in the laboratory and sedimentary environment: a review. Sedimentology 62, 1749-1769

Gregory, R.T., Criss, R.E. and Taylor, H.P. (1989) Oxygen isotope exchange kinetics of mineral pairs in closed and open systems: Applications to problems of hydrothermal alteration of igneous rocks and Precambrian iron formations. Chem Geol 75, 1-42. https://doi.org/10.1016/0009-2541(89)90019-3

Gregory, R.T. and Taylor Jr, H.P. (1981) An oxygen isotope profile in a section of Cretaceous oceanic crust, Samail Ophiolite, Oman: Evidence for δ18O buffering of the oceans by deep (> 5 km) seawater-hydrothermal circulation at mid-ocean ridges. Journal of Geophysical Research: Solid Earth 86, 2737-2755

Grobe, A., Urai, J.L., Littke, R. and Lünsdorf, N.K. (2016) Hydrocarbon generation and migration under a large overthrust: The carbonate platform under the Semail Ophiolite, Jebel Akhdar, Oman. Int J Coal Geol 168, 3-19. https://doi.org/10.1016/j.coal.2016.02.007

Grobe, A., von Hagke, C., Littke, R., Dunkl, I., Wübbeler, F., Muchez, P. and Urai, J.L. (2019) Tectono-thermal evolution of Oman's Mesozoic passive continental margin under the obducting Semail Ophiolite: a case study of Jebel Akhdar, Oman. Solid Earth 10, 149-175. 10.5194/se-10-149-2019

Gumati, Y. (1993) Kinetic modelling, thermal maturation and hydrocarbon generation in the United Arab Emirates. Marine and Petroleum Geology 10, 153-161

Guo, W. and Eiler, J.M. (2007) Temperatures of aqueous alteration and evidence for methane generation on the parent bodies of the CM chondrites. Geochimica et Cosmochimica Acta 71, 5565-5575. 10.1016/j.gca.2007.07.029

Hanna, S.S. (1990) The Alpine deformation of the central Oman Mountains. Geological Society London Special Publications 49, 341-359. https://doi.org/10.1144/GSL.SP.1992.049.01.21

Heasley, E. C., Worden, R. H., & Hendry, J. P. (2000). Cement distribution in a carbonate reservoir: recognition of a palaeo oil–water contact and its relationship to reservoir quality in the Humbly Grove field, onshore, UK. Marine and Petroleum Geology, 17(5), 639-654.

Hemingway, J.D. (2020) isotopylog: open-source tools for clumped isotope kinetic data analysis. http://pypi.python.org/pypi/isotopylog [online; accessed 2021-08-25]

Hemingway, J.D. and Henkes, G.A. (2021) A disordered kinetic model for clumped isotope bond reordering in carbonates. Earth and Planetary Science Letters 566, 116962. https://doi.org/10.1016/j.epsl.2021.116962

Henkes, G.A., Passey, B.H., Grossman, E.L., Shenton, B.J., Perez-Huerta, A. and Yancey, T.E. (2014) Temperature limits for preservation of primary calcite clumped isotope paleotemperatures. Geochimica et Cosmochimica Acta 139, 362-382. 10.1016/j.gca.2014.04.040

Henry, D.G., Watson, J.S. and John, C.M. (2017) Assessing and calibrating the ATR-FTIR approach as a carbonate rock characterization tool. Sediment Geol 347, 36-52. https://doi.org/10.1016/j.sedgeo.2016.07.003

Hoefs, J. (2015). Isotope Fractionation Processes of Selected Elements. In: Stable Isotope Geochemistry. 49-265. https://doi.org/10.1007/978-3-319-19716-6_2

Hönig, M.R. and John, C.M. (2015) Sedimentological and isotopic heterogeneities within a Jurassic carbonate ramp (UAE) and implications for reservoirs in the Middle East. Marine and Petroleum Geology 68, 240-257. https://doi.org/10.1016/j.marpetgeo.2015.08.029

Hönig, M.R., John, C.M. and Manning, C. (2017) Development of an equatorial carbonate platform across the Triassic-Jurassic boundary and links to global palaeoenvironmental changes (Musandam Peninsula, UAE/Oman). Gondwana Research 45, 100-117. https://doi.org/10.1016/j.gr.2016.11.007

Honlet, R., Gasparrini, M., Muchez, P., Swennen, R. and John, C.M. (2018) A new approach to geobarometry by combining fluid inclusion and clumped isotope thermometry in hydrothermal carbonates. Terra Nova 30, 199-206. 10.1111/ter.12326

Horita, J. (2014) Oxygen and carbon isotope fractionation in the system dolomite–water–CO2 to elevated temperatures. Geochimica et Cosmochimica Acta 129, 111-124 .https://doi.org/10.1016/j.gca.2013.12.027

Hsu, J.C. (1996) Multiple comparisons : theory and methods.. Chapman & Hall, London. 43-180.

Huntington, K.W., Budd, D.A., Wernicke, B.P. and Eiler, J.M. (2011) Use of Clumped-Isotope Thermometry to Constrain the Crystallization Temperature of Diagenetic Calcite. J Sediment Res 81, 656-669.10.2110/jsr.2011.51

Huntington, K.W., Eiler, J.M., Affek, H.P., Guo, W., Bonifacie, M., Yeung, L.Y., Thiagarajan, N., Passey, B., Tripati, A., Daeron, M. and Came, R. (2009) Methods and limitations of 'clumped' CO2 isotope (Delta(47)) analysis by gas-source isotope ratio mass spectrometry. J Mass Spectrom 44, 1318-1329. 10.1002/jms.1614

Huntington, K.W. and Lechler, A.R. (2015) Carbonate clumped isotope thermometry in continental tectonics. Tectonophysics 647, 1-20. 10.1016/j.tecto.2015.02.019

Huntington, K.W., Wernicke, B.P. and Eiler, J.M. (2010) Influence of climate change and uplift on Colorado Plateau paleotemperatures from carbonate clumped isotope thermometry. Tectonics 29 (3). https://doi.org/10.1029/2009TC002449

Hurai, V., Huraiová, M., Slobodník, M. and Thomas, R. (2015) Chapter 9 - Stable Isotope Geochemistry of Geofluids, in: Hurai, V., Huraiová, M., Slobodník, M., Thomas, R. (Eds.), Geofluids. Elsevier, pp. 293-344.

Immenhauser, A. (2022) On the delimitation of the carbonate burial realm. The Depositional Record 8, 524-574. https://doi.org/10.1002/dep2.173

Immenhauser, A., Hillgärtner, H., Sattler, U., Bertotti, G., Schoepfer, P., Homewood, P., Vahrenkamp, V., Steuber, T., Masse, J.-P., Droste, H., Koppen, J.T.-v., van der Kooij, B., van Bentum, E., Verwer, K., Strating, E.H., Swinkels, W., Peters, J., Immenhauser-Potthast, I. and Al Maskery, S. (2004) Barremian-lower Aptian Qishn

Formation, Haushi-Huqf area, Oman: a new outcrop analogue for the Kharaib/Shu'aiba reservoirs. Geoarabia 9, 153-194. 10.2113/geoarabia0901153

Ingalls, M. (2019) Reconstructing carbonate alteration histories in orogenic sedimentary basins: Xigaze forearc, southern Tibet. Geochimica et Cosmochimica Acta 251, 284-300. https://doi.org/10.1016/j.gca.2019.02.005

John, C.M. (2018) Burial estimates constrained by clumped isotope thermometry: example of the Lower Cretaceous Qishn Formation (Haushi-Huqf High, Oman). Geological Society, London, Special Publications 435, 107-121. 10.1144/SP435.5

John, C.M. and Bowen, D. (2016) Community software for challenging isotope analysis: First applications of "Easotope' to clumped isotopes. Rapid Commun Mass Sp 30, 2285-2300. 10.1002/rcm.7720

Johnson, R. H. (1920) The cementation process in sandstone: American Association of Petroleum Geologists Bulletin, v. 4, p. 33-35.

Jones, B., Luth, R.W. and MacNeil, A.J. (2001) Powder X-Ray Diffraction Analysis of Homogeneous and Heterogeneous Sedimentary Dolostones. J Sediment Res 71, 790-799.10.1306/2dc40968-0e47-11d7-8643000102c1865d

Kaczmarek, S.E. and Sibley, D.F. (2007) A Comparison of Nanometer-Scale Growth and Dissolution Features on Natural and Synthetic Dolomite Crystals: Implications for the Origin of Dolomite. J Sediment Res 77, 424-432.10.2110/jsr.2007.035

Kaczmarek, S.E. and Sibley, D.F. (2011) On the evolution of dolomite stoichiometry and cation order during high-temperature synthesis experiments: An alternative model for the geochemical evolution of natural dolomites. Sediment Geol 240, 30-40. https://doi.org/10.1016/j.sedgeo.2011.07.003

Kaczmarek, S.E. and Sibley, D.F. (2014) Direct physical evidence of dolomite recrystallization. Sedimentology 61, 1862-1882.https://doi.org/10.1111/sed.12119

Kaczmarek, S.E. and Thornton, B.P. (2017) The effect of temperature on stoichiometry, cation ordering, and reaction rate in high-temperature dolomitization experiments. Chem Geol 468, 32-41.https://doi.org/10.1016/j.chemgeo.2017.08.004

Kim, S.-T. and O'Neil, J.R. (1997) Equilibrium and nonequilibrium oxygen isotope effects in synthetic carbonates. Geochimica et Cosmochimica Acta 61, 3461-3475

Kim, S.T., Mucci, A. and Taylor, B.E. (2007) Phosphoric acid fractionation factors for calcite and aragonite between 25 and 75 degrees C: Revisited. Chem Geol 246, 135-146.10.1016/j.chemgeo.2007.08.005

Kırmacı, M.Z. (2013) Origin of dolomite in the Late Jurassic platform carbonates, Bolkar Mountains, Central Taurides, Turkey: Petrographic and geochemical evidence. Geochemistry 73, 383-398. https://doi.org/10.1016/j.chemer.2012.11.001

Koch, A. and Siegesmund, S. (2004) The combined effect of moisture and temperature on the anomalous expansion behaviour of marble. Environ Geol 46, 350-363.10.1007/s00254-004-1037-9

Kolchugin, A.N., Immenhauser, A., Walter, B.F. and Morozov, V.P. (2016) Diagenesis of the palaeo-oil-water transition zone in a Lower Pennsylvanian carbonate reservoir: Constraints from cathodoluminescence microscopy, microthermometry, and isotope geochemistry. Marine and Petroleum Geology 72, 45-61. https://doi.org/10.1016/j.marpetgeo.2016.01.014

Lacroix, B. and Niemi, N.A. (2019) Investigating the effect of burial histories on the clumped isotope thermometer: An example from the Green River and Washakie

Basins, Wyoming. Geochimica et Cosmochimica Acta 247, 40-58.
10.1016/j.gca.2018.12.016

Lambert, L., Durlet, C., Loreau, J.-P. and Marnier, G. (2006) Burial dissolution of micrite in Middle East carbonate reservoirs (Jurassic–Cretaceous): keys for recognition and timing. Marine and Petroleum Geology 23, 79-92.
https://doi.org/10.1016/j.marpetgeo.2005.04.003

Landmesser, P. and Saydam, A.S. (1996) Seismostratigraphic Interpretation of Lower Thamama/Habshan. Abu Dhabi International Petroleum Exhibition and Conference. October 1996. doi: https://doi.org/10.2118/36204-MS

Lawson, M., Shenton, B.J., Stolper, D.A., Eiler, J.M., Rasbury, E.T., Becker, T.P., Phillips-Lander, C.M., Buono, A.S., Becker, S.P. and Pottorf, R. (2018) Deciphering the diagenetic history of the El Abra Formation of eastern Mexico using reordered clumped isotope temperatures and U-Pb dating. GSA Bulletin 130, 617-629

Lebeau, O., Busigny, V., Chaduteau, C. and Ader, M. (2014) Organic matter removal for the analysis of carbon and oxygen isotope compositions of siderite. Chem Geol 372, 54-61. 10.1016/j.chemgeo.2014.02.020

Lechler, A.R., Niemi, N.A., Hren, M.T. and Lohmann, K.C. (2013) Paleoelevation estimates for the northern and central proto–Basin and Range from carbonate clumped isotope thermometry. Tectonics 32, 295-316

Lerche, I. and McKenna, T.E. (1991) Pollen translucency as a thermal maturation indicator. Journal of Petroleum Geology 14, 19-35.
https://doi.org/10.1111/j.1747-5457.1991.tb00296.x

Lister, G.S. (1988) A 15,000-year Isotopic Record from Lake Zürich of Deglaciation and Climatic Change in Switzerland. Quaternary Research 29, 129-141.
10.1016/0033-5894(88)90056-7

Lloyd, M.K., Eiler, J.M. and Nabelek, P.I. (2017) Clumped isotope thermometry of calcite and dolomite in a contact metamorphic environment. Geochimica et Cosmochimica Acta 197, 323-344.10.1016/j.gca.2016.10.037

Lloyd, M.K., Ryb, U. and Eiler, J.M. (2018) Experimental calibration of clumped isotope reordering in dolomite. Geochimica et Cosmochimica Acta 242, 1-20.
https://doi.org/10.1016/j.gca.2018.08.036

Loosveld, R.J.H., Bell, A. and Terken, J.J.M. (1996) The Tectonic Evolution of Interior Oman. Geoarabia 1, 28-51.10.2113/geoarabia010128

Loyd, S.J., Corsetti, F.A., Eiler, J.M. and Tripati, A.K. (2012) Determining the Diagenetic Conditions of Concretion Formation: Assessing Temperatures and Pore Waters Using Clumped Isotopes. J Sediment Res 82, 1006-1016.10.2110/jsr.2012.85

Lu, Y.C., Song, S.R., Taguchi, S., Wang, P.L., Yeh, E.C., Lin, Y.J., MacDonald, J. and John, C.M. (2018) Evolution of hot fluids in the Chingshui geothermal field inferred from crystal morphology and geochemical vein data. Geothermics 74, 305-318.
10.1016/j.geothermics.2017.11.016

Lu, Y.C., Song, S.R., Wang, P.L., Wu, C.C., Mii, H.S., MacDonald, J., Shen, C.C. and John, C.M. (2017) Magmatic-like fluid source of the Chingshui geothermal field, NE Taiwan evidenced by carbonate clumped-isotope paleothermometry. J Asian Earth Sci 149, 124-133. 10.1016/j.jseaes.2017.03.004

Luczaj, J.A., Harrison III, W.B. and Smith Williams, N. (2006) Fractured hydrothermal dolomite reservoirs in the Devonian Dundee Formation of the central Michigan Basin. Aapg Bull 90, 1787-1801

Lukoczki, G., Haas, J., Gregg, J.M., Machel, H.G., Kele, S. and John, C.M. (2019) Multi-phase dolomitization and recrystallization of Middle Triassic shallow marine–peritidal carbonates from the Mecsek Mts. (SW Hungary), as inferred from petrography, carbon, oxygen, strontium and clumped isotope data. Marine and Petroleum Geology 101, 440-458. https://doi.org/10.1016/j.marpetgeo.2018.12.004

Lukoczki, G., Haas, J., Gregg, J.M., Machel, H.G., Kele, S. and John, C.M. (2020) Early dolomitization and partial burial recrystallization: a case study of Middle Triassic peritidal dolomites in the Villány Hills (SW Hungary) using petrography, carbon, oxygen, strontium and clumped isotope data. International Journal of Earth Sciences 109, 1051-1070. 10.1007/s00531-020-01851-7

Lumsden, D.N. (1979) Discrepancy between thin-section and X-ray estimates of dolomite in limestone. J Sediment Res 49, 429-435.10.1306/212f7761-2b24-11d7-8648000102c1865d

MacDonald, J., John, C. and Girard, J.P. (2015) Dolomitization processes in hydrocarbon reservoirs: insight from geothermometry using clumped isotopes. Proced Earth Plan Sc 13, 265-268. 10.1016/j.proeps.2015.07.062

Machel, H.G. and Lonnee, J. (2002) Hydrothermal dolomite—A product of poor definition and imagination. Sediment Geol 152, 163-171

Mahapoonyanont, N., Mahapoonyanont, T., Pengkaew, N. and Kamhangkit, R. (2010) Power of the test of One-Way Anova after transforming with large sample size data. Procedia - Social and Behavioral Sciences 9, 933-937. https://doi.org/10.1016/j.sbspro.2010.12.262

Manche, C.J. and Kaczmarek, S.E. (2019) Evaluating reflux dolomitization using a novel high-resolution record of dolomite stoichiometry: A case study from the Cretaceous of central Texas, USA. Geology 47, 586-590. 10.1130/g46218.1

Mangenot, X., Gasparrini, M., Rouchon, V. and Bonifacie, M. (2018) Basin-scale thermal and fluid flow histories revealed by carbonate clumped isotopes ((47)) - Middle Jurassic carbonates of the Paris Basin depocentre. Sedimentology 65, 123-150. 10.1111/sed.12427

Masse, J.-P. and Fenerci-Masse, M. (2015) Evolution of the rudist bivalve Agriopleura Kühn (Radiolitidae, Hippuritida) from the Mediterranean region. Palaeontology 58, 71-100. https://doi.org/10.1111/pala.12118

Masse, J., Maksoud, S., Fenerci-Masse, M., Granier, B. and Azar, D. (2015) Earliest Aptian Caprinidae (Bivalvia, Hippuritida) from Lebanon. Carnets de Géologie 15, 21-30

Mathieu, J., Kontak, D.J. and Turner, E.C. (2013) A fluid inclusion study of diagenetic fluids in Proterozoic and Paleozoic carbonate rocks, Victoria Island, NWT. Geofluids 13, 559-578. https://doi.org/10.1111/gfl.12063

McCulloh, T.H. and Naeser, N.D. (1989) Thermal History of Sedimentary Basins: Introduction and Overview, in: Naeser, N.D., McCulloh, T.H. (Eds.), Thermal History of Sedimentary Basins. Springer New York, New York, NY, pp. 1-11

McKenzie, D. (1978) Some remarks on the development of sedimentary basins. Earth and Planetary Science Letters 40, 25-32. https://doi.org/10.1016/0012-821X(78)90071-7

McLimans, R.K. (1987) The application of fluid inclusions to migration of oil and diagenesis in petroleum reservoirs. Appl Geochem 2, 585-603. https://doi.org/10.1016/0883-2927(87)90011-4

Meckler, A.N., Affolter, S., Dublyansky, Y.V., Kruger, Y., Vogel, N., Bernasconi, S.M., Frenz, M., Kipfer, R., Leuenberger, M., Spotl, C., Carolin, S., Cobb, K.M., Moerman,

J., Adkins, J.F. and Fleitmann, D. (2015) Glacial-interglacial temperature change in the tropical West Pacific: A comparison of stalagmite-based paleo-thermometers. Quaternary Sci Rev 127, 90-116. 10.1016/j.quascirev.2015.06.015

Melville, P., Jeelani, O.A., Menhali, S.A. and Grötsch, J. (2004) Three-Dimensional Seismic Analysis in the Characterization of a Giant Carbonate Field, Onshore Abu Dhabi, United Arab Emirates, in: Eberli, G.P., Masaferro, J.L., Sarg, J.F.R. (Eds.), Seismic Imaging of Carbonate Reservoirs and Systems. American Association of Petroleum Geologists Memoir 81, p. 123-148

Mering, J.A., Barker, S.L.L., Huntington, K.W., Simmons, S., Dipple, G., Andrew, B. and Schauer, A. (2018) Taking the Temperature of Hydrothermal Ore Deposits Using Clumped Isotope Thermometry. Econ Geol 113, 1671-1678. 10.5382/econgeo.2018.4608

Millan, M.I., Machel, H.G. and Bernasconi, S.M. (2016) Constraining Temperatures of Formation and Composition of Dolomitizing Fluids in the Upper Devonian Nisku Formation (Alberta, Canada) with Clumped Isotopes. J Sediment Res 86, 107-112. 10.2110/jsr.2016.6

Mitterer, R. M., & Cunningham, R. (1985). The interaction of natural organic matter with grain surfaces: implications for calcium carbonate precipitation. SEPM Special Publication 36-Carbonate Cements. https://doi.org/10.2110/pec.85.36.0017

Molenaar, N., Cyziene, J., Sliaupa, S. and Craven, J. (2008) Lack of inhibiting effect of oil emplacement on quartz cementation: Evidence from Cambrian reservoir sandstones, Paleozoic Baltic Basin. GSA Bulletin 120, 1280-1295.10.1130/B25979.1

Montenat, C., Barrier, P. and Soudet, H.J. (2003) Aptian faulting in the Haushi-Huqf (Oman) and the tectonic evolution of the southeast Arabian platform-margin. Geoarabia 8, 643-662.10.2113/geoarabia0804643

Moore, C.H. (1989a) Chapter 1-The Nature of Carbonate Depositional Systems-Comparison of Carbonates and Siliciclastics, in: Moore, C.H. (Ed.), Developments in Sedimentology. Elsevier, pp. 1-19.

Moore, C.H. (1989b) Chapter 3 Diagenetic Environments of Porosity Modification and Tools for Their Recognition in the Geologic Record, in: Moore, C.H. (Ed.), Developments in Sedimentology. Elsevier, pp. 43-74.

Moore, C.H. (1989c) Chapter 9 Burial Diagenetic Environment, in: Moore, C.H. (Ed.), Developments in Sedimentology. Elsevier, pp. 237-284.

Moore, C.H. (2001) Chapter 9 - Burial Diagenetic Environment, in: Moore, C.H. (Ed.), Developments in Sedimentology. Elsevier, pp. 291-340.

Moore, C.H. and Druckman, Y. (1981) Burial diagenesis and porosity evolution, upper Jurassic Smackover, Arkansas and Louisiana. AAPG Bulletin 65, 597-628

Moore, C.H. and Wade, W.J. (2013) Chapter 10 - Burial Diagenetic Environment, in: Moore, C.H., Wade, W.J. (Eds.), Developments in Sedimentology. Elsevier, pp. 239-284.

Morad, S., Al Suwaidi, M., Mansurbeg, H., Morad, D., Ceriani, A., Paganoni, M. and Al-Aasm, I. (2019) Diagenesis of a limestone reservoir (Lower Cretaceous), Abu Dhabi, United Arab Emirates: Comparison between the anticline crest and flanks. Sediment Geol 380, 127-142

Morgan, P. (1983) Constraints on Rift Thermal Processes from Heat Flow and Uplift, in: Morgan, P., Baker, B.H. (Eds.), Developments in Geotectonics. Elsevier, pp. 277-298.

Mraz, E., Wolfgramm, M., Moeck, I. and Thuro, K. (2019) Detailed Fluid Inclusion and Stable Isotope Analysis on Deep Carbonates from the North Alpine Foreland Basin to Constrain Paleofluid Evolution. Geofluids 2019, 8980794.10.1155/2019/8980794

Muller, I.A., Violay, M.E.S., Storck, J.C., Fernandez, A., van Dijk, J., Madonna, C. and Bernasconi, S.M. (2017) Clumped isotope fractionation during phosphoric acid digestion of carbonates at 70 degrees C. Chem Geol 449, 1-14. 10.1016/j.chemgeo.2016.11.030

Murphy, W. M., Oelkers, E. H., & Lichtner, P. C. (1989). Surface reaction versus diffusion control of mineral dissolution and growth rates in geochemical processes. Chemical Geology, 78(3-4), 357-380.

Nader, F., Bachaud, P. and Michel, A. (2015) Numerical modelling of fluid-rock interactions: Lessons learnt from carbonate rocks diagenesis studies, EGU General Assembly Vol 17.p. 8270. EGU2015-8270.

Naylor, H.N., Defliese, W.F., Grossman, E.L. and Maupin, C.R. (2020) Investigation of the thermal history of the Delaware Basin (West Texas, USA) using carbonate clumped isotope thermometry. Basin Res 32, 1140-1155

Neilson, J.E., Oxtoby, N.H. and Simmons, M.D. (1996) Effect of Petroleum Emplacement on Reservoir Quality in the Thamama Reservoirs of Abu Dhabi. Abu Dhabi International Petroleum Exhibition and Conference Vol 36241. https://doi.org/10.2118/36241-MS

Neilson, J.E., Oxtoby, N.H., Simmons, M.D., Simpson, I.R. and Fortunatova, N.K. (1998) The relationship between petroleum emplacement and carbonate reservoir quality: examples from Abu Dhabi and the Amu Darya Basin. Marine and Petroleum Geology 15, 57-72. https://doi.org/10.1016/S0264-8172(97)00033-0

Nelson, C.S. and Smith, A.M. (1996) Stable oxygen and carbon isotope compositional fields for skeletal and diagenetic components in New Zealand Cenozoic nontropical carbonate sediments and limestones: A synthesis and review. New Zealand Journal of Geology and Geophysics 39, 93-107.10.1080/00288306.1996.9514697

Nielsen, P., Swennen, R. and Keppens, E. (1994) Multiple-step recrystallization within massive ancient dolomite units: an example from the Dinantian of Belgium. Sedimentology 41, 567-584. https://doi.org/10.1111/j.1365-3091.1994.tb02011.x

Noufal, A., Obaid, K. and Ali, M.Y. (2016) Tectonic Map of Abu Dhabi, UAE, Abu Dhabi International Petroleum Exhibition & Conference. SPE-183108-MS https://doi.org/10.2118/183108-MS

O'Brien, C.L., Robinson, S.A., Pancost, R.D., Damste, J.S.S., Schouten, S., Lunt, D.J., Alsenz, H., Bornemann, A., Bottini, C. and Brassell, S.C. (2017) Cretaceous sea-surface temperature evolution: Constraints from TEX86 and planktonic foraminiferal oxygen isotopes. Earth-Sci Rev 172, 224-247

Obermajer, M., Stasiuk, L.D., Fowler, M.G. and Osadetz, K.G. (1997) Acritarch fluorescence as a new thermal maturity indicator. AAPG Bulletin 81, 1561

Oelkers, E., Bjorkum, P. and Murphy, W. (1992) The mechanism of porosity reduction, styolite development and quartz cementation in North Sea sandstones, International symposium on water-rock interaction, pp. 1183-1186

Oswald, E.J., Mueller, H.W., III, Goff, D.F., Al-Habshi, H. and Al-Matroushi, S. (1995) Controls On Porosity Evolution In Thamama Group Carbonate Reservoirs in Abu Dhabi. Middle East oil show and conference 9th. Vol 1, 251-265. https://doi.org/10.2118/29797-MS

Paganoni, M., Al Harthi, A., Morad, D., Morad, S., Ceriani, A., Mansurbeg, H., Al Suwaidi, A., Al-Aasm, I.S., Ehrenberg, S.N. and Sirat, M. (2016) Impact of stylolitization on diagenesis of a Lower Cretaceous carbonate reservoir from a giant oilfield, Abu Dhabi, United Arab Emirates. Sediment Geol 335, 70-92

Passey, B.H. and Henkes, G.A. (2012) Carbonate clumped isotope bond reordering and geospeedometry. Earth and Planetary Science Letters 351-352, 223-236. 10.1016/j.epsl.2012.07.021

Perkins, R.D., Dwyer, G.S., Rosoff, D.B., Fuller, J., Baker, P.A. and Lloyd, R.M. (1994) Salina Sedimentation and Diagenesis: West Caicos Island, British West Indies, Dolomites: A Volume in Honour of Dolomieu, 35-54.

Peters, K.E., Cassa, M.R., Magoon, L.B. and Dow, W.G. (1994) Applied Source Rock Geochemistry. in The Petroleum System—From Source to Trap. American Association of Petroleum Geologists Memoir 60. 93-117.

Petersen, S.V., Defliese, W.F., Saenger, C., Daëron, M., Huntington, K.W., John, C.M., Kelson, J.R., Bernasconi, S.M., Colman, A.S., Kluge, T., Olack, G.A., Schauer, A.J., Bajnai, D., Bonifacie, M., Breitenbach, S.F.M., Fiebig, J., Fernandez, A.B., Henkes, G.A., Hodell, D., Katz, A., Kele, S., Lohmann, K.C., Passey, B.H., Peral, M.Y., Petrizzo, D.A., Rosenheim, B.E., Tripati, A., Venturelli, R., Young, E.D. and Winkelstern, I.Z. (2019) Effects of Improved 17O Correction on Interlaboratory Agreement in Clumped Isotope Calibrations, Estimates of Mineral-Specific Offsets, and Temperature Dependence of Acid Digestion Fractionation. Geochemistry, Geophysics, Geosystems 20, 3495-3519.10.1029/2018gc008127

Petersen, S. V., & Schrag, D. P. (2014). Clumped isotope measurements of small carbonate samples using a high-efficiency dual-reservoir technique. Rapid Communications in Mass Spectrometry, 28(21), 2371-2381.

Petersen, S.V., Winkelstern, I.Z., Lohmann, K.C. and Meyer, K.W. (2016) The effects of Porapak (TM) trap temperature on delta O-18, delta C-13, and Delta(47) values in preparing samples for clumped isotope analysis. Rapid Commun Mass Sp 30, 199-208. 10.1002/rcm.7438

Pike, S., Dewison, M.G. and Spears, D.A. (1989) Sources of Error in Low-Temperature Plasma Ashing Procedures for Quantitative Mineral Analysis of Coal Ash. Fuel 68, 664-668. Doi 10.1016/0016-2361(89)90170-1

Pytte, A. and Reynolds, R. (1989) The thermal transformation of smectite to illite, Thermal history of sedimentary basins. Springer, pp. 133-140.

Quade, J., Leary, R., Dettinger, M.P., Orme, D., Krupa, A., DeCelles, P.G., Kano, A., Kato, H., Waldrip, R., Huang, W. and Kapp, P. (2020) Resetting Southern Tibet: The serious challenge of obtaining primary records of Paleoaltimetry. Global Planet Change 191, 103194. https://doi.org/10.1016/j.gloplacha.2020.103194

Ramm, M. (1992) Porosity-depth trends in reservoir sandstones: theoretical models related to Jurassic sandstones offshore Norway. Marine and Petroleum Geology 9, 553-567. https://doi.org/10.1016/0264-8172(92)90066-N

Reeder, R.J. (2000) Constraints on Cation Order in Calcium-rich Sedimentary Dolomite. Aquat Geochem 6, 213-226.10.1023/A:1009659122772

Reeder, R.J. and Wenk, H.-R. (1983) Structure refinements of some thermally disordered dolomites. Am Mineral 68, 769-776

Reid, R.P. and Macintyre, I.G. (1998) Carbonate recrystallization in shallow marine environments: a widespread diagenetic process forming micritized grains. J Sediment Res 68, 928-946

Reid, R.P., Macintyre, I.G. and Post, J.E. (1992) Micritized skeletal grains in northern Belize Lagoon; a major source of Mg-calcite mud. J Sediment Res 62, 145-156

Reinhold, C. (1998) Multiple episodes of dolomitization and dolomite recrystallization during shallow burial in Upper Jurassic shelf carbonates: eastern Swabian Alb, southern Germany. Sediment Geol 121, 71-95. https://doi.org/10.1016/S0037-0738(98)00077-3

Ries, A.C. and Shackleton, R.M. (1990) Structures in the Huqf-Haushi Uplift, east Central Oman. Geological Society, London, Special Publications 49, 653. 10.1144/GSL.SP.1992.049.01.39

Roberts, L.R., Holmes, J.A., Leng, M.J., Sloane, H.J. and Horne, D.J. (2018) Effects of cleaning methods upon preservation of stable isotopes and trace elements in shells of Cyprideis torosa (Crustacea, Ostracoda): Implications for palaeoenvironmental reconstruction. Quaternary Sci Rev 189, 197-209. 10.1016/j.quascirev.2018.03.030

Robertson, E.C. (1988) Thermal properties of rocks, Open-File Report, - ed. USGS Numbered Series number 88-441, 10-71. https://doi.org/10.3133/ofr88441

Robison, C.R., van Gijzel, P. and Darnell, L.M. (2000) The transmittance color index of amorphous organic matter: a thermal maturity indicator for petroleum source rocks. Int J Coal Geol 43, 83-103.https://doi.org/10.1016/S0166-5162(99)00055-5

Roedder, E. and Bodnar, R.J. (1980) Geologic Pressure Determinations from Fluid Inclusion Studies. Annual Review of Earth and Planetary Sciences 8, 263-301. 10.1146/annurev.ea.08.050180.001403

Rosales, I., Robles, S. and Quesada, S. (2004) Elemental and Oxygen Isotope Composition of Early Jurassic Belemnites: Salinity vs. Temperature Signals. J Sediment Res 74, 342-354. 10.1306/112603740342

Rosen, M.R., Miser, D.E. and Warren, J.K. (1988) Sedimentology, mineralogy and isotopic analysis of Pellet Lake, Coorong region, South Australia. Sedimentology 35, 105-122. https://doi.org/10.1111/j.1365-3091.1988.tb00907.x

Rosenbaum, J. and Sheppard, S.M.F. (1986) An isotopic study of siderites, dolomites and ankerites at high temperatures. Geochimica et Cosmochimica Acta 50, 1147-1150. https://doi.org/10.1016/0016-7037(86)90396-0

Rousseau, M., Dromart, G., Garcia, J.-P., Atrops, F. and Guillocheau, F. (2005) Jurassic evolution of the Arabian carbonate platform edge in the central Oman mountains. J Geol Soc London 162, 349-362

Royse, C.F., Wadell, J.S. and Petersen, L.E. (1971) X-ray determination of calcite-dolomite; an evaluation. J Sediment Res 41, 483-488. 10.1306/74d722a7-2b21-11d7-8648000102c1865d

Ryb, U. and Eiler, J.M. (2018) Oxygen isotope composition of the Phanerozoic ocean and a possible solution to the dolomite problem. Proceedings of the National Academy of Sciences 115, 6602-6607

Ryb, U., Lloyd, M.K. and Eiler, J.M. (2021) Carbonate clumped isotope constraints on burial, uplift and exhumation histories of the Colorado Plateau. Earth and Planetary Science Letters 566, 116964. https://doi.org/10.1016/j.epsl.2021.116964

Ryb, U., Lloyd, M.K., Stolper, D.A. and Eiler, J.M. (2017) The clumped-isotope geochemistry of exhumed marbles from Naxos, Greece. Earth and Planetary Science Letters 470, 1-12. 10.1016/j.epsl.2017.04.026

Saddiqi, O., Michard, A., Goffe, B., Poupeau, G.r. and Oberhänsli, R. (2006) Fission-track thermochronology of the Oman Mountains continental windows, and current problems of tectonic interpretation. Bulletin de la Société Géologique de France 177, 127-134. 10.2113/gssgfbull.177.3.127

Sakai, R., Kusakabe, M., Noto, M. and Ishii, T. (1990) Origin of waters responsible for serpentinization of the Izu-Ogasawara-Mariana forearc seamounts in view of hydrogen and oxygen isotope ratios. Earth and Planetary Science Letters 100, 291-303. https://doi.org/10.1016/0012-821X(90)90192-Z

Sattler, U.T.E., Immenhauser, A., HillgÄRtner, H. and Esteban, M. (2005) Characterization, lateral variability and lateral extent of discontinuity surfaces on a Carbonate Platform (Barremian to Lower Aptian, Oman). Sedimentology 52, 339-361. https://doi.org/10.1111/j.1365-3091.2005.00701.x

Schmoker, J.W. and Halley, R.B. (1982) Carbonate porosity versus depth: a predictable relation for south Florida. AAPG Bulletin 66, 2561-2570

Schmoker, J.W., Krystinik, K.B. and Halley, R.B. (1985) Selected characteristics of limestone and dolomite reservoirs in the United States. Aapg Bull 69, 733-741

Scholle, P.A. and Halley, R.B. (1989) Burial Diagenesis: Out of Sight, Out of Mind! Carbonate Sedimentology and Petrology, 135-160. https://doi.org/10.1029/SC004p0135

Scholle, P.A. and Ulmer-Scholle, D.S. (2003) Carbonate Diagenesis: Meso- and Telogenetic Burial Diagenesis, in: Scholle, P.A., Ulmer-Scholle, D.S. (Eds.), A Color Guide to the Petrography of Carbonate Rocks: Grains, textures, porosity, diagenesis. American Association of Petroleum Geologists, 77: 1-486. https://doi.org/10.1306/M77973

Schön, J. H. (2015). Pore space properties. In Developments in Petroleum Science. Elsevier. Vol. 65. pp. 21-84.

Schütz, F., Winterleitner, G. and Huenges, E. (2018) Geothermal exploration in a sedimentary basin: new continuous temperature data and physical rock properties from northern Oman. Geothermal Energy 6(1), 1-23. 10.1186/s40517-018-0091-6

Searle, M. and Cox, J. (1999) Tectonic setting, origin, and obduction of the Oman ophiolite. GSA Bulletin 111, 104-122.

Searle, M.P., Cherry, A.G., Ali, M.Y. and Cooper, D.J.W. (2014) Tectonics of the Musandam Peninsula and northern Oman Mountains: From ophiolite obduction to continental collision. Geoarabia 19, 135-174

Sena, C.M., John, C.M., Jourdan, A.L., Vandeginste, V. and Manning, C. (2014) Dolomitization of Lower Cretaceous Peritidal Carbonates by Modified Seawater: Constraints from Clumped Isotopic Paleothermometry, Elemental Chemistry, and Strontium Isotopes. J Sediment Res 84, 552-566. 10.2110/jsr.2014.45

Shenton, B.J., Grossman, E.L., Passey, B.H., Henkes, G.A., Becker, T.P., Laya, J.C., Perez-Huerta, A., Becker, S.P. and Lawson, M. (2015) Clumped isotope thermometry in deeply buried sedimentary carbonates: The effects of bond reordering and recrystallization. Geol Soc Am Bull 127, 1036-1051. 10.1130/B31169.1

Sheppard, S. (1984) Stable isotope studies of formation waters and associated Pb-Zn hydrothermal ore deposits. Thermal Phenomena in Sedimentary Basins. Technip, Paris, 301-303

Sheppard, S.M.F. (1986) Characterization and isotopic variations in natural waters. Reviews in Mineralogy and Geochemistry 16, 165-183

Simon, L., Lécuyer, C. and Putelat, T. (2017) The calculation of water-rock ratios using trace element (Li, B) stable isotopes. Annales Universitatis Mariae Curie-Sklodowska. sectio AAA – Physica Vol 71, 79. http://dx.doi.org/10.17951/aaa.2016.71.79

Sirat, M., Al-Aasm, I.S., Morad, S., Aldahan, A., Al-Jallad, O., Ceriani, A., Morad, D., Mansurbeg, H. and Al-Suwaidi, A. (2016) Saddle dolomite and calcite cements as records of fluid flow during basin evolution: Paleogene carbonates, United Arab Emirates. Marine and Petroleum Geology 74, 71-91. https://doi.org/10.1016/j.marpetgeo.2015.11.005

Skelton, P. (2018) Introduction to the Hippuritida (rudists): Shell structure, anatomy, and evolution. Treatise Online, 104, 1-37.

Snell, K.E., Thrasher, B.L., Eiler, J.M., Koch, P.L., Sloan, L.C. and Tabor, N.J. (2013) Hot summers in the Bighorn Basin during the early Paleogene. Geology 41, 55-58

Staplin, F.L. (1969) Sedimentary organic matter, organic metamorphism, and oil and gas occurrence. Bulletin of Canadian Petroleum Geology 17, 47-66. 10.35767/gscpgbull.17.1.047

Staudigel, P.T. and Swart, P.K. (2016) Isotopic behavior during the aragonite-calcite transition: Implications for sample preparation and proxy interpretation. Chemical Geology 442. 130-138. 10.1016/j.chemgeo.2016.09.013

Stevens, G.R. and Clayton, R.N. (1971) Oxygen isotope studies on Jurassic and Cretaceous belemnites from New Zealand and their biogeographic significance. New Zealand Journal of Geology and Geophysics 14, 829-897.10.1080/00288306.1971.10426336

Stoessell, R.K. and Moore, C.H. (1983) Chemical Constraints and Origins of Four Groups of Gulf Coast Reservoir Fluids1. Aapg Bull 67, 896-906. 10.1306/03B5B6C8-16D1-11D7-8645000102C1865D

Stolper, D.A. and Eiler, J.M. (2015) The Kinetics of Solid-State Isotope-Exchange Reactions for Clumped Isotopes: A Study of Inorganic Calcites and Apatites from Natural and Experimental Samples. Am J Sci 315, 363-411. 10.2475/05.2015.01

Stolper, D.A., Eiler, J.M. and Higgins, J.A. (2018) Modeling the effects of diagenesis on carbonate clumped-isotope values in deep-and shallow-water settings. Geochimica et Cosmochimica Acta 227, 264-291

Swanson, E.M., Wernicke, B.P., Eiler, J.M. and Losh, S. (2012) Temperatures and Fluids on Faults Based on Carbonate Clumped-Isotope Thermometry. Am J Sci 312, 1-21. 10.2475/01.2012.01

Swart, P. K., Burns, S. J., & Leder, J. J. (1991). Fractionation of the stable isotopes of oxygen and carbon in carbon dioxide during the reaction of calcite with phosphoric acid as a function of temperature and technique. Chemical Geology: Isotope Geoscience section, 86(2), 89-96.

Sweeney, J.J. and Burnham, A.K. (1990) Evaluation of a simple model of vitrinite reflectance based on chemical kinetics. AAPG Bulletin 74, 1559-1570

Tagami, T., Galbraith, R.F., Yamada, R. and Laslett, G.M. (1998) Revised Annealing Kinetics of Fission Tracks in Zircon and Geological Implications, in: van den Haute, P., de Corte, F. (Eds.), Advances in Fission-Track Geochronology: A selection of papers presented at the International Workshop on Fission-Track Dating, Ghent, Belgium, 1996. Springer Netherlands, Dordrecht, pp. 99-112.

Taher, A.A. (1996) Delineation of Organic Richness and Thermal History of the Lower Cretaceous Thamama Group, East Abu Dhabi: A Modeling Approach for Oil Exploration, GeoArabia 2 (1), 65–88. 10.2118/36277-MS^

Taylor, H.P. (1978) Oxygen and hydrogen isotope studies of plutonic granitic rocks. Earth and Planetary Science Letters 38, 177-210. https://doi.org/10.1016/0012-821X(78)90131-0

Taylor Jr, H. (1977) Water/rock interactions and the origin of H2O in granitic batholiths: Thirtieth William Smith lecture. Journal of the Geological Society, 133(6), 509-558.

Thompson-Rizer, C.L., Woods, R.A. and Ottenjann, K. (1988) Quantitative fluorescence results from sample exchange studies. Organic geochemistry, 12(4), 323-332.

Tissot, B., Pelet, R. and Ungerer, P. (1987) Thermal history of sedimentary basins, maturation indices, and kinetics of oil and gas generation. AAPG Bulletin 71, 1445-1466

Vahrenkamp, V., Barata, J., Van Laer, P.J., Swart, P. and Murray, S. (2014) Micro Rhombic Calcite of a Giant Barremian (Thamama B) Reservoir Onshore Abu Dhabi - Clumped Isotope Analyses Fix Temperature, Water Composition and Timing of Burial Diagenesis. Abu Dhabi International Petroleum Exhibition and Conference. SPE-172033-MS. 1-12. https://doi.org/10.2118/172033-MS

van Buchem, F.S., Pittet, B., Hillgärtner, H., Grötsch, J., Al Mansouri, A.I., Billing, I.M., Droste, H.H., Oterdoom, W.H. and van Steenwinkel, M. (2002a) High-resolution sequence stratigraphic architecture of Barremian/Aptian carbonate systems in northern Oman and the United Arab Emirates (Kharaib and Shu'aiba formations). Geoarabia 7, 461-500

van Buchem, F.S.P., Al-Husseini, M.I., Maurer, F., Droste, H.J. and Yose, L.A. (2010) Sequence-stratigraphic synthesis of the Barremian – Aptian of the eastern Arabian Plate and implications for the petroleum habitat, in: van Buchem, F.S.P., Al-Husseini, M.I., Maurer, F., Droste, H.J. (Eds.), Barremian – Aptian Stratigraphy and Hydrocarbon Habitat of the Eastern Arabian Plate (vol. 1). GeoArabia Special Publication 4, 2010, v. 1, p. 9-48

van Buchem, F.S.P., Pittet, B., Hillgärtner, H., Grötsch, J., Al Mansouri, A.I., Billing, I.M., Droste, H.H.J., Oterdoom, W.H. and van Steenwinkel, M. (2002b) High-resolution Sequence Stratigraphic Architecture of Barremian/Aptian Carbonate Systems in Northern Oman and the United Arab Emirates (Kharaib and Shu'aiba Formations). Geoarabia 7, 461-500

Van Simaeys, S., Rendall, B., Lucia, F.J., Kerans, C. and Fullmer, S. (2017) Facies-independent reservoir characterization of the micropore-dominated Word field (Edwards Formation), Lavaca County, Texas. AAPG Bulletin 101, 73-94. 10.1306/06101616034

Vandeginste, V. and John, C.M. (2012) Influence of climate and dolomite composition on dedolomitization: insights from a multi-proxy study in the central Oman Mountains. J Sediment Res 82, 177-195.10.2110/jsr.2012.19

Vandeginste, V., John, C.M., Cosgrove, J.W. and Manning, C. (2014) Dimensions, texture-distribution, and geochemical heterogeneities of fracture- related dolomite geobodies hosted in Ediacaran limestones, northern Oman. AAPG Bulletin 98, 1789-1809. 10.1306/05121413127

Vandeginste, V., John, C.M., van de Flierdt, T. and Cosgrove, J.W. (2013) Linking process, dimension, texture, and geochemistry in dolomite geobodies: A case study from Wadi Mistal (northern Oman). Aapg Bull 97, 1181-1207. 10.1306/11011212076

Vandeginste, V., Stehle, M.C., Jourdan, A.-L., Bradbury, H.J., Manning, C. and Cosgrove, J.W. (2017) Diagenesis in salt dome roof strata: Barite - calcite assemblage in Jebel Madar, Oman. Marine and Petroleum Geology 86, 408-425. https://doi.org/10.1016/j.marpetgeo.2017.06.008

Veillard, C.M.A., John, C.M., Krevor, S. and Najorka, J. (2019) Rock-buffered recrystallization of Marion Plateau dolomites at low temperature evidenced by clumped isotope thermometry and X-ray diffraction analysis. Geochimica Et Cosmochimica Acta 252, 190-212. 10.1016/j.gca.2019.02.012

Von Der Borch, C.C. and Jones, J.B. (1976) Spherular modern dolomite from the Coorong area, South Australia. Sedimentology 23, 587-591. https://doi.org/10.1111/j.1365-3091.1976.tb00070.x

Walderhaug, O. (1990) A fluid inclusion study of quartz-cemented sandstones from offshore mid-Norway; possible evidence for continued quartz cementation during oil emplacement. Journal of Sedimentary Research, 60(2), 203-210.

Waples, D.W. (1982) Time and Temperature in Petroleum Formation: Application of Lopatin's Method to Petroleum Exploration. AAPG Bulletin 66, 1152-1152.

Waples, D.W. (2001) A New Model for Heat Flow in Extensional Basins: Radiogenic Heat, Asthenospheric Heat, and the McKenzie Model. Natural Resources Research 10, 227-238. 10.1023/A:1012521309181

Warburton, J., Burnhill, T., Graham, R. and Isaac, K. (1990) The evolution of the Oman Mountains foreland basin. Geological Society, London, Special Publications 49, 419-427

Wheildon, J., Morgan, P., Williamson, K.H., Evans, T.R. and Swanberg, C.A. (1994) Heat flow in the Kenya rift zone. Tectonophysics 236, 131-149. https://doi.org/10.1016/0040-1951(94)90173-2

Wierzbowski, H. (2007) Effects of pre-treatments and organic matter on oxygen and carbon isotope analyses of skeletal and inorganic calcium carbonate. Int J Mass Spectrom 268, 16-29. DOI 10.1016/j.ijms.2007.08.002

Winkelstern, I.Z. and Lohmann, K.C. (2016) Shallow burial alteration of dolomite and limestone clumped isotope geochemistry. Geology 44, 467-470

Worden, R.H. and Heasley, E.C. (2000) Effects of petroleum emplacement on cementation in carbonate reservoirs. Bulletin de la Societe geologique de France 171, 607-620

Worden, R.H., Heasley, E.C. and Barclay, S.A. (1999) The effects of petroleum emplacement on diagenesis : a comparison between sandstone and carbonate reservoirs. Sciences Géologiques, bulletins et mémoires, 149-153

Worden, R. H., Oxtoby, N. H., & Smalley, P. C. (1998). Can oil emplacement prevent quartz cementation in sandstones?. Petroleum Geoscience, 4(2), 129-137.

Xiong, Z., Ding, L., Spicer, R.A., Farnsworth, A., Wang, X., Valdes, P.J., Su, T., Zhang, Q., Zhang, L., Cai, F., Wang, H., Li, Z., Song, P., Guo, X. and Yue, Y. (2020) The early Eocene rise of the Gonjo Basin, SE Tibet: From low desert to high forest. Earth and Planetary Science Letters 543, 116312. https://doi.org/10.1016/j.epsl.2020.116312

Yamamoto, K., Ottinger, G., Zinati, O.A., Takayanagi, H., Yamamoto, K. and Iryu, Y. (2018) Geochemical, petrographical, and petrophysical evaluations of a

heterogeneous, stratiform dolomite from a Barremian oil field, offshore Abu Dhabi (United Arab Emirates). Aapg Bull 102, 129-152. 10.1306/0327171524717016

Appendix A.

XRD data, Chapter 5

Sample Name	MgCO3 %mole	Dol:Cal	Dolomite ordering	Comments
MPA 35	51.1	1.00	0.58	
AK-27	51.2	0.98	0.56	
AK-25	51.6	1.00	0.79	
AK-24	51.1	1.00	0.71	
AK-23	51.1	1.00	0.69	
AK-22	50.8	1.00	0.46	
M-5*	46.9	0.82	0.51	This samples has two dol104 peaks, * higher intensity
M-5	49.8	0.82	0.51	
M-8	50.7	0.32	0.63	
M-9	47.0	0.94	0.40	This samples has two dol104 peaks, * higher intensity
M-9*	50.3	0.94	0.40	
M-10	50.4	0.98	0.37	
M-31*	46.6	0.46	0.40	This samples has two dol104 peaks, * higher intensity
M-31	49.7	0.46	0.40	
453_Gray		0.0%		
453_SK		0.0%	0.52	
526_RED	50.65	11.7%		
I5	51.04	100.0%	0.48	
MPA 34	51.08	100.0%	0.53	
MPA-11A	45.36	6.6%		
MPA-11BG		0.0%	0.61	
MPA-12 AG	50.54	93.1%		
MPA-12AA		0.0%		
MPA-24	49.82	87.7%	0.38	
WBH_25	50.91	100.0%	TLTD	Too Low To Detect
WN625_Gray		0.0%		
WN625_red	50.18	30.6%		
WN627		0.0%		
WSNE_MAT	46.41	100.0%	0.79	
WSNE_WC	49.36	100.0%	0.65	
WSNE_WCPU	50.06	10.5%		
Z9484_M		0.0%	0.45	
Z9684	45.43	3.0%		
Zg484_R		0.0%		
Zg652	51.30	82.8%		
Zg653	51.02	91.4%		
526_GR MAT		0.0%		
E37	50.84	83.7%		

Appendix.B.

Clumped Isotope Data

Chapter 3

	ID	d13C VPDB	d18O VPDB	D47 CDES	d18O VSMOW	D48 Offset	49 Param
S1	A-JMF6A						
R1	2018-08-28 20:20 BST	-7.95	-15.17	0.572	15.28	0.382	-0.074
R2	2018-08-29 12:12 BST	-7.84	-15.09	0.601	15.36	0.646	-0.013
R3	2018-09-05 15:31 BST	-7.93	-15.18	0.581	15.27	0.304	-0.024
S2	B-JMF6A						
R1	2018-08-27 20:28 BST	-7.86	-14.93	0.488	15.53	-0.427	-0.064
R2	2018-08-29 15:22 BST	-7.8	-14.84	0.589	15.62	0.65	-0.082
R3	2018-08-30 16:34 BST	-7.82	-14.85	0.57	15.61	0.623	-0.142
S3	C-JMF6A						
R1	2018-08-27 17:57 BST	-7.93	-15.03	0.47	15.43	-0.77	-0.171
R2	2018-08-28 16:30 BST	-7.61	-14.47	0.515	16	0.291	0.015
R3	2018-08-29 22:22 BST	-7.76	-14.95	0.524	15.51	0.464	0.034
S4	ICM-OPA10-3X						
R1	2019-03-14 02:32 GMT	2.07	-1.86	0.286	29.01	-0.137	0.238
R2	2019-03-14 11:25 GMT	2.08	-1.8	0.316	29.06	0.04	0.167
R3	2019-03-16 16:33 GMT	2.08	-1.94	0.295	28.92	-0.036	0.2
R4	2019-03-17 01:15 GMT	2.1	-1.92	0.318	28.95	0.018	0.209
R5	2019-03-19 11:28 GMT	2.05	-1.9	0.282	28.96	-0.085	0.195
R6	2019-03-22 08:15 GMT	2.04	-1.96	0.277	28.9	-0.314	0.211
R7	2019-03-28 04:37 GMT	2.08	-1.85	0.3	29.01	-0.122	0.196
R8	2019-04-13 21:59 BST	2.02	-1.99	0.325	28.86	-0.077	0.241
R9	2019-07-18 02:27 BST						
S5	ICM-OPA10-6X-NotStirred						
R1	2019-03-28 02:26 GMT	2.06	-1.85	0.319	29.01	-0.116	0.19
R2	2019-03-31 16:00 BST	2.06	-1.91	0.326	28.95	-0.056	0.198
R3	2019-04-02 07:54 BST	2.06	-1.8	0.316	29.06	-0.147	0.179
R4	2019-04-02 22:34 BST	2.05	-1.8	0.327	29.07	-0.12	0.209
R5	2019-05-04 19:17 BST	2.05	-1.84	0.307	29.03	-0.088	0.171
R6	2019-07-16 03:11 BST						
R7	2019-07-26 19:38 BST						
S6	ICM-OPA10-6X-Stirred						
R1	2019-04-10 01:22 BST	1.99	-2.12	0.298	28.73	-0.14	0.241
R2	2019-04-23 09:45 BST	2.06	-1.85	0.331	29.01	0.231	0.188
R3	2019-05-04 12:39 BST	2.07	-1.86	0.303	29.01	-0.119	0.148
R4	2019-07-16 11:42 BST						
R5	2019-07-18 04:33 BST						
R6	2019-07-26 17:25 BST						
S7	ICM-OPA30						
R1	2019-01-30 08:26 GMT	2.08	-1.89	0.33	28.98	-0.069	0.205
R2	2019-03-14 00:28 GMT	2.04	-1.85	0.348	29.01	0.057	0.201
R3	2019-03-14 07:01 GMT	2.08	-1.84	0.317	29.02	0.041	0.198
R4	2019-03-15 16:40 GMT	2.06	-2.02	0.301	28.84	0.055	0.205

R5	2019-03-15 23:23 GMT	1.97	-2.12	0.336	28.74	0.104	0.176
R6	2019-03-24 16:00 GMT	2.06	-1.84	0.309	29.02	-0.234	0.22
R7	2019-04-02 16:20 BST	2.07	-1.78	0.316	29.09	0.033	0.178
S8	ICM_20X20						
R1	2019-05-04 10:17 BST	2.06	-1.89	0.277	28.97	-0.24	0.169
R2	2019-05-05 04:19 BST	2.07	-1.89	0.252	28.98	-0.245	0.172
R3	2019-05-09 05:44 BST	2.06	-1.86	0.315	29.01	-0.044	0.194
R4	2019-05-09 14:28 BST	2.06	-1.86	0.34	29	0.149	0.18
R5	2019-07-17 15:40 BST						
R6	2019-07-26 01:18 BST						
R7	2019-08-10 12:08 BST						
S9	ICM_2C						
R1	2019-03-25 02:54 GMT	1.86	-2.14	0.309	28.71	-0.277	0.254
R2	2019-04-01 23:34 BST	1.78	-2.31	0.293	28.54	-0.192	0.163
R3	2019-04-02 14:13 BST	2.06	-1.78	0.32	29.08	-0.082	0.19
S10	IOL-OPA10						
R1	2018-11-16 15:56 GMT	0.13	0.46	0.599	31.39	-0.417	0.085
R2	2019-01-17 19:12 GMT	0.36	0.43	0.627	31.37	0.146	0.119
R3	2019-01-18 08:12 GMT	0.3	0.49	0.64	31.42	0.166	0.117
R4	2019-01-18 21:25 GMT	0.29	0.38	0.613	31.31	0.307	0.126
R5	2019-01-22 15:30 GMT	0.29	0.29	0.659	31.22	0.225	0.166
R6	2019-01-22 21:59 GMT	0.26	0.25	0.641	31.18	0.197	0.159
R7	2019-02-09 14:24 GMT	0.34	0.35	0.597	31.28	0	0.129
R8	2019-04-03 00:58 BST	0.3	0.45	0.646	31.38	-0.034	0.199
R9	2019-04-13 15:47 BST	0.25	0.35	0.632	31.28	0.07	0.269
R10	2019-05-05 06:52 BST	0.29	0.41	0.635	31.35	-0.08	0.158
S11	IOL-OPA20						
R1	2018-11-08 18:36 GMT	0.29	0.46	0.635	31.4	-0.115	0.188
R2	2019-01-18 17:07 GMT	0.27	0.27	0.619	31.2	0.272	0.123
R3	2019-01-19 01:47 GMT	0.32	0.34	0.629	31.27	0.354	0.159
R4	2019-01-19 08:40 GMT	0.32	0.32	0.618	31.25	0.396	0.136
R5	2019-01-22 04:11 GMT	0.34	0.31	0.665	31.24	0.269	0.124
R6	2019-01-23 11:27 GMT	0.3	0.33	0.651	31.26	0.312	0.19
R7	2019-01-27 02:04 GMT	0.33	0.32	0.631	31.25	0.173	0.213
R8	2019-01-30 13:02 GMT	0.33	0.38	0.622	31.31	0.118	0.184
R9	2019-04-13 09:39 BST	0.24	0.32	0.612	31.25	-0.049	0.26
R10	2019-07-16 20:39 BST						
S12	IOL-OPA30						
R1	2018-09-25 17:28 BST	0.38	0.39	0.632	31.33	-0.005	0.104
R2	2018-10-17 22:23 BST	0.36	0.43	0.668	31.36	-0.205	-0.025
R3	2018-10-24 14:17 BST	0.35	0.65	0.652	31.59	-0.085	0.197
R4	2019-01-18 06:07 GMT	0.36	0.43	0.617	31.37	0.084	0.116
R5	2019-01-22 08:43 GMT	0.32	0.32	0.667	31.25	0.187	0.182
R6	2019-01-23 02:31 GMT	0.28	0.3	0.671	31.23	0.33	0.184
R7	2019-04-13 01:23 BST	0.3	0.34	0.61	31.27	0.023	0.233
R8	2019-07-27 19:03 BST						
R9	2019-08-10 16:25 BST						
R10	2019-08-17 19:38 BST						
S13	JC10						
R1	2019-03-22 06:05 GMT	-7.81	-14.74	0.516	15.73	-0.129	0.139

R2	2019-03-22 14:53 GMT	-7.79	-14.6	0.5	15.87	-0.173	0.151
R3	2019-03-24 00:33 GMT	-7.86	-14.73	0.48	15.73	-0.289	0.169
S14	JMF6A-OPA10						
R1	2018-11-16 11:48 GMT	-7.93	-14.09	0.519	16.39	-0.205	0.016
R2	2018-11-21 21:19 GMT	-7.68	-15.2	0.701	15.25	-11.165	-1.791
R3	2019-01-17 21:27 GMT	-7.88	-14.66	0.531	15.81	-0.144	0.01
R4	2019-01-18 14:56 GMT	-7.84	-14.72	0.534	15.74	-0.024	0.037
R5	2019-01-19 18:25 GMT	-7.87	-14.75	0.542	15.72	0.135	0.077
R6	2019-01-22 17:38 GMT	-7.85	-14.84	0.566	15.62	0.13	0.126
R7	2019-01-27 06:36 GMT	-7.92	-14.75	0.55	15.71	0.055	0.134
R8	2019-04-12 23:16 BST	-7.87	-14.85	0.531	15.61	-0.016	0.234
R9	2019-05-04 23:42 BST	-7.83	-14.74	0.507	15.73	-0.117	0.109
S15	JMF6A-OPA20						
R1	2018-11-08 15:35 GMT	-8.02	-14.79	0.559	15.67	0.166	0.284
R2	2019-01-17 23:32 GMT	-7.84	-14.64	0.526	15.82	-0.112	0.021
R3	2019-01-18 23:38 GMT	-7.9	-14.73	0.497	15.73	0.05	0.071
R4	2019-01-22 13:08 GMT	-7.82	-14.75	0.569	15.71	0.044	0.106
R5	2019-01-26 21:35 GMT	-7.96	-14.7	0.517	15.76	0.042	0.096
R6	2019-01-30 10:42 GMT	-7.85	-14.74	0.546	15.73	0.166	0.114
R7	2019-04-01 21:22 BST	-7.88	-14.82	0.514	15.64	-0.036	0.105
R8	2019-04-13 07:28 BST	-7.91	-14.76	0.52	15.71	-0.081	0.206
R9	2019-07-26 13:07 BST						
S16	JMF6A-OPA30						
R1	2018-09-12 16:33 BST	-7.53	-14.56	0.586	15.91	0.577	0.107
R2	2018-09-25 20:52 BST	-7.71	-14.5	0.532	15.97	0.162	0.035
R3	2018-10-24 18:05 BST	-7.87	-14.51	0.527	15.97	-0.385	-0.181
R4	2018-11-07 17:41 GMT	-7.51	-13.94	0.579	16.55	0.419	0.186
R5	2018-11-08 12:19 GMT	-7.8	-14.39	0.556	16.09	0.193	0.128
R6	2019-01-19 10:51 GMT	-7.9	-14.72	0.53	15.75	0.093	0.077
R7	2019-01-22 06:35 GMT	-7.89	-14.78	0.541	15.69	0.121	0.092
R8	2019-01-23 16:00 GMT	-7.85	-14.73	0.545	15.74	0.106	0.13
R9	2019-04-13 17:55 BST	-7.88	-14.8	0.567	15.66	0.053	0.206
R10	2019-05-04 14:51 BST	-7.65	-14.55	0.515	15.92	-0.07	0.13
R11	2019-05-09 10:26 BST	-7.82	-14.71	0.603	15.75	0.181	0.133

Chapter 4

	ID	d13C VPDB	d18O VPDB	D47 CDES	d18O VSMOW	D48 Offset	49 Param
S1	K89220_M	2.57	-7.47	0.447	23.22		
R1	2019-08-03 05:04 BST	2.59	-7.59	0.434	23.1	-0.081	0.216
R2	2019-08-09 10:26 BST	2.51	-7.44	0.451	23.25	-0.03	0.212
R3	2019-08-15 13:49 BST	2.62	-7.42	0.443	23.27	-0.104	0.239
R4	2019-08-17 15:19 BST	2.55	-7.43	0.461	23.26	0.053	0.223
S2	K89220_Sk	2.57	-7.14	0.463	23.56		
R1	2019-08-03 03:03 BST	2.5	-7.37	0.453	23.33	-0.039	0.235

R2	2019-08-09 06:11 BST	2.57	-7.01	0.471	23.69	-0.089	0.224
R3	2019-08-15 09:30 BST	2.62	-7.04	0.465	23.66	-0.019	0.2
S3	L90004_M	2.82	-7.29	0.454	23.41		
R1	2019-08-03 09:24 BST	2.8	-7.46	0.445	23.23	0.013	0.2
R2	2019-08-09 14:42 BST	2.8	-7.11	0.469	23.59	0.072	0.25
R3	2019-08-15 16:05 BST	2.85	-7.3	0.448	23.4	-0.052	0.206
S4	L90088_M	3.46	-7.72	0.47	22.96		
R1	2019-08-24 23:16 BST	3.41	-7.75	0.45	22.93	0.008	0.324
R2	2019-09-04 04:23 BST	3.41	-7.58	0.436	23.1	-0.246	0.178
R3	2020-01-29 11:21 GMT	3.55	-7.83	0.524	22.85	-0.451	0.184
S5	L90088_Sk	2.84	-6.81	0.479	23.9		
R1	2019-08-25 03:55 BST	2.86	-6.72	0.508	23.99	0.085	0.293
R2	2019-09-04 09:11 BST	2.84	-6.88	0.486	23.83	-0.097	0.199
R3	2020-01-11 10:06 GMT	2.83	-6.83	0.441	23.87	0.618	0.364
S6	L90088_WSK	3.51	-8.98	0.453	21.66		
R1	2019-08-24 20:59 BST	3.54	-8.88	0.475	21.77	0.035	0.277
R2	2019-09-04 02:20 BST	3.5	-9.16	0.432	21.47	-0.293	0.176
R3	2020-01-11 12:21 GMT	3.51	-8.89	0.453	21.75	-0.048	0.411
S7	M92641_M	3.18	-6.73	0.463	23.98		
R1	2019-08-02 22:49 BST	3.15	-6.78	0.461	23.93	-0.041	0.244
R2	2019-08-09 03:59 BST	3.19	-6.7	0.459	24.01	-0.051	0.224
R3	2019-08-15 07:13 BST	3.2	-6.71	0.47	24	-0.115	0.242
S8	M92836_Rd	3.18	-7.23	0.473	23.47		
R1	2019-08-02 20:43 BST	3.21	-7.31	0.454	23.39	-0.082	0.217
R2	2019-08-08 23:33 BST	3.19	-7.21	0.494	23.49	-0.145	0.24
R3	2019-08-15 02:54 BST	3.18	-7.18	0.455	23.51	-0.003	0.193
R4	2019-08-17 13:14 BST	3.12	-7.22	0.49	23.48	0.023	0.211
S9	N97205_M	2.26	-5.22	0.487	25.54		
R1	2019-08-25 10:31 BST	2.26	-5.14	0.502	25.62	0.138	0.279
R2	2019-09-04 16:07 BST	2.28	-5.04	0.5	25.73	-0.048	0.211
R3	2020-01-11 17:06 GMT	2.22	-5.48	0.458	25.27	0.033	0.352
S10	N97205_pel	2.21	-5.34	0.495	25.42		
R1	2019-08-25 06:01 BST	2.27	-5.31	0.531	25.45	0.109	0.314

R2	2020-01-11 19:22 GMT	2.25	-5.43	0.473	25.33	0.224	0.363
R3	2020-08-16 01:33 BST	2.12	-5.28	0.482	25.47	0.561	0.256
S11	W957510_M	3.32	-7.25	0.476	23.44		
R1	2019-08-25 17:15 BST	3.31	-7.28	0.497	23.41	0.023	0.283
R2	2019-09-05 15:54 BST	3.32	-7.18	0.483	23.52	-0.039	0.191
R3	2020-01-12 00:06 GMT	3.32	-7.29	0.449	23.4	-0.744	0.324
S12	W957510_SK	3.24	-6.43	0.484	24.29		
R1	2019-08-25 15:10 BST	3.29	-6.36	0.496	24.36	0.106	0.273
R2	2019-09-05 13:39 BST	3.19	-6.47	0.499	24.26	0.092	0.218
R3	2020-01-12 02:20 GMT	3.24	-6.47	0.455	24.25	-0.666	0.335
S13	X90571_M	2.86	-7.01	0.466	23.69		
R1	2019-08-03 13:41 BST	2.89	-6.96	0.44	23.74	-0.046	0.228
R2	2019-08-14 20:28 BST	2.81	-7.05	0.469	23.66	-0.057	0.216
R3	2019-08-17 06:35 BST	2.87	-7.03	0.488	23.68	0.054	0.22
S14	X90704_BM	3.41	-7.83	0.451	22.84		
R1	2019-08-26 04:07 BST	3.43	-7.75	0.468	22.93	0.014	0.257
R2	2019-09-24 10:13 BST	3.34	-8.07	0.449	22.6	0.07	0.276
R3	2020-01-13 17:29 GMT	3.47	-7.68	0.435	23.01	-0.879	0.327
S15	X90704_Gm	3.29	-7.79	0.457	22.89		
R1	2019-08-25 21:37 BST	3.36	-7.8	0.462	22.88	-0.034	0.268
R2	2019-09-24 03:14 BST	3.23	-7.74	0.444	22.94	-0.11	0.26
R3	2020-07-31 13:49 BST	3.28	-7.82	0.464	22.86	-0.198	0.131
S16	X90704_Sk	3.41	-9	0.447	21.64		
R1	2019-08-25 23:47 BST	3.54	-8.91	0.475	21.74	-0.008	0.285
R2	2019-09-24 05:31 BST	3.38	-9.06	0.46	21.58	-0.086	0.317
R3	2020-08-16 07:07 BST	3.32	-9.05	0.407	21.59	0.033	0.242
S17	Y90101_BM	3.29	-7.21	0.448	23.49		
R1	2019-08-02 14:01 BST	3.35	-7.16	0.417	23.54	-0.108	0.223
R2	2019-08-08 17:04 BST	3.29	-7.32	0.445	23.37	-0.395	0.223
R3	2019-08-14 16:07 BST	3.22	-7.1	0.466	23.6	-0.058	0.216
R4	2019-08-17 02:19 BST	3.31	-7.24	0.465	23.45	0.151	0.167
S18	Y90101_GM	2.88	-6.98	0.457	23.72		
R1	2019-08-02 16:09 BST	2.81	-7.06	0.451	23.65	-0.125	0.234

R2	2019-08-08 21:25 BST	2.88	-7.04	0.456	23.66	-0.133	0.199
R3	2019-08-14 22:37 BST	2.92	-6.94	0.456	23.77	0.029	0.205
R4	2019-08-17 08:48 BST	2.93	-6.89	0.465	23.82	0.029	0.223
S21	Z94708_Bm	3.32	-6.74	0.463	23.97		
R1	2019-09-24 17:06 BST	3.29	-6.71	0.47	24	0.033	0.277
R2	2020-07-31 09:01 BST	3.3	-6.83	0.455	23.88	-0.176	0.134
R3	2020-08-16 09:35 BST	3.36	-6.69	0.464	24.02	-0.04	0.21
S22	Z94708_Sk	3.23	-8.37	0.4	22.29		
R1	2019-08-27 14:07 BST	3.25	-8.52	0.408	22.14	-0.485	0.304
R2	2020-08-06 16:23 BST	3.16	-8.31	0.406	22.35	-0.34	0.133
R3	2020-08-16 15:21 BST	3.27	-8.27	0.386	22.39	0.218	0.257
S23	Z94708_inn	3.05	-6.94	0.495	23.77		
R1	2019-08-26 06:16 BST	3.23	-6.74	0.496	23.97	0.058	0.276
R2	2019-09-24 12:29 BST	3.14	-6.83	0.473	23.88	-0.019	0.269
R3	2020-01-22 00:37 GMT	2.79	-7.25	0.517	23.45	-1.837	0.186

Chapter 5

	ID	d13C VPDB	d18O VPDB	D47 CDES	d18O VSMOW	D48 Offset	49 Param
S2	Z9484_M	3.58	-6.45	0.477	24.27		
R1	2021-11-01 10:29 GMT	3.62	-6.27	0.497	24.46	-0.328	0.067
R2	2021-11-07 03:15 GMT	3.62	-6.34	0.491	24.39	0.55	0.103
R3	2021-11-14 08:52 GMT	3.52	-6.72	0.452	23.99	0.071	0.234
R4	2021-11-17 20:28 GMT	3.54	-6.48	0.466	24.24	-0.028	0.194
S4	Z9484_Rud	3.43	-7.11	0.452	23.59		
R1	2021-11-01 08:06 GMT	3.44	-7	0.445	23.71	-0.711	0.058
R2	2021-11-07 08:20 GMT	3.47	-7.08	0.449	23.62	0.68	0.117
R3	2021-11-17 22:56 GMT	3.39	-7.24	0.461	23.45	0.151	0.183
S6	Z9652	4.77	-6.58	0.38	24.14		
R1	2021-11-01 03:16 GMT	4.78	-6.52	0.388	24.2	-0.455	0.072
R2	2021-11-07 00:43 GMT	4.77	-6.59	0.383	24.13	0.447	0.128
R3	2021-11-14 16:13 GMT	4.77	-6.55	0.4	24.16	0.365	0.162
R4	2021-11-18 03:54 GMT	4.78	-6.61	0.365	24.11	0.213	0.17
R5	2021-11-27 19:05 GMT	4.75	-6.64	0.364	24.08	3.497	0.193
S8	Z9653	4.85	-6.33	0.368	24.39		
R1	2021-11-01 15:19 GMT	4.85	-6.31	0.365	24.41	0.032	0.093
R2	2021-11-06 19:37 GMT	4.83	-6.43	0.379	24.29	0.476	0.118
R3	2021-11-18 06:27 GMT	4.86	-6.25	0.361	24.48	0.434	0.177
S10	Z9684-0	2.92	-4.86	0.504	25.91		
R1	2018-06-29 23:01 BST	3.03	-4.7	0.512	26.07	97.884	0.276
R2	2019-03-19 02:40 GMT	2.89	-4.87	0.494	25.9	-0.018	0.166

R3	2019-03-22 23:50 GMT	2.88	-4.97	0.493	25.8	-0.116	0.196
R4	2019-08-18 02:13 BST	2.9	-4.91	0.518	25.86	0.126	0.215
S2	MPA11_calc	2.41	-6.13	0.382	24.6		
R1	2021-05-09 03:44 BST	2.44	-6.31	0.358	24.41	-0.131	0.238
R2	2021-05-18 13:47 BST	2.41	-5.92	0.36	24.82	0.448	0.211
R3	2021-05-22 06:53 BST	2.34	-6.14	0.413	24.59	0.026	0.251
R4	2021-05-28 12:39 BST	2.43	-6.07	0.401	24.66	0.34	0.285
R5	2021-10-01 18:53 BST	2.43	-6.22	0.378	24.5	-0.085	0.342
S4	MPA24_dolo	3.49	-6.24	0.356	24.48		
R1	2021-05-09 10:59 BST	3.49	-6.35	0.392	24.37	0.158	0.273
R2	2021-05-16 20:08 BST	3.47	-6.25	0.371	24.48	0.15	0.198
R3	2021-05-21 23:07 BST	3.48	-6.17	0.335	24.56	-0.134	0.263
R4	2021-12-03 09:10 GMT	3.51	-6.21	0.324	24.52	1.099	0.252
S6	MPA34_dolo	6.38	-1.96	0.409	28.9		
R1	2021-05-09 06:09 BST	6.4	-1.97	0.42	28.89	0.127	0.303
R2	2021-05-18 19:10 BST	6.24	-2.11	0.381	28.75	0.439	0.251
R3	2021-05-22 04:22 BST	6.51	-1.7	0.401	29.17	0.445	0.243
R4	2021-09-22 18:57 BST	6.36	-2.05	0.434	28.81	-1.141	0.464
S7	MPA35						
R1	2013-10-26 18:11 BST	6.27	-0.18	0.405	30.74	0.228	0.153
R2	2013-11-05 20:13 GMT	6.29	-0.17	0.399	30.74	-0.21	-0.063
S9	WBH_25_dolo	5.68	-6.46	0.346	24.26		
R1	2021-05-09 13:24 BST	5.72	-6.35	0.337	24.37	-0.015	0.261
R2	2021-05-16 04:40 BST	5.61	-6.48	0.341	24.24	0.018	0.194
R3	2021-05-21 20:31 BST	5.7	-6.56	0.36	24.16	-0.003	0.254
S11	WSNE2_89_WC_dolo	4.31	-4.51	0.298	26.27		
R1	2021-05-09 20:40 BST	4.33	-4.46	0.276	26.32	-0.022	0.272
R2	2021-05-15 23:24 BST	4.28	-4.53	0.309	26.25	-0.11	0.174
R3	2021-05-21 15:14 BST	4.32	-4.53	0.308	26.25	-0.167	0.22
S13	WSNE2_89_matrix_dolo	3.71	-4.59	0.337	26.19		
R1	2021-05-09 18:12 BST	3.71	-4.63	0.332	26.15	-0.061	0.235
R2	2021-05-21 12:36 BST	3.66	-4.65	0.302	26.13	-0.234	0.226
R3	2021-09-16 06:04 BST	3.77	-4.38	0.368	26.4	-0.357	0.317
R4	2021-09-22 16:35 BST	3.7	-4.69	0.346	26.08	-1.392	0.462
S15	WSNE2_calcite	2	-6.4	0.384	24.33		
R1	2021-05-21 07:18 BST	2.17	-6.14	0.373	24.59	-0.203	0.17
R2	2021-05-28 20:56 BST	1.99	-6.09	0.36	24.65	0.165	0.221
R3	2021-09-16 03:33 BST	1.95	-6.67	0.378	24.04	-0.3	0.304
R4	2021-09-22 11:34 BST	1.88	-6.68	0.423	24.03	-1.768	0.287
S17	xMPA11B_calc	3.43	-7.33	0.433	23.36		
R1	2021-10-02 16:52 BST	3.81	-6.6	0.373	24.11	0.054	0.309
R2	2021-10-07 06:21 BST	3.57	-7.15	0.481	23.55	0.363	0.4
R3	2021-10-10 16:49 BST	3.62	-7.23	0.399	23.47	-0.174	0.371
R4	2021-10-18 10:02 BST	2.45	-8.98	0.513	21.67	1.016	0.674
R5	2022-05-04 12:15 BST	3.68	-6.69	0.4	24.02	-0.93	-0.342
S19	xMPA12A-G_dolo	3.46	-7.85	0.373	22.82		
R1	2021-10-10 09:37 BST	3.3	-8.17	0.324	22.5	0.575	0.243
R2	2021-11-27 09:00 GMT	3.53	-7.68	0.315	23	-0.643	0.132
R3	2021-12-02 05:46 GMT	3.57	-7.74	0.383	22.95	0.01	0.165
R4	2022-05-04 09:48 BST	3.43	-7.83	0.47	22.85	-3.326	-0.703

S21	xMPA12A_calc	3.48	-12	0.332	18.55		
R1	2021-10-10 14:26 BST	3.54	-11.85	0.342	18.71	-0.159	0.271
R2	2021-10-18 13:05 BST	3.41	-12.16	0.323	18.39	-0.217	0.335
S23	xMPA3_calc	-6.24	-4.26	0.389	26.53		
R1	2021-10-02 14:23 BST	-5.96	-3.55	0.356	27.26	0.045	0.305
R2	2021-10-07 01:34 BST	-6.12	-4.16	0.422	26.63	6.944	0.372
R3	2021-10-10 07:11 BST	-6.09	-4.06	0.374	26.73	0.016	0.353
R4	2021-10-18 20:27 BST	-6.78	-5.28	0.405	25.48	-0.01	0.48
S2	WN526_calc	-3.97	-2.9	0.479	27.93		
R1	2021-09-18 15:01 BST	-4.01	-2.83	0.469	28	-1.038	0.383
R2	2021-09-22 09:13 BST	-3.95	-2.85	0.486	27.98	-1.706	0.329
R3	2021-09-25 16:09 BST	-3.94	-3.03	0.482	27.79	-1.968	0.329
S4	WN627_calc	2.01	-3.03	0.382	27.8		
R1	2021-05-21 04:35 BST	2.08	-2.91	0.36	27.92	-0.181	0.176
R2	2021-05-28 04:37 BST	2.05	-3.09	0.383	27.73	-0.007	0.267
R3	2021-12-03 03:21 GMT	1.91	-3.08	0.404	27.75	0.034	0.187
S6	WS33_Brown_inf_calc	-1.17	-7.07	0.491	23.64		
R1	2021-01-28 08:20 GMT	-1.17	-7.22	0.529	23.48	0.327	0.063
R2	2021-04-03 15:56 BST	-1.2	-7.13	0.475	23.57	0.133	0.21
R3	2021-04-30 17:34 BST	-1.14	-6.99	0.478	23.72	0.027	0.169
R4	2021-05-16 12:22 BST	-1.16	-6.93	0.483	23.78	0.287	0.073
S8	WS33_Matrix_calc	-0.14	-6.29	0.383	24.43		
R1	2021-01-28 01:07 GMT	-0.14	-6.32	0.385	24.41	0.001	0.11
R2	2021-04-04 17:35 BST	-0.21	-6.4	0.36	24.33	0.759	0.269
R3	2021-04-24 18:27 BST	-0.17	-6.42	0.412	24.3	-0.03	0.201
R4	2021-04-30 10:28 BST	-0.12	-6.16	0.377	24.57	-0.102	0.174
R5	2021-05-16 14:51 BST	-0.08	-6.17	0.383	24.56	-0.003	0.122
S10	WS33_Orangeinfil_calc	-5.19	-5.02	0.594	25.75		
R1	2021-01-28 03:28 GMT	-5.2	-5.18	0.63	25.58	0.228	0.084
R2	2021-04-04 22:20 BST	-5.18	-4.98	0.597	25.79	0.135	0.187
R3	2021-04-30 15:12 BST	-5.17	-4.96	0.542	25.81	-0.055	0.189
R4	2021-05-16 07:21 BST	-5.18	-4.91	0.608	25.86	0.214	0.115
R5	2021-05-28 10:09 BST	-5.22	-5.06	0.59	25.7	0.231	0.224
S12	xWN625_Grey_calc	2.47	-2.86	0.341	27.98		
R1	2021-10-02 21:46 BST	2.56	-2.89	0.323	27.94	-0.055	0.313
R2	2021-11-16 09:08 GMT	2.49	-2.82	0.354	28.01	12.785	0.17
R3	2021-11-18 18:54 GMT	2.44	-2.83	0.331	28.01	0.076	0.131
R4	2021-11-26 13:43 GMT	2.41	-2.89	0.354	27.94	12.936	0.126
S14	xWN625_Red_dolo	2.3	-4	0.372	26.8		
R1	2021-10-02 19:25 BST	2.53	-3.67	0.346	27.14	0.064	0.338
R2	2021-10-07 08:49 BST	2.38	-3.86	0.412	26.94	0.348	0.388
R3	2021-10-11 00:20 BST	2.41	-3.85	0.372	26.95	-0.137	0.352
R4	2021-10-19 04:18 BST	1.8	-4.88	0.38	25.89	1	0.522
R5	2021-11-19 14:35 GMT	2.36	-3.73	0.352	27.07	0.03	0.223
S20	xxWN453_Wskel_calc	1.75	-4.24	0.343	26.55		
R1	2021-11-02 01:11 GMT	1.82	-4.12	0.354	26.67	-0.055	0.073
R2	2021-11-18 21:20 GMT	1.72	-4.37	0.356	26.41	0.119	0.157
R3	2021-11-27 01:48 GMT	1.73	-4.22	0.32	26.57	-0.089	0.198
S22	xxWN526_Grey_dolo	0.09	-3.17	0.349	27.65		
R1	2021-11-01 17:44 GMT	0.15	-3	0.354	27.83	-0.186	0.12

R2	2021-11-18 11:21 GMT	0.13	-3.04	0.346	27.78	0.117	0.184
R3	2021-11-27 04:15 GMT	0.11	-3.15	0.327	27.67	-0.099	0.215
R4	2021-12-02 10:29 GMT	-0.04	-3.5	0.367	27.31	0.161	0.197
S2	AK-13	6.04	-3.35	0.346	27.47		
R1	2022-05-09 13:10 BST	6.09	-3.4	0.346	27.41	-0.198	-0.057
R2	2022-05-13 19:30 BST	6.16	-3.16	0.347	27.66	0.041	-0.001
R3	2022-05-18 13:20 BST	5.87	-3.48	0.344	27.33	0.073	-0.107
S4	AK-23	6.08	-1.06	0.321	29.83		
R1	2022-05-10 13:01 BST	6.08	-1.05	0.31	29.83	-0.076	-0.032
R2	2022-05-14 19:22 BST	6.09	-1.05	0.331	29.84	-0.047	0.049
R3	2022-05-19 21:38 BST	6.06	-1.08	0.32	29.8	-0.057	-0.085
S6	AK-24	5.92	-1.05	0.348	29.84		
R1	2022-05-10 03:28 BST	5.83	-1.08	0.348	29.81	-0.087	-0.009
R2	2022-05-14 09:48 BST	5.96	-1.1	0.347	29.78	0.217	0.089
R3	2022-05-19 03:38 BST	5.98	-0.95	0.348	29.94	-0.055	-0.09
S8	AK-25	6.02	-0.02	0.313	30.9		
R1	2022-05-10 05:54 BST	6.04	0.06	0.289	30.98	0.064	-0.022
R2	2022-05-14 12:11 BST	6.04	-0.03	0.338	30.89	0.178	0.069
R3	2022-05-19 06:01 BST	5.99	-0.07	0.311	30.84	0.214	-0.096
S10	AK-27	3.21	0.38	0.359	31.31		
R1	2022-05-10 10:39 BST	3.24	0.52	0.338	31.46	0.066	-0.013
R2	2022-05-14 16:59 BST	3.24	0.39	0.362	31.32	-0.121	0.037
R3	2022-05-19 19:15 BST	3.14	0.22	0.379	31.15	4.428	-0.124
S12	AK-7	5.46	-2.82	0.354	28.01		
R1	2022-05-09 20:20 BST	5.45	-2.82	0.363	28.02	-0.175	-0.067
R2	2022-05-14 02:40 BST	5.48	-2.8	0.36	28.04	0.098	-0.006
R3	2022-05-18 20:27 BST	5.44	-2.86	0.339	27.97	0.021	-0.119
S14	MPA-35	6.38	-0.58	0.387	30.32		
R1	2022-05-10 01:07 BST	6.36	-0.61	0.369	30.29	-0.038	-0.025
R2	2022-05-14 07:26 BST	6.44	-0.48	0.388	30.42	0.175	0.055
R3	2022-05-19 01:14 BST	6.35	-0.65	0.404	30.25	-0.058	-0.104
S16	Mist-2	0.05	-8.14	0.399	22.53		
R1	2022-05-09 10:46 BST	0.05	-8.19	0.383	22.48	-0.127	-0.091
R2	2022-05-13 17:06 BST	0.06	-8.14	0.39	22.53	-0.069	-0.018
R3	2022-05-18 10:57 BST	0.05	-8.09	0.423	22.58	-0.347	-0.186
S18	Mist-31	2.03	-5.34	0.364	25.41		
R1	2022-05-10 22:37 BST	2.04	-5.25	0.357	25.51	-0.032	-0.056
R2	2022-05-15 04:55 BST	2.01	-5.41	0.371	25.34	0.032	0.028
R3	2022-05-20 07:14 BST	2.03	-5.37	0.365	25.38	0.213	-0.1
S20	Mist-5	0.52	-5.93	0.418	24.8		
R1	2022-05-10 15:26 BST	0.49	-6.01	0.419	24.72	-0.04	-0.049
R2	2022-05-14 21:44 BST	0.57	-5.75	0.411	25	-0.001	0.023
R3	2022-05-20 00:03 BST	0.48	-6.04	0.424	24.69	-0.02	-0.138
S22	Mist-6	1.27	-4.5	0.376	26.28		
R1	2022-05-09 17:57 BST	1.25	-4.51	0.372	26.27	-0.18	-0.068
R2	2022-05-14 00:16 BST	1.28	-4.53	0.355	26.25	0.143	-0.006
R3	2022-05-18 18:05 BST	1.27	-4.46	0.402	26.33	-0.173	-0.143
S24	Mist-8	1.69	-7.35	0.323	23.34		
R1	2022-05-11 01:01 BST	1.73	-7.13	0.302	23.57	-0.202	-0.068
R2	2022-05-15 07:18 BST	1.65	-7.51	0.332	23.17	-0.058	0.002

R3	2022-05-20 09:37 BST	1.69	-7.42	0.334	23.27	0.158	-0.099
S26	Mist-9	1.73	-3.38	0.393	27.43		
R1	2022-05-10 20:13 BST	1.65	-3.41	0.369	27.41	-0.071	-0.039
R2	2022-05-15 02:31 BST	1.78	-3.37	0.391	27.44	0.105	0.031
R3	2022-05-20 04:50 BST	1.77	-3.37	0.418	27.45	0.091	-0.127